Novel iridium complex as a new antimicrobial photodynamic therapy agent

Isuru Muthukudaarachchi

The University Of Sheffield.

A thesis submitted for the degree of Doctor of Philosophy
February 2022

The University of Sheffield
Department of Chemistry and School of Clinical Dentistry

Abstract

With the rise of antibiotic resistance many alternatives to antibiotic treatments have been suggested, among which is photodynamic therapy. Photodynamic therapy uses a compound (photosensitiser) which is not toxic without light, but becomes toxic when irradiated by light. Over the past few decades photodynamic therapy has seen a marked progress as an anticancer treatment while antimicrobial photodynamic therapy has remained relatively stagnant. *Porphyromonas gingivalis* and *Pseudomonas aeruginosa* are bacteria responsible for causing severe periodontal disease and skin infections, respectively. The diseases caused by these pathogenic bacteria are difficult to irradicate not only because they are difficult to access but also because they can develop resistance to antibiotics very quickly and/or can invade host cells to escape the action of both host immune responses and therapeutic agents. An effective antibacterial agent would need to be able to penetrate the host cell membrane, and target bacteria inside the host cells whilst remaining non-toxic to the host cells themselves.

Herein we introduce a novel aPDT conjugate - a new mononuclear iridium(III) complex which is cell-permeable, that is modified with an antibacterial agent metronidazole, that in itself cannot penetrate membrane of mammalian cells. The Ir(III) moiety acts as light-absorber and photosensitizer, whilst also carrying the antibiotic moiety across the cellular membrane. We demonstrate the effective antimicrobial properties of this conjugate against *P gingivalis* & *P.aeruginosa*. We show that: (i) The dosage required to achieve 99.9% killing of bacteria is extremely low; (ii) the conjugate works under visible light; (iii) the treatment does not damage host cells.

Acknowledgements

Firstly I would like to thank my supervisors Prof Julia Weinstein and Prof Simon Whawell. They have guided me throughout my PhD journey and enthusiastically supported me to test my ideas, which were not always conventional. In addition to being supportive of entrepreneurial side, they also showed great kindness and understanding through some difficult times. I will be eternally grateful to them for allowing me to be part of this project.

From the biology side I would also like to thank Mr Jason Heath and Ms Brenka McCabe for the training and guidance they provided me on microbiology and tissue culture throughout the project. Thank you to Ashley Gains, Cher Farrugia, Katherine Ansbro and Anita Liu for discussions on microbiology, tissue culture and answering my many questions. From Chemistry, thanks to Dr James Shipp and Dr Simon Parker for their help with the synthesis. Thank you to Dr Callum Jones for helping with the cell imaging. Special thanks to Dr Marta Martinez Alonso for productive discussions and sharing her expertise on iridium complexes.

A special thanks to Dr Christa Walther for helping with light microscopy and Dr Christopher Hill for taking electron microscopy images.

Thanks also go to Dr Joanna Shepherd for collaborating on the 3D skin model experiments. A special thanks to her PhD student, Rawan Alshalan. Her selfless support and guidance on 3D skin models before, during and after the experiment made this difficult and long experiment, which was done amidst restrictions, a smoother process.

Thank you, my large and loving family for inspiring and supporting me. Special thanks to my sister for always being there to listen to my problems. Finally, I would like to express my deepest gratitude to my parents for their love, endless support and inspiration.

List of abbreviations

a.u	arbitary units
A568	alexa fluor 568
AcOH	acetic acid
aPDT	antimicrobial photodynamic therapy
ATP	adenosine triphosphate
Bbz	2,2'-bisbenzimidazole
BHI	brain heart infusion
BSA	bovine serum albumin
CFU	colony forming units
Cy5	cyanine (650/670)
DAPI	4', 6-diamidino-2-phenylindole
DCC	N,N’-dicyclohexylcarbodiimide
DCU	dicyclohexyl urea
DED	decellularized dermis
DMEM	dulbecco’s Modified Eagle’s Medium
DMF	dimethylformamide
DMSO	dimethyl sulphoxide
DNA	deoxyribonucleic acid
eDNA	extracellular DNA
EDTA	ethylenediamine tetra-acetic acid
eqv	equivalents
FCS	fetal calf serum
FITC	fluorescein isothiocyanate
H357	cell line: Epithelial squamous cell carcinoma
HEK293	cell line: Human embryonic kidney cells
HEP-G2	cell line: Human hepatocellular carcinoma

IC	internal conversion
IC50	half maximal inhibitory concentration
IMS	industrial methylated spirit
ISC	inter system crossing
M	molarity ($moldm^{-3}$)
mdz	metronidazole
MeOH	methanol
MLCT	metal to ligand charge transfer
MS	mass spectrometry
MTT	3-(4,5-dimethylthiazol-2-yl)-2,5-diphenyltetrazolium bromide
NMR	nuclear magnetic resonance
OD	optical denisity
PBS	phosphate buffered saline
PDT	photodynamic therapy
ppm	parts per million
pqc	2-phenylquinoline-4-carboxylic acid
PS	photosensitiser
RNA	ribonucleic acid
ROS	reactive oxygen species
SFM	serum free medium
SIM	structured illumination microscopy
TEM	transmission electron microscope
TLRs	toll-like receptors
Uv-Vis	ultraviolet-visible
λem	emission wavelength
λex	excitation wavelength

Table of Contents

Chapter 1

Introduction to Photodynamic Therapy (PDT)

1.1 The Hidden Army

The discovery of penicillin in 1928 by Sir Alexander Fleming became a cornerstone of modern medicine. Since the beginning of its mass production in the early 1940s, antibiotics have taken many forms in aminoglycosides, tetracyclines, chloramphenicols, macrolides, glycopeptides, oxazolidinones, ansamycins, quinolones, and streptogramins.[1] This success lasted until the 1970s when the first reports of antibiotic resistance emerged. Ever since then the number of resistant bacteria have increased while the arsenal of effective antibiotics have dwindled.[2] In it was estimated that approximately 700,000 deaths occur every year from antimicrobial resistance, which is projected to rise to 10 million by 2050.[3] The annual death rate caused by antibiotic resistance has increased to 1.27 million as of 2019.[4] As this hidden army of bacteria threatens to return humanity back into a pre-antibiotic era, the need to find a successor to antibiotics has become urgent. Interestingly, a technique which came to light approximately 30 years before the discovery of penicillin has remerged as a viable antimicrobial treatment. This technique is the use of a photochemically generated singlet oxygen to attack pathogens or cancer cells, and has come to be known as Photodynamic Therapy (PDT).

1.2 Singlet Oxygen to PDT

Thermal or photochemical reactions involving oxygen can lead to the generation of singlet oxygen, the lowest excited state of O_2.[5,6] Thermal reactions will make use of various reaction

precursors (e.g. phosphite, ozonides or peroxides). Aromatic endoperoxides have become the most prevalent class of precursors for thermal generation of singlet oxygen. Among hundreds of aromatic endoperoxides, which has proven to release singlet oxygen, anthracene derivatives have taken a prominent place.[7] The major disadvantage presented by endoperoxides is their low yielding release of singlet oxygen due to its relatively higher activation barrier, which is ca. 38 kcal mol^{-1}(158.99 kJ mol^{-1}).[8,9] This results in the release of dioxygen in either its singlet or triplet state. Turro *et al* suggested that this release may be stepwise, involving the conversion of a biradical intermediate to a triplet biradical via intersystem crossing (ISC). However, singlet oxygen generation with the use retro [4 + 2] cycloadditions involving 1,4-endoperoxides is a single-step reaction, which results in only singlet oxygen and the parent anthracene (Scheme 1). Modifying 1,4-anthracene derivatives is a reliable source of thermally generated singlet oxygen, for use in organic reactions such oxy-functionlizations.

Singlet oxygen may be generated photochemically from peroxides. It can also be generated by the excitation of a photosensitiser (PS) followed by an energy transfer to triplet (ground-state) oxygen. These photosensitisers vary from various dyes to transition metal complexes (discussed below). Generation of singlet oxygen photochemically has many applications, including PDT.

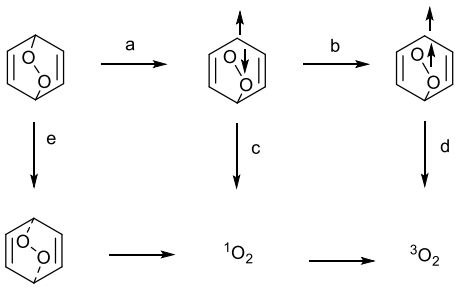

Scheme 1- Mechanism for the biradical generation of $^3O^2$ (path a → b → d) and the concerted mechanism for the formation of $^1O_2$ (from ref [9])

1.3 Photodynamic Therapy

PDT is a relatively non-invasive therapeutic method for the destruction of unwanted cells. The main advantage of PDT over traditional chemotherapy is its specificity. PDT makes use of a PS and a light of wavelength specific to the PS to generate singlet oxygen or reactive oxygen species (ROS), which causes irreparable oxidative damage to cells. The PS may be administered topically or intravenously. The drug is then allowed to incubate. Depending on the PS, this may vary from 5 min to 24 h. The desired area is then illuminated with light of a specific wavelength. The ideal activation wavelength of the PS should be 600 – 800 nm. This range ensures generation of singlet oxygen while avoiding interactions with native chromophores of the body (e.g. melanin).

Initially the PS is in its singlet ground state. Upon absorbing a photon of appropriate energy, the PS is excited into a higher energy singlet state (Figure 1). The excited singlet state of the commonly used organic PS is very short-lived (nanoseconds timescale). The PS will dissipate its excess energy by either emitting light (florescence) or a process known as internal conversion (heat production). Alternately the PS may undergo intersystem crossing (ISC) to a triplet state.

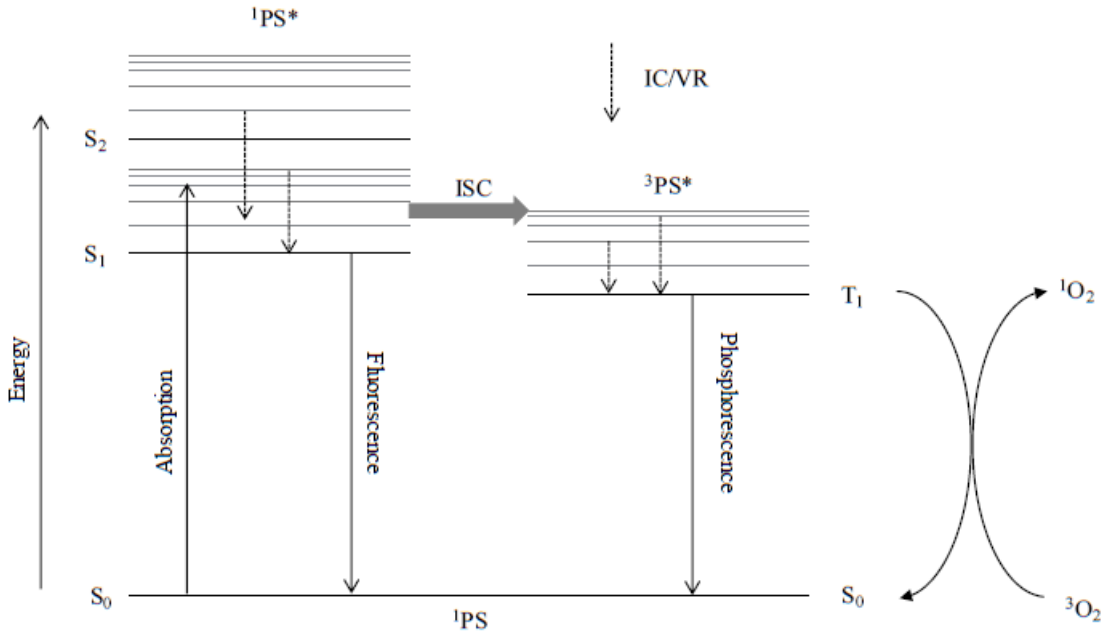

Figure 1- Simplified Jablonski diagram showing typical energy levels and transitions relevant to the formation of the triplet state and photosensitization of molecular oxygen.

This triplet sate is generally longer-lived than the singlet excited state. The lifetime of the triplet state is long enough for it to transfer energy to triplet oxygen, converting it to an excited singlet oxygen in the process. This is an example of a Type II photochemical process[10] (i.e. direct transfer of energy from PS to triplet O_2). This direct energy transfer promotes an electron of $^3O_2$ to a higher energy level while inverting its spin. The lowest two singlet states of dioxygen, denoted as $^1\Delta_g$ and $^1\Sigma_g$, are distinguishable by the π-antibonding and the ca. 63 kJ mol^{-1} energy gap. The higher energy $^1\Sigma_g$ state is very short-lived as the transition to $^1\Delta_g$ is a spin-allowed transition. The lifetime of $^1\Delta_g$ state is dependent on two processes, physical quenching and chemical quenching. In physical quenching, $^1O_2$ transfers its excess energy onto another species. No products are formed and the $^1O_2$ molecule decays to $^3O_2$. Chemical quenching sees chemical reactions between $^1O_2$ and other molecules resulting in formation of isolatable products.[11] Singlet oxygen is a formidable electrophile capable of reacting with nucleophiles such as amines, unsaturated

carbon chains and anions resulting in products such as peroxides. These peroxides, upon decomposition, are capable of initiating various reactions in biological systems.[12]

The lifetime of singlet oxygen in biological systems is dependent on both physical and chemical quenching; singlet-state lifetimes, τ_S, in water is ca. 4 μs [13]. This lifetime is even shorter in cells due to multiple chemical quenching (*e.g.* enzymatic reactions and reactions with biomolecules such as DNA). The lifetime of singlet oxygen plays a role in the selection of organelles damaged during PDT.

A Type I photochemical reaction may also occur. Here, the PS maybe involved in a reduction reaction, obtaining electrons from biological electron donors such a tryptophan, tyrosine and NADPH, resulting in two radical pairs (i.e. $PS^{-\cdot}$ and biomolecule$^{+\cdot}$) In the presence of oxygen the $PS^{-\cdot}$ donates an electron to molecular oxygen resulting in a superoxide anion radical, $O_2^{-\cdot}$ and the ground-state PS. $O_2^{-\cdot}$ is capable of acting as a reductant or an oxidant.

In PDT, Type II believed to be the dominant process and occurs with more ease. This may be due to the presence of enzymes that protect against superoxides and the lack of enzyme that can neutralize $^1O_2$. That said, some studies have shown that high efficiency of PDT is achieved through the combined effects from type I and type II reactions.[14]

1.4 Properties of Ideal PDT agents

There is an arsenal of potential PDT agents. Listed below are some properties these candidates should possess in order to be an effective PDT agent:

- **Absorbance band** – The ideal absorbance wavelength for a PDT agent is in the near-infrared (NIR) region of the electromagnetic spectrum, 650 – 800 nm. This allows for maximum penetration of light without interacting with endogenous chromophores and water (Figure 2) whilst maintaining high enough energy for optimal activation of the PS.
- **Single and pure compound** – Allows for Good Manufacturing Practice (GMP), good quality control and lower manufacturing costs.
- **Triplet quantum yield** – High triplet quantum yield to ensure maximum production of ROS.
- **No dark toxicity and rapid evacuation from healthy cells** – Although initially it was thought that ideal drug-light interval was as long as up to 4 days to give time for accumulation in tumors and clear-out from healthy cells and excreted from the body, it is now thought the ideal time is much shorter (minutes/hours) and should be excreted out much quicker as prolonged exposure can cause vascular damage.[15]

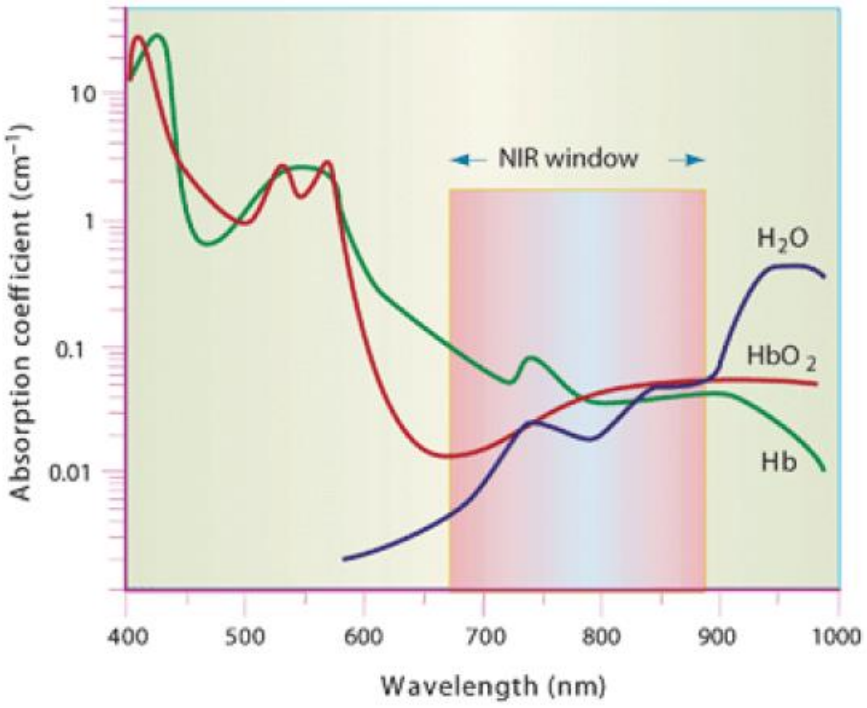

Figure 2- Absorption spectra of typical absorbances in human tissues (from ref [16]).

1.5 Brief overview of PDT agents

Tetrapyrrole Structures

Making up the largest group of anti-cancer PDT agents, tetrapyrrole structures are dubbed as the 'pigment of life'. This is due to their backbone appearing in many biological molecules such as haem and chlorophyll. Due to the large extended resonance of the C=C double bonds, the absorption of the so-called Q-band is significantly red-shifted. The Q-band refers to the weak electronic transitions ($S_0 \rightarrow S_1$) in an absorption spectrum. The peaks that correspond to strong electronic transitions ($S_0 \rightarrow S_2$) are called the Soret bands.

- ***Porphyrins***

The work on porphyrin based PDT agents, spearheaded by Dr Thomas Dougherty, sparked the modern era of the photodynamic therapy. Dougherty *et al.* introduced haematoporphyrin (HpD) a water-soluble mixture of porphyrins.[17–19] A more refined version was later developed and came to be known as Photofrin. Although widely used, Photofrin has marked disadvantages, including skin photosensitivity potentially lasting up to several months. It is inefficient for use in bulky tumors due to its small absorbance peak at 630 nm with a molar extinction coefficient of 1170 M^{-1} cm^{-1}.[20]

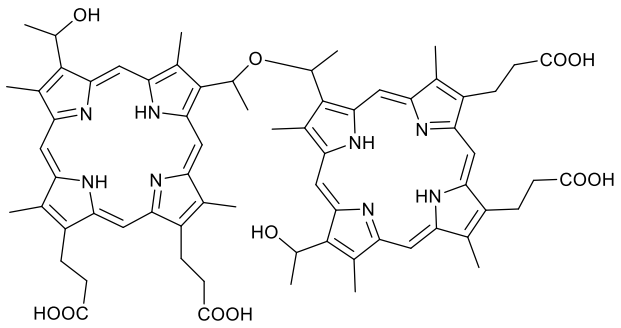

Photofrin

- ***Phthalocyanines***

Phthalocyanines have an absorbance of 630 nm. Several cationic phthalocyanines have been studied as antimicrobial PDT agents.[21,22] In contrast to porphyrins, phthalocyanines have strong absorbances at 630 nm. The molar extinction coefficients range between approximately 1.56 x 10^5 M^{-1} cm^{-1} – 2.75 M^{-1} cm^{-1}. This is dependent on the substituents. For example, the work of Ouedraogo *et al* using axially substituted iron phthalocyanines showed no charge transfer in the Q band region. Alternatively, the work of Zang *et al* using amino substituted zinc phthalocyanines showed wide Q bands owing to charge transfer from ligands to π system of the phthalocyanine.[23]

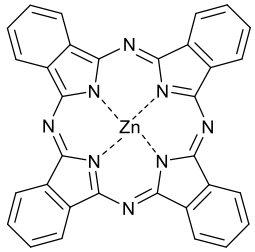

Liposomal ZnPC (Phthalocyanine)

- ***Chlorins***

Derived from chlorophyll, various chlorins such as Temoporfin and Verteporfin are in clinical use.

[24]. Chlorins are activated in the 650 – 700 nm range.

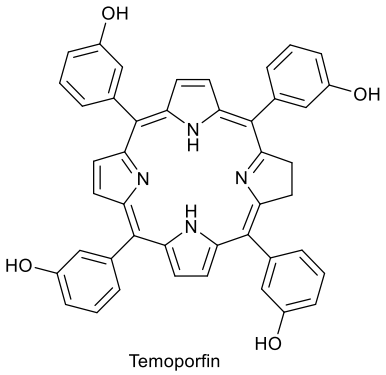

Temoporfin

BODIPY dyes

Relatively new class of PDT agents, boron-dipyrromethene (BODIPY) dyes consists of fluorophores and a BF_2 bridging unit. BODIPY dyes are often used in conjunction with transition metal complexes to achieve higher excitation wavelengths due to the ability of the π-conjugated linkers to absorb visible light.[25]

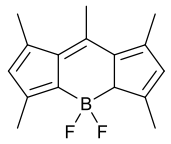

Difluoro{2-[1-(3,5-dimethyl-2H-pyrrol-2-ylidene-N)ethyl]-3,5-dimethyl-1H-pyrrolato-N}boron

Transition Metals – Discussed in detail under Section 3.

1.6 PDT agents in the clinic and in clinical trials

Several of the PDT classes mentioned above have been investigated in clinical trials for various diseases. Periodontal disease is by far the biggest application of aPDT according to literature and clinical trial data. Other antimicrobial applications of PDT include antifungal applications, acne treatments and treatments of chronic skin infections. Below is a summary of selected clinical trials of these for periodontal disease.

1.6.1 Periodontal disease

Citation	Treatment	Clinical outcome
Mueller *et al*. [26]	Each periodontal pocket was treated with methylene blue (0.05 mg/mL) and incubated for 1 minute. The pockets were then treated with 670	There was no significant reduction between groups in pocket depth (PD) and bleeding upon probing (BOP)

	nm light (289 mW, 60 s/pocket).0-7 sessions	
Segarra-Vidal *et al*.[27]	Procedure was conducted according to manufacturer's (Periowave® system) instructions. The photosensitser used was methylene blue (0.05 mg/mL) and the diode was a 670 nm diode probe.	There was no significant reduction in pocket depth and bleeding upon probing. The study also showed the patient group with periodontal disease showed increased bacterial counts of *P.gingivalis*, *T. forsythia*, *T.denticola*.
Skurska *et al*.[28]	One group was treated with methylene blue (10 mg/mL) + light (660 nm). The control group was treated with antibiotics (metronidazole + amoxicillin).	The group treated with antibiotics showed significant improvements in their condition compared to the group treated with PDT who showed no significant improvements.
Alwaeli *et al*.[29]	Methylene blue (10 mg/mL) was incubated for 1-3 minutes and irradiated with 660 nm (60 mW 10 s)	There was a significant reduction in PD and BOP in the PDT + Scaling and root planing (SRP) group than group with only SRP.
Hill *et al*.[30]	Indocyanine green (0.1 mg/mL) was incubated for 1 minute and irradiated with 808 nm (100 mW) diode	There was no significant reduction between groups in pocket depth (PD) and bleeding upon probing (BOP) or pathogen reduction.

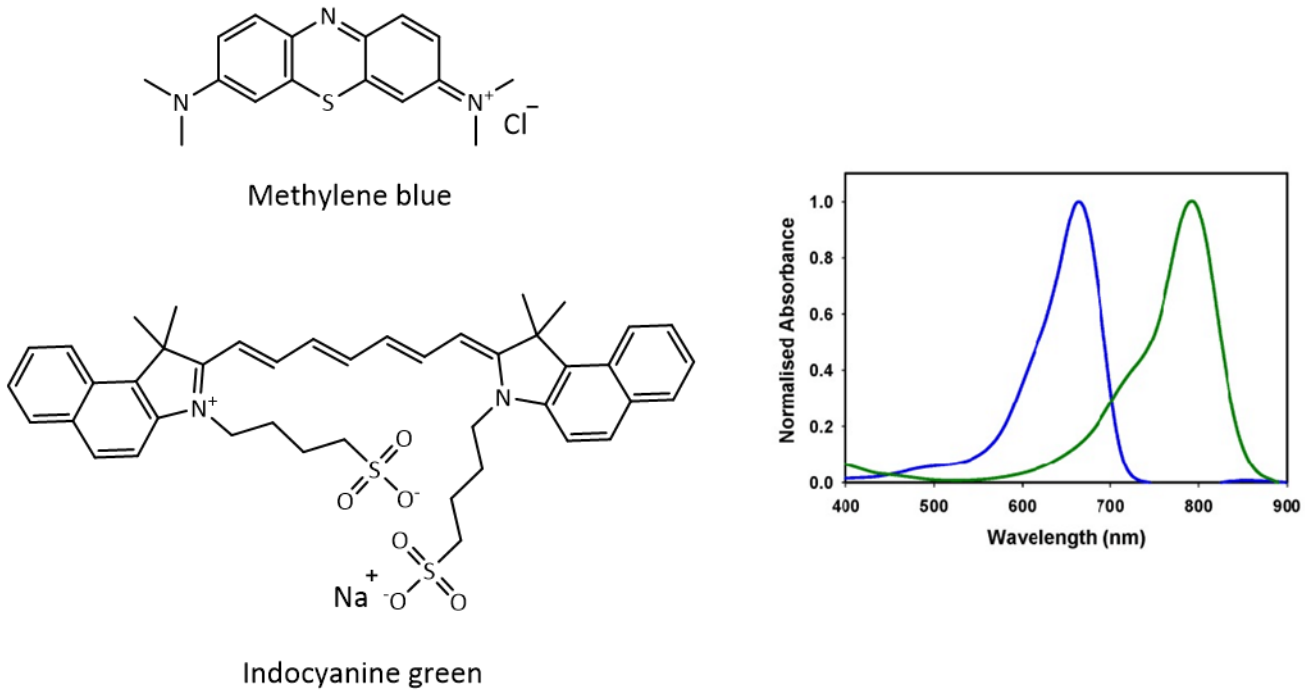

Figure 3- The chemical structures of methylene blue and indocyanine green. The absorption spectra are shown on the right (blue -methylene blue, green - indocyanine green)

1.7 Antimicrobial Photodynamic Therapy (aPDT) vs Antibitoics

Although PDT has gained more popularity as anti-cancer treatments, PDT first came to light as a result of the work of Oscar Raab, a medical student working on the effect of acridine dye on *Paramecia*.[31] However, the interest in aPDT peaked in the early 1990s when reports of PDT agents being able to selectively target microbes emerged. It was suggested that the best way to target microbes while minimizing interactions with the host cell was the use of PDT agents with a large positive charge, making them electrostatically attractive to bacterial cell walls possessing a prominent negative charge.[32] Moreover, aPDT is an appealing replacement for antibiotic treatments as aPDT agents have been shown to be effective against bacteria, even those

extremely resistant to antibiotics.[33] The inability of bacteria to become resistant to aPDT agents, even after several partial killing-growth cycles is especially appealing and reassuring. Whereas, effective antibiotic action may take days or weeks, aPDT is rapid, taking only minutes to show significant effect.[34]

Despite these great advantages, the power of aPDT is greatly underestimated and seemed to have taken a backseat in the medical and pharmaceutical communities. In the review mentioned above, many strategies to counteract antibiotic resistance has been suggested. Some of these suggested strategies include antibodies, probiotics, immune stimulation, vaccines etc. It, however, failed to mention aPDT, despite having over 2000 citations in PubMed.[3]

Even so, aPDT has seen an increase in popularity in certain fields, one of which is dentistry where PDT is used to tackle dental infections caused by oral pathogens such as *Porphyromonas gingivalis*.

1.8 *Porphyromonas gingivalis*

Porphyromonas gingivalis is a Gram-negative bacterium that grows under anaerobic conditions. Out of about 700 bacterial species to occupy the oral cavities, *P.gingivalis* is one of the few and the most prominent cause of severe forms of periodontal diseases. In contrast to Gram-positive bacteria, Gram-negative bacteria have a thicker peptidoglycan wall and an additional lipid membrane. This makes infections caused by Gram-negative bacteria difficult to treat.

P.gingivalis is able to survive deep within periodontal pockets by fermenting amino acids such as cysteine. The presence of heme and vitamin K is also crucial for it survival.[35] The aggregation of heme to its cell wall gives *P.gingivalis* its characteristic black colour in blood agar cultures. [36] Due

to its ability to invade host cells using lipopolysaccharide (LPS) in their cell wall, *P.gingivalis* is able to escape detection from the immune system and avoid attacks from antibiotics. This strategy is crucial for its survival and is the major obstacle in treatment of periodontal diseases.[37] It is shown that the interaction of β1 integrin with the major fimbriae (discussed below) of *P.gingivalis* causes the actin cytoskeleton of the host cells to rearrange leading to its invasion. Interestingly *P.gingivalis* is also able to invade macrophages, hinting this may be tactic to evade the immune system.[38] Upon successful invasion, *P.gingivalis* has been shown to secrete enzymes responsible for the hydrolysing of ATP, delaying the ATP dependent process of cell apoptosis. This allows the pathogen to live inside the host for an extended period of time.[39] It is then free to spread to neighbouring cells via actin cytoskeleton bridges, allowing for pathogenesis with minimal exposure to the immune surveillance and antibiotics.[40]

1.8.1 Virulence factors of P.gingivalis

Virulence factors are molecules employed by pathogens to facilitate host cell invasion and propagate diseases. *P. gingivalis* has several virulence factors in its arsenal. However, cysteine proteases, lipopolysaccharide, capsular polysaccharides and fimbriae are its most powerful weapons.

- **Cysteine proteases (gingipains)** - Accounting for over 85% of protein hydrolysis of *P.gingivalis*, gingipains are soluble proteases that are divided into two categories, arginine specific (Arg-X), responsible for the hydrolysis of extracellular matrix components, and lysine specific (Lys-X), which aids in cell adhesion in addition to its proteolytic capabilities.[41–43]

- **Lipopolysaccharide (LPS)** - LPS is a class of polysaccharides that covers all Gram-negative bacteria. Upon binding to host receptors such as Toll-like receptors (TLRs) and CD14, it is able to stimulate a cascade of signals within the cell. This allows the host cell to differentiate between commensal and harmful bacteria. One such signal caused by *P.gingivalis* LPS, as shown by Chiang *et al*., leads to inflammatory reactions and bone resorption.[44] As well as having a different structure to other Gram-negative bacteria, the LPS of *P.gingivalis* also shows variations from strain to strain. Examples include the structural differences in the O-antigen (a repetitive monomer in lipopolysaccharides), acylation patterns and the varying ability of lipid A to activate receptors: most Gram-negative bacteria show strong affinity towards TLR4 receptor whereas lipid A of *P.gingivalis* mainly activates the TLR2 receptor. It has also been shown that in the presence of high concentrations of hemin, *P.gingivalis* is able to modify its lipid A from penta-acylated lipid-A to tetra-acylated lipid A. This may play a role in *P.gingivalis*' ability to subvert immune signalling by changing the communication between LPS and TLR receptors according to the environment it is in.[45,46] A paper published in 2005 by Paramonov *et al* reported the presence of another category of LPS where lipid-A was linked to an anionic polysaccharide, named A-LPS. According to the study, A-LPS has structural associations with Arg-X gingipain and is able to induce weak cytokine responses in host monocytes, which not seen in bacteria with more mainstream LPS structures.[47]

- **Capsular polysaccharides (CPS) -** One of *P.gingivalis*' most formidable virulence factors is thought to be its capsule, otherwise known as K-antigen or CPS. The high increase in

invasion capabilities of encapsulated bacteria as opposed to non-encapsulated bacteria has been demonstrated in a murine lesion model.[48] CPS are divided into six categories depending on their ability to stimulate the responses from IgG antibodies.[49] CPS also provides another line of defence against the immune system by protecting the bacteria from phagocytosis. Moreover, they may assist in the adherence of the bacteria onto gingival epithelial cells.[50] Furthermore, study showing the increased cytokine stimulation by non-encapsulated mutants show the importance of CPS in softening the immune response and for the survival of *P.gingivalis* in the periodontal pocket.[51]

- **Fimbriae** - Fimbriae are thin appendages on the surface of *P.gingivalis*. They are of two types, type I and type II. Type I fimbriae are involved in the early establishment of the pathogen by providing aid in the formation of biofilms whereas type II fimbriae play a role in downplaying the immune response from T-cells. However, it should be noted *P.gingivalis* strains that lack type I fimbriae are still highly invasive and virulent.[52,53]

1.8.2 Treatments for periodontal disease

Many treatments are in use to treat periodontal diseases. One such method is the mechanical removal of plaque and flushing/rinsing with disinfectants. These, however, do not guarantee the complete cleansing of the periodontal pockets. In severe cases antibiotics such as metronidazole, amoxicillin or penicillin maybe administered. However, as mentioned above, antibiotic resistance is on the rise. Treatments against periodontal bacteria have also faced problems of antimicrobial resistance. For example, in studies published in 1983 and 1993 the percentages of bacteria

resistant to metronidazole, penicillin and amoxicillin were 0-2%, 2-3% and 0.5% respectively.[54] A study published in 2002 demonstrated the rise in percentage resistance within the span of ten weeks for doxycycline (6% to 35%), amoxicillin (0.5% to 25%) and metronidazole (50% to 80%).[55]

Various studies published in the last two decades with regards to antimicrobial PDT has resulted in its incorporation into clinical periodontology. Most commonly used aPDT agents in periodontology include toluidine blue and methylene blue, which have been shown to be effective against both Gram-positive and Gram-negative bacteria.[56] While early studies have shown various oral bacteria to be susceptible to methylene blue and toluidine blue, later studies showed that they are ineffective in completely destroying the pathogens, especially those in biofilms.[57,58] The increased resistance is possibly caused by the biofilm reducing the uptake of the dye and possible inactivation of methylene blue.[59,60] Methylene blue treatments may be administered using kits such as Periowave™ Treatment kit or Helbo™ Blue treatment kit. Here the periodontal pocket is treated with methylene blue and allowed to incubate for 60 s. The pocket is then exposed to red light for 60 s using a fibreoptic probe. While organic PDT molecules are widely used, they have many drawbacks that are preventing PDT from becoming a more mainstream form of antimicrobial and anticancer treatment. For example, Photofrin causes prolonged light sensitivity due to slow evacuation from cells. Also, as mentioned above, methylene blue and toluidine blue are ineffective at complete removal of infections – it is not clear if these agents even enter human cells, or only kill bacteria outside of human cells. The need for a more effective PDT agents have led to researchers looking beyond the horizon of traditional heterocyclic ring structures. Inspired by the monumental success of cisplatin and subsequent

transition metal complexes as anticancer agents, the recent decade has seen an increase in the use of transition metal complexes as PDT agents.

3.1 Transition metal complexes vs Organic molecules for PDT applications

Transition metal complexes are another new class of PDT agents. Many of the initial transition metal PDT agents were born as biological imaging probes.[61] Among the most studied transition metal complexes for PDT are Ru(II), Ir(III), Pt(II), and Re(I). As mentioned above, an ideal PDT agent should have strong absorbance in the NIR range with long-lived triplet states to ensure high quantum yields of $^1O_2$ and/or other ROS. The latter two are dependent on effective intersystem crossing (ISC). However, it is very difficult to determine the relationship between molecular structure and the rate/efficiency of the ISC, especially in the molecules lacking a heavy atom centre. The transition from S_1 to T_1 is non-radiative and adheres to the laws of conservation of energy and momentum (angular momentum). This is achieved via spin-orbit coupling (SOC). SOC is an interaction that couples electron spin and the orbital angular momentum allowing two spin states to couple (usually forbidden) whilst conserving total angular momentum.[62] Transition metals can be classified into what is known as heavy atoms. Heavy atom nuclei possess a strong positive charge. Electrons moving in its close proximity will be accelerated to relativistic velocity resulting in a strong coupling between spin and the orbital magnetic momentum. Thus, transition metals are able to induce strong ISC due to the enhanced SOC effects.

Most organic PDT chromophores consist of a system with extended π-conjugation. Upon excitation a π-π* transition is observed. Due to a large exchange integral, these compounds have an increased energy gap between S_1 and T_1 states. This results in weak ISC.

Although capable of efficient ISC, transition metal complexes have poor molar absorptivity in the visible light region. This has significantly held back applying transition metals as PDT agents. The weak molar absorption coefficients maybe due to the weak absorption of S_0-^{1}MLCT transition,

where the HOMO and the LUMO are localised on different parts of the molecule, and hence the orbital overlap is comparatively small. [63,64]

Based on these problems, two solutions are apparent. One is to append the metal with a visible light harvesting chromophore such a BODIPY dye. One drawback of this method is, even though the complexes show strong visible light absorption, the energy harvested by the ligand is not channelled to the metal centre. So even though excitation wavelength is improved, the quantum yield of the triplet state is not necessarily affected. The alternative is to bind the light-harvesting chromophore to the centre via an unsaturated C=C bond or to attaching the chromophore by direct metalation (C-metal bond).[65,66] It is much more difficult to make such modifications to small organic chromophores since the ISC mechanism vary from one another and chemical modifications will form compounds with unforeseen photophysical properties.

Transition metal complexes show efficient and predictable ISC with high yielding and long-lived triplet states. Moreover, they are relatively easily to modify to fine-tune photophysical and/or biological properties, making them an exciting class of new PDT agents. Cyclometalated metal complexes in particular are emerging as strong candidates in this category.

3.2 The photophysics of cyclometalated complexes

Being strong-field ligands, cyclometalating ligands enhance the formation MLCT states which is much desired in PDT (Figure 4). This is due the ability of cyclometalating ligands to split the metal *d*-orbitals of the metal efficiently, promoting MLCT over metal centred charge transfers. In 2002 Hay showed that the LUMO and LUMO+1 to be ligand-based π* orbitals. The presence of a rich

π system in cyclometalating ligands may also allow excitation of an electron into a π* orbital. [67–69] The high SOC of metal centre then enable ISC into a ligand based triplet π-π* state. In reality a mixed MLCT-^{3}[π-π] is seen.[70] It should be noted that, according to a paper published in 2005 by Park *et al*., inter ligand energy transfer (ILET) from ^{3}MLCT to an ancillary ligand may also be seen, allowing for fine-tuning of the emission wavelengths.[71]

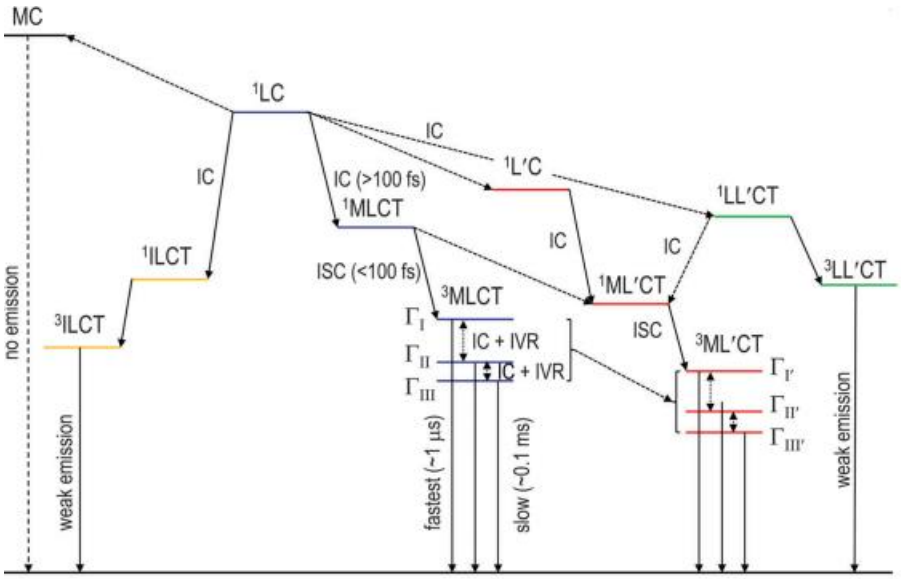

Figure 4- Photophysics of cyclometalated Ir(III) complexes (from ref [67])

Such example was demonstrated by Yersin *et al*., where the group demonstrated the drastically different photophysical properties of two Ir(III)-complexes bearing two identical cyclometalated ligands each, (2-(4',6'-difluorophenyl)pyridine), but different ancillary ligands. One was bearing a acetonylacetonato ligand (FIracac) while the second carried an N,O-bound picolinato ligand (FIrpic). The emission spectra and structures of these complexes are shown in Figure 5. Due to the nitrogen possessing a stronger ligand field effect than oxygen it is able to lower the energy of the three occupied d orbitals of the t_{2g} (i.e. HOMO) better than oxygen thereby increasing the

d-π* energy gap, causing as increase of energy in the MLCT transition and ultimately causing a blueshifted emission. [72,73]

To date the cyclometalated complexes that have been studied for PDT and singlet oxygen sensitization have been octahedral d^6 Ir(III) complexes or square planar d^8 Pt(II) complexes. The former will be the exclusive focus of this review.

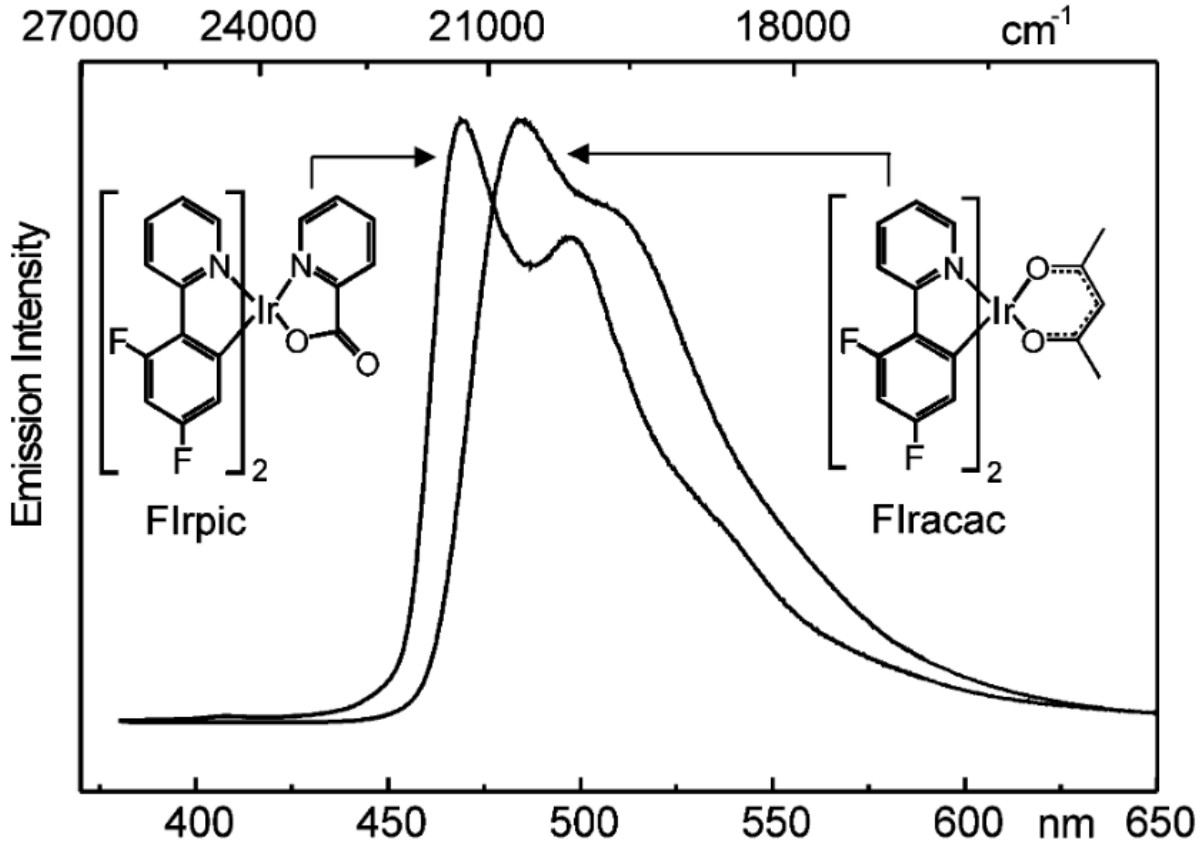

Figure 5- Emission of FIracac and FIrpic in CH_2Cl_2 (λexc 300 nm) at 300 K (from ref [33])

3.3 Cyclometalated Ir(III) complexes

3.3.1 Synthesis of Ir(III) complexes

Cyclometalated Ir(III) complexes are octahedral in structure. They are able to bear one, two or three cyclometalating ligands. Mono-cyclometalated Ir(III) complexes are rare and have not been investigated for singlet oxygen formation. On the other hand biscyclometalated Ir(III) complexes have been extensively studied for singlet oxygen production. They are of $Ir(C\hat{}N)_2L_2$ (C^N=cyclometalating ligand, L=ancillary ligand). The ancillary ligand may be two singly bound ligands or a single chelating ligand.

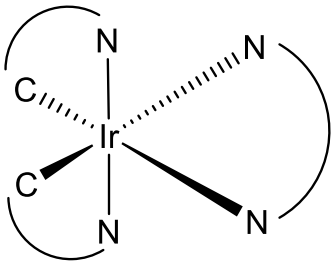

General structure of $Ir(C\hat{}N)_2L_2$

Their synthesis is relatively simple; $IrCl_3$ is refluxed with 2-2.5 equivalents of the cyclometalating ligand to yield a dimer bridged by two chlorides. This chloride bridge is then broken by the addition of the desired ancillary ligand. These biscyclometalated complexes can also be used as precursors for the production of tris-cyclometalated variants by simply displacing the ancillary ligand by refluxing with another cyclometalating ligand. It should be noted that, with the appropriate ligand, the reflux temperature may be used to control the formation of either the facial or meridional isomer.[74] Scheme 2 shows various sample pathways for the synthesis cyclometalated Ir(III) complexes.

Another interesting synthetic route was shown by Swager *et al*. in 2011. The paper showed preparation of a plethora of cyclometalated Ir(III) complexes with the use of a Cu(I) trazolide intermediate for the transmetalation step. The advantage is the one-pot reactions of ligand synthesis and the cyclometallation step.[75]

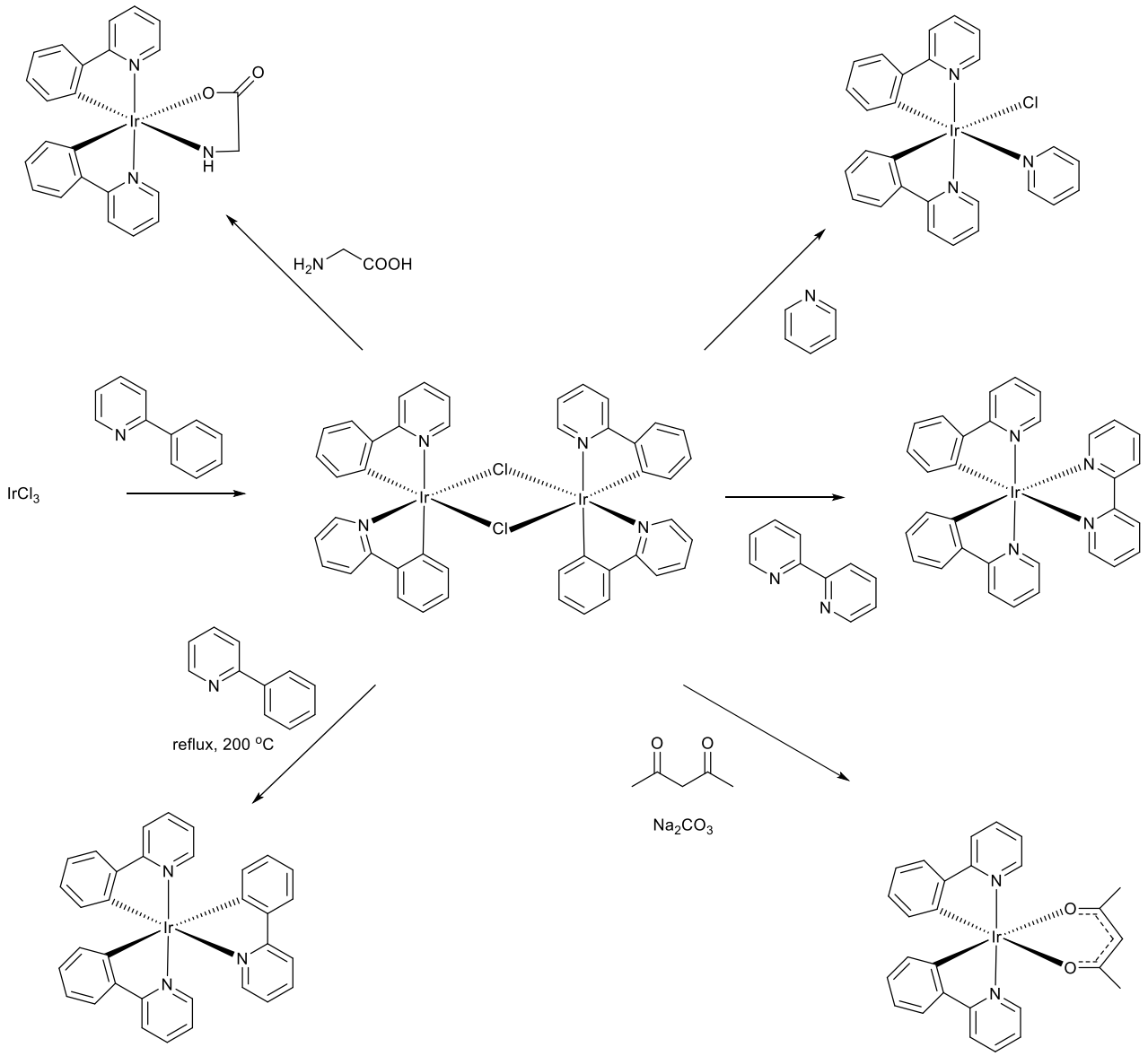

Scheme 2- Possible synthetic pathways for the synthesis of bis- and triscyclometalated Ir(III) complexes. All complexes are made at 140 °C for in 2-methoxyethanol for 24 hours unless otherwise stated

3.3.2 Cyclometalated Ir(III) complexes and singlet oxygen – the mechanism

The interest in cyclometalated Ir(III) as photophysical singlet oxygen generators spiked in 2002 following a paper by the groups of Thompson and Selke. A full paper was later published in 2007 which demonstrated the ability of ten cyclometalated Ir(III) complexes (Figure 6) to produce singlet oxygen in addition to the investigations on the mechanism of singlet oxygen generation by these complexes.[76,77] Singlet oxygen may quench the triplet excited MCLT-π-π* of cyclometalated Ir(III) via three routes: direct transfer of energy to form singlet oxygen (Eq 1), an electron transfer resulting in a superoxide anion or simple physical deactivation

$[Ir(C\hat{}N)_2L_2]^* + {}^3O_2 \rightarrow {}^1O_2 + [Ir(C\hat{}N)_2L_2]$ (Eq 1)

$[Ir(C\hat{}N)_2L_2]^* + {}^3O_2 \rightarrow {}^3O^{-\bullet}{}_2 + [Ir(C\hat{}N)_2L_2]^+$ (Eq 2)

$[Ir(C\hat{}N)_2L_2]^* + {}^3O_2 \rightarrow {}^3O_2 + [Ir(C\hat{}N)_2L_2]$ (Eq 3)

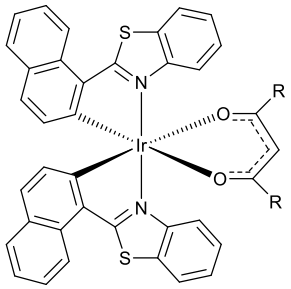

1: R = Me

2: R = t-Bu

ϕ_Δ = (1) 0.89

(2) 0.77

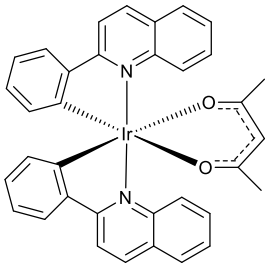

3

$\phi_\Delta = 0.89$

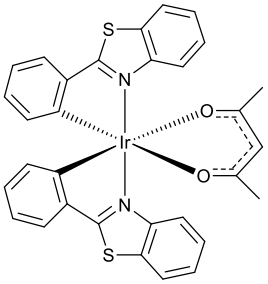

4

$\phi_\Delta = 1.00$

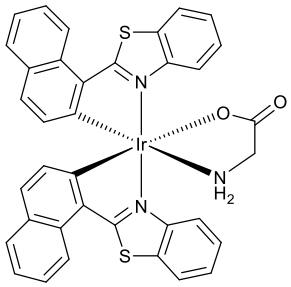

5

$\phi_\Delta = 0.81$

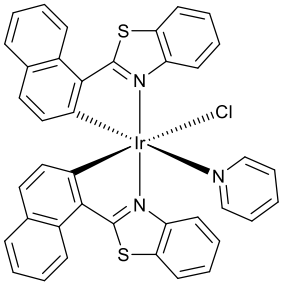

6

ϕ_Δ =1.00

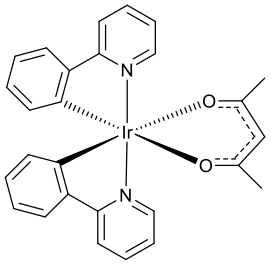

7

$\phi_\Delta = 0.90$

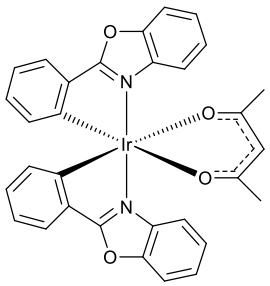

8

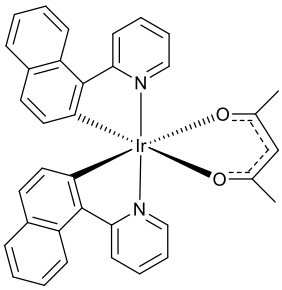

9

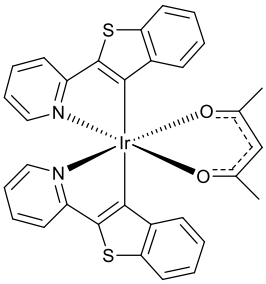

10

Figure 6- Initial cyclometalated Ir(III) complexes investigated for photosensitization of singlet oxygen

3.3.3 Cyclometalated Ir(III) complexes as PDT agents.

Although many Ir(III) complexes have been developed as PDT agents, many have one prominent drawback. As mentioned above, transition-metal based PDT agents have a short excitation wavelength. The following is a brief overview of approaches taken to rectify this problem in Ir(III) complexes.

Several groups have suggested attaching Ir(III) complexes with light-harvesting organic chromophores (Scheme 3). For example, Zhao *et al*. have synthesized Ir(III) conjugates with BODPIY dyes via π- conjugation linkers to harness NIR absorptions (**10a**, **10b**, **10c**, **10d**). [78,79] Martinez-Martinez also took a similar approach but opted to functionalize the ancillary ligand with the BODIPY dye (**11a**, **11b**). [25]

Despite the strategy, both classes of Ir-BODIPY conjugates show similar absorption bands and ISC from the singlet to triplet state was observed when illuminated with visible light.

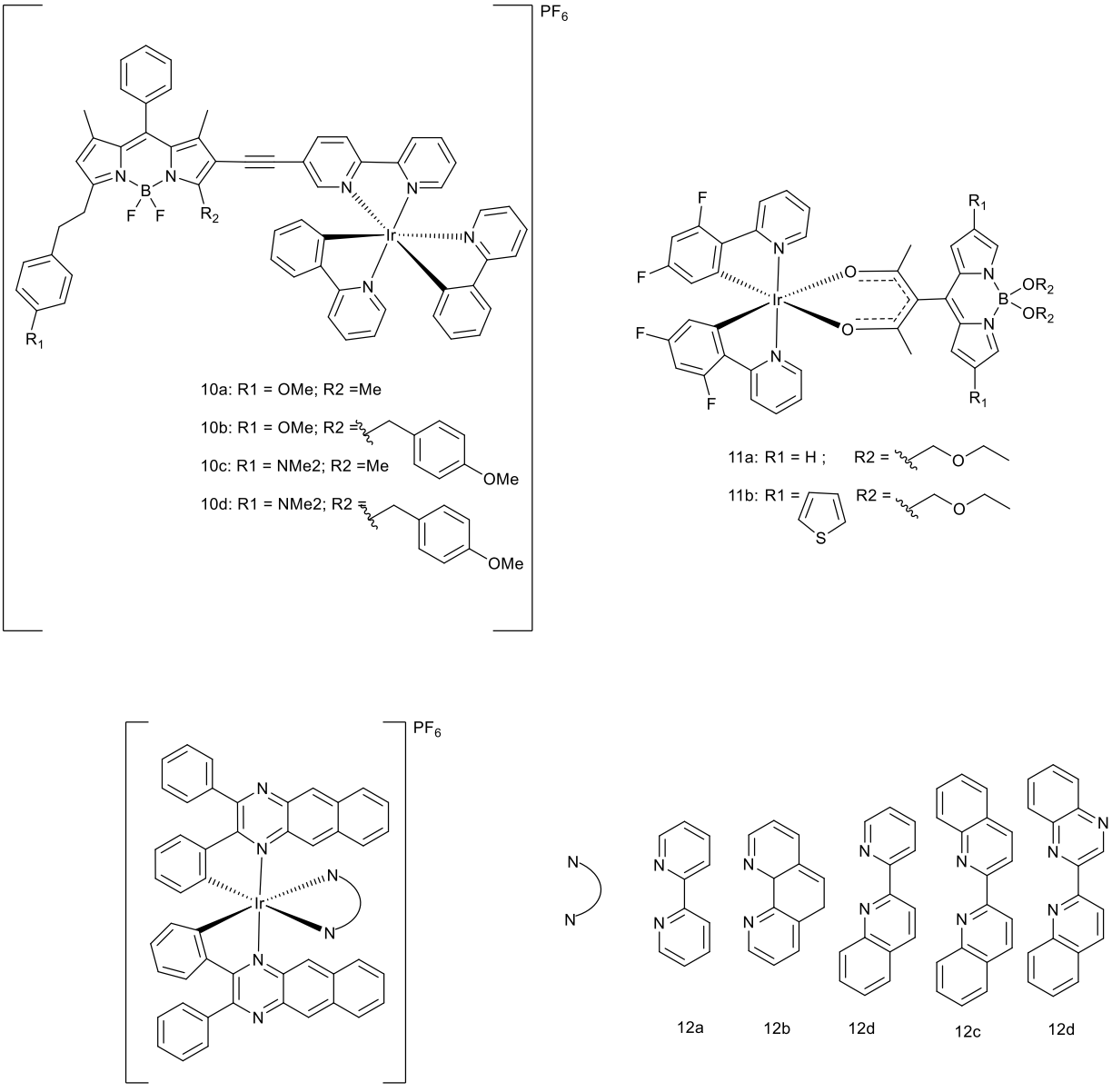

Scheme 3- Cyclometalated Ir(III) complexes synthesised for absorption in the NIR region

An alternate strategy is the use of ligands with extended π-systems. Similar to the previous approach, this results in long triplet lifetimes resulting in good PDT effects. Sun and McFarland reported five Ir(III) complexes (**12a**, **12b**, **12**, **12d**), each with increasing π-conjugation. They were able to demonstrate an increase in the intensity of the spin-forbidden ($b_{2g} \rightarrow e_g$ or $e_g \rightarrow e_g$) bands (600-800 nm) with increase in π-conjugation.[80]

Two-photon excitation is the process of exciting a molecule with two simultaneous photons. This allows for the use of two photons carrying half the energy that is required to populate the emissive excited state (Scheme 5). Two-photon excitation requires a high density of photons. The two-photon absorption process is proportional to the square of the photon intensity, reflecting the requirement for two photons of light to interact with the molecule simultaneously. The main advantage of this technique for PDT is that NIR excitation can be achieved without modifying the molecule. Two-photon excitation has been successfully demonstrated in confocal microscopy and provides an exciting new direction for PDT. McKenzie *et al*. demonstrated the efficacy of two photon PDT with the use of two Ir(III) complexes of $[Ir(ppy)_2]$ type with either a bisbenzimidazole (**13a**) or a N,N-dimethylated version (**13b**) of it. These compounds were previously shown to have effective PDT effects with one-photon excitation at 405 nm. These two complexes showed similar effects with NIR two photon excitation.[81]

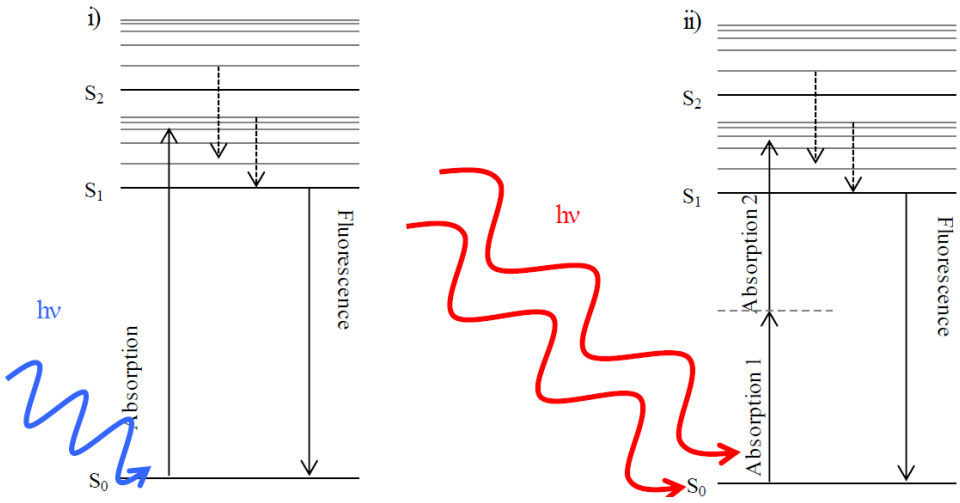

Scheme 4- One Photon Excitation (i) vs Two Photon Excitation (ii)

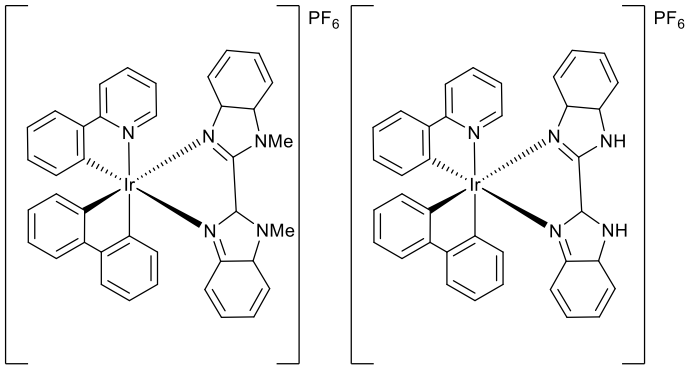

13b **13a**

Aims and Objectives

This project is based on the hypothesis that certain metal complexes are suitable for killing of microbes, more specifically *P.gingivalis*, when irradiated with light. From the literature it is clear that *P.gingivalis* is very resourceful and strategic in avoiding antibiotics and immune surveillance by tacking refuge inside host cells. It has also been shown by McKenzie *et al*. that **13a** is effective at localizing inside human cells followed by exiting cells after *ca.* 2 h, while doing little to no harm without light activation. The specific aims of the project are outlined below:

- To investigate the ability of current anticancer PDT agents, starting with **13a,** to act as antimicrobial PDT agents at doses that are harmless to human cells, with or without light.
- To investigate these potential antimicrobial PDT agents as dual optical/electron microscopy imaging probes for bacteria. This will also aid in studying the uptake and localizing of the metal complex by the bacteria.
- To synthesize novel transition metal based PDT agents specially tailored towards *P.gingivalis* and other bacteria, while looking to overcome the more broad shortcomings of transition metal PDT such as activation wavelength and solubility.

Chapter 2

Experimental Methods

2.1 Synthesis

Nuclear Magnetic resonance (NMR) spectroscopy

All ^{1}H NMR spectra were recorded on a 400 MHz Bruker Advance 400 spectrometer. NMR chemical shifts (δ) were determined relative to internal tetramethylsilane, Si(CH3)4 and are given in ppm. Spectroscopic grade deuterated NMR solvents were purchased from Sigma Aldrich.

2.1.1 Synthesis of 2-(2-methyl-5-nitro-1H-imidazol-1-yl)ethyl 2-phenylquinoline-4-carboxylate, compound (mdz-pqc).

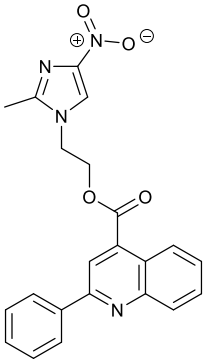

mdz-pqc

To a solution of 2-phenylquinoline-4-carboxylic acid (1.0 g,4 mmol), 2-methyl-5-nitroimidazole-1-ethanol (metronidazole)(1.03 g, 6 mmol), and 4-(dimethylamino)pyridine (0.15 g, 1.2 mmol) in dry dichloromethane (10 mL), N,N'-dicyclohexylcarbodiimide (0.99 g, 4.8 mmol 1.3 eq) was added upon stirring at room temperature. The resulting mixture was stirred for further 2 hours, which

resulted in formation of a white precipitate. Dicyclohexylurea (DCU) was filtered off and the filtrate was evaporated to dryness, resulting in a light yellow solid. The solid was redissolved in a minimum amount of dichloromethane (10 mL). Addition of hexane (30 ml) led to precipitation of a yellow solid, which was collected by filtration, washed with hexane, and dried *in vacuo*. The product was obtained as a light yellow solid (0.72 g, 93%). ^{1}H NMR (400 MHz, Acetone-d_6) δ 2,54 (s, 3H), 4.90 (t, $^{4}J_{HH}$ = 4 Hz, 2H), 4.98 (t, $^{4}J_{HH}$ = 4 Hz, 2H), 7.58 (m, 4H), 7.66 (ddd, $^{3}J_{HH}$ = 8.3, 6.9, 1.2 Hz, 1H), 7.85 (ddd, $^{3}J_{HH}$ = 8.8, 8.3, 5.4 Hz, 1H), 7.98 (s, 1H), 8.18 (d, $^{3}J_{HH}$ = 8.4 Hz, 1H), 8.32 (d, $^{3}J_{HH}$ = 7.0 Hz, 2H), 8.38 (s, 1H), 8.56 (d, $^{3}J_{HH}$ = 8.5 Hz, 1H) . HRMS (m/z): [M^{+}] calcd for $C_{22}H_{18}N_4O_4$ 402.41, found 403.1.

2.1.2 Synthesis of [Ir(mdz-pqc)$_2$(μCl)]$_2$

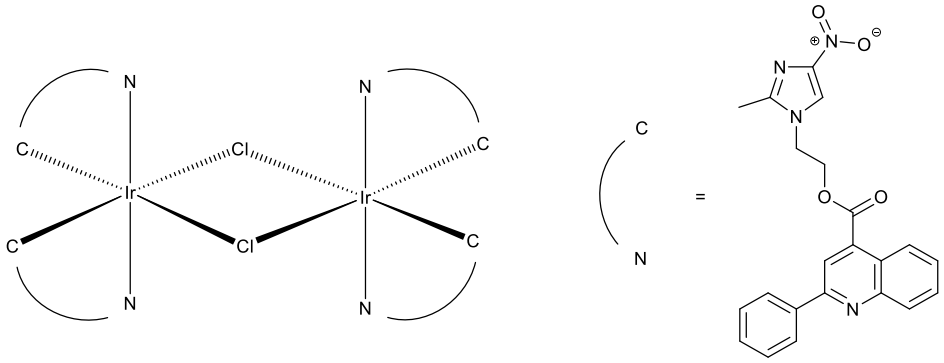

[Ir(mdz-pqc)$_2$(μCl)]$_2$

A mixture of 2-methoxyethanol and water (9 ml, 3:1), containing $IrCl_3$ •$3H_2O$ (0.20 g, 0.67 mmol 1eqv) and **mdz-pqc** (0.54 g, 1.39 mmol 2.02eqv) was refluxed under argon. Colour changes from pale yellow to red-orange observed after 30 minutes. The reflux was stopped after 48 hours, and

the reaction mixture allowed to cool down to room temperature. Water was added to the reaction mixture, leading to precipitation of an orange solid which was filtered and air-dried (0.14 g, 54%).^{1}H NMR (400 MHz, Acetone-d_6) δ 2,54 (s, 3H), 4.92 (t, J = 4 Hz, 8H), 4.99 (t, J = 4 Hz, 8H), 7.57 (m, 13H), 7.67 (ddd, 4H), 7.85 (ddd, 4H), 7.98 (s, 2H), 8.20 (m, 4H), 8.32 (m, 8H), 8.40 (s, 4H), 8.60 (dd, J = 17.9, 11.2 Hz, 4H). HRMS (m/z): [M^+] calcd for $C_{88}H_{68}Cl_2Ir_2N_{16}O_{16}$ 2060.94, found 1031.24.

2.1.3 Synthesis of 2,2'-bisbenzimidazole

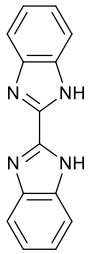

2,2'-bisbenzimidazole

O-Phenylenediamine (0.54 g 0.005 mol) and oxalic acid (0.225 g, 0.0025 mol) were added to ethylene glycol (6 mL) in a 10 mL microwave tube. Polyphosphoric acid (1 mL) was added to the mixture. The vessel was irradiated with microwaves at 160 °C for 30 min. After allowing to cool room temperature the pH was adjusted to pH 10. The resulting precipitate was filtered and washed several times with water until the water emerged at neutral. A light green precipitate was obtained (0.9g, 77% yield). ^{1}H NMR (400 MHz, DMSO) δ 13.55 (s, 1H), 7.76 (d, $^{3}J_{HH}$ = 7.6 Hz, 1H), 7.56 (d, $^{3}J_{HH}$ = 7.8 Hz, 1H), 7.36 – 7.24 (m, 2H) HRMS (m/z): [M+] calcd for $C_{14}H_{10}N_{4,}$ 234.09; found 234.26.

2.1.4 Synthesis of [Ir(mdz-pqc)$_2$(bbzH$_2$)]Cl, Complex 14

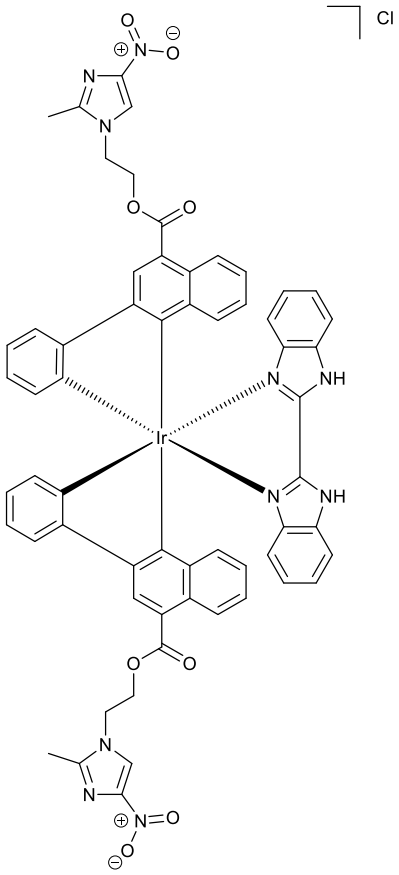

Complex 14

A suspension of **[Ir(mdz-pqc)$_2$(μCl)]$_2$** (0.14 g, 0.07 mmol, 1.0 eqv) and **2,2'-bisbenzimidazole** (0.03 g, 0.12 mmol 2.1 eqv) was dissolved in a mixture of methanol and dichloromethane (20 mL, 1:1) and refluxed at 65 ^{o}C under a positive pressure of argon for 24h. The reaction mixture was rotary evaporated to dryness, and the solid residue was redissolved in a minimum volume of dichloromethane (5 mL). Addition of hexane (10 mL) resulted in precipitation of a light-green solid, which was filtered. The solid was purified using HPLC using 40% THF in water (plus 0.1% TFA) as the eluant. The residue was filtered off and the filtrate was concentrated to obtain a

green precipitate (60 mg, 10%). ^{1}H NMR (400 MHz, Acetone-d_6) δ 4.90 (t, 4H), 4.97 (t, 4H), 7.54 (m, 6H), 7.67 (ddd, 2H), 7.82 (ddd, 2H), 7.98 (s), 8.19 (m, 2H), 8.32 (m, 4H), 8.40 (m, 1H), 8.61 (m, 2H). HRMS (m/z): [M^+] calcd for $C_{58}H_{44}ClIrN_{12}O_8$ 1229.3, found 1230.3.

2.1.5 Synthesis of $[Ir(pqc)_2(\mu Cl)]_2$

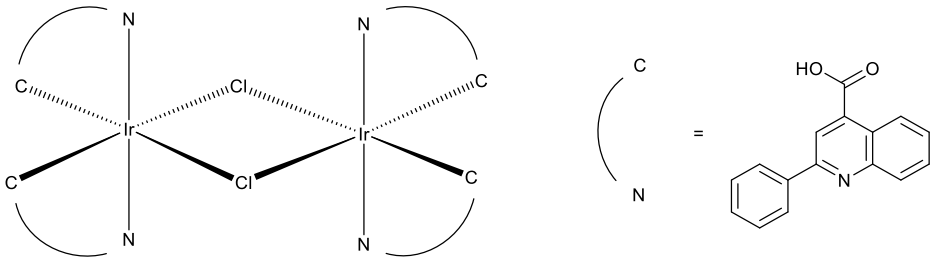

$[Ir(pqc)_2(\mu Cl)]_2$

A mixture of 2-methoxyethanol and water (9 ml, 3:1), containing $IrCl_3 \bullet 3H_2O$ (1.0 g, 3.35 mmol 1eqv) and 2-phenylquinoline-4-carboxylic acid (1.75 g, 8.61 mmol, 2.1eqv) was refluxed under argon. A dark purple precipitate for observed after 5 hours. Reflux was stopped after 48 hours, and the reaction mixture allowed to cool down to room temperature. Water was added to the reaction mixture, leading to precipitation of a dark purple solid which was filtered and air-dried (0.23g, 9.6%).

2.1.6 Synthesis of [Ir(pqc)$_2$(bbzH$_2$)]Cl, Complex 15

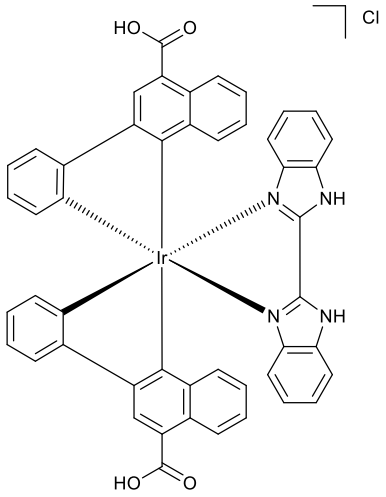

Complex 15

A suspension of **[Ir(pqc)$_2$(μCl)]$_2$** (0.0989 g, 0.07 mmol, 1.0 eqv) and **2,2'-bisbenzimidazole** (0.03 g, 0.12 mmol 2.1 eqv) was dissolved in a mixture of methanol and dichloromethane (20 mL, 1:1) and refluxed at 65 ^{o}C under a positive pressure of argon for 48 h. The reaction mixture was rotary evaporated to dryness, and the solid residue was redissolved in a minimum volume of dichloromethane (5 mL) and precipitated in hexane (20 mL). The precipitate was filtered and purified in a Sephadex column using MeOH the eluent to obtain a red precipitate (14.40 mg, 10.3%). ^{1}H NMR (400 MHz, MeOD) 7.57 (m, 8H), 7.76 (m, 3H), 7.82 (d, 4H), 813 (d, 5H), 8.44 (d, 2H). HRMS (m/z): [M^{+}] calcd for $C_{48}H_{30}ClIrN4O_4$ 919.19, found 920.19.

2.2 Bacterial growth and culture

P. gingivalis (W50 or NCTC 11834) was grown and maintained fastidious anaerobe agar medium (FA; LabM, UK). The agar was treated with oxalated horse blood (Oxoid, UK) 5% (v/v). An anerobic cabinet (10% H_2, 10% CO_2, and 80% N_2) at 37 ˚C was used for bacterial growth and incubation. The bacteria were allowed to grow for 3 days (unless otherwise state) prior to starting the experiments.

P. aeruginosa (PA01) was grown and maintained on Leria-Bartani (LB) agar (Miller) at 37 ˚C in an aerobic incubator for 24 hours prior to starting the experiments.

2.3 Cell lines

Cell line	Genotype	Reference
H357	Epithelial squamous cell carcinoma	[82]
HEK293	Human embryonic kidney cells	[83]
HEP-G2	Human hepatocellular carcinoma	[84]

2.4 Cell culture

Dulbecco's modified Eagle's medium (DMEM) (Sigma) is a cell culture growth medium containing various nutrients including vitamins and amino acids necessary for the growth of cells *in-vitro* (full composition of DMEM is listed in the appendix).[85] DMEM was supplemented with 5 mL L-glutamine (200 mM solution), 50 mL fetal calf serum (10%) was used to culture cells in standard T-75 flasks (a narrow necked flask made of polystyrene with an adherent inner surface). Cells were incubated 37 °C in an atmosphere of 5% CO_2 / 95% air. Cells were allowed to reach ~90%

confluency prior to experiments. Cells were washed with PBS and subcultured using Trypsin EDTA (2 mL).

2.5 Bacterial Colony Forming Unit (CFU) assay

The bacterial solution was serially diluted (10^{-1}-10^{-4}) and placed on Fastidious Anaerobe (FA) agar as 5 µL triplicates and incubated for 4-5 days.

2.6 PDT experiments on *P.gingivalis* and *P.aeruginosa*

1 ml *P.gingivalis* (W50 or NCTC 11834) or *P.aeruginosa* suspensions with a chosen optical density 0.5 OD_{600} (for *P.gingivalis*) and 0.1 OD_{600} (for *P.aeruginosa*) in PBS were made. The suspension was split into a glass vials (for irradiation) and an Eppendorf tubes (dark control). The suspensions were treated with a known concentration (concentrations used are indicated in the main body) of either metal complexes or pure metronidazole. Two more suspensions in a glass vial were treated with pure PBS. One of these was kept in the dark while the other was irradiated. All vessels were wrapped in foil and all samples were allowed to incubate in an anaerobic cabinet (for *P.gingivalis*) or an aerobic incubator (for *P.aeruginosa*). The suspension in the glass vials were irradiated with a laser diode (ThorLabs M405L3 - 405 nm) (405 nm, 20 $mWcm^{-2}$, 3 min). The contents of the all vessels were pipetted onto fresh agar plates for CFU counting.

2.7 Cell toxicity and PDT experiments

Two 96-well plates were seeded with 10000 cells/well (100 µL) and left to incubate overnight. Both plates were treated with varying concentrations of the complex (0-1000 nM, 100 µL) or equivalent DMSO control (0.2%) and incubated for 2 hours. Cells were washed with PBS (1 x 3mL). The cells were treated with DMEM (without phenol red and L-glutamine + 10% FCS, 100 µL). One plate was treated with light (405 nm, 20 $mWcm^{-2}$, 3 minutes). The other plate was

wrapped in foil and kept in the dark. Both plates were allowed to incubate overnight. The wells were washed with PBS and replaced with fresh DMEM (w/o phenol red and L-glutamine + 10% FCS, 100 µL). 3-(4,5-dimethylthiazol-2yl)-2,5-diphenyltetrazoliumbromide (MTT) (30 µL) was added to each well and incubated for 24 h. The formazan crystals were dissolved by carefully removing the media and dissolving the crystals in DMSO (50 µL). Optical density of the wells were recorded at 540 nm on a plate reader (Tecan, Infinite® 200 PRO plate reader) .

2.8 Invasion assay

All experiments were performed in triplicate. A previously reported antibiotic protection assay was modifed.[86] H357 cells were seeded onto a 24 well plate (9 wells in triplicates plus two more for cell counting) at 8 x 10^4 cells/ ml with 1 mL of cell suspension per well and incubated for 3 days. On the 3rd day the two wells for cell counting were washed with PBS (2 x 500 µL), trypsinised (500 µL, trypsin-0.02% EDTA) and neutralized with growth media (500 µL, DMEM with 10% FCS) after cell detachment. Three-day old plate-cultured *P.gingivalis* were transferred to centrifuge tube with growth media (DMEM with no added supplements). The bacterial concentration adjusted to a multiplicity of infection 1:100, i.e. every human cell is to be exposed 100 bacterial cells. The wells seeded with cells were washed with PBS (2 x 500 µL). The bacterial solution above was added to each well (500 µL/ well) and incubated for 90 minutes. A further triplicate of wells with the original inoculate were also incubated alongside the cells (viability wells). These three wells were left untreated until the end of the experiment. The wells were washed with PBS (3 x 500 µL). The extracellular bacteria were killed by treating each well with metronidazole (200 µg/mL, 500 µL) and incubating at 37^{o}C, 5% CO_2 for 1 hour.

The metronidazole was removed by washing with PBS (3 x 500 µL). Each triplicate was then treated with either DMEM, **3** (5 nM in DMEM) or **3** (1000 nM in DMEM) and incubated for at 37°C, 5% CO_2 for 2 hours. The wells were removed of **3** or DMEM and washed with PBS and replaced with DMEM (w/o phenol red and L-glutamine). Each well was then treated with 405 nm light for 3 mins at 20 $mWcm^{-2}$. The wells were washed with PBS (3 x 500 µL). The cells were lysed by adding sterile distilled water (200 µL/well), scraping with a pipette tip for 45 s followed by aggressive aspirating. The lysates and the viability wells were then serially diluted and plated for colony counting. Colony forming units were counted after 4 days of incubation. The number of internalised bacteria can be expressed as a percentage of CFUs in the original inoculum.

$$\%\ invasion = \frac{CFUs\ in\ DMEM\ control}{CFUs\ in\ original\ inoculum} \text{ x } 100$$

2.9 Biofilm toxicity and PDT experiments

2.9.1 Growth of biofilms

To grow biofilms *P.gingivalis* from the agar plate was inoculated to brain heart infusion (BHI) liquid nutrient broth (components in the appendix) and the OD_{600} adjusted 0.5 OD_{600} (for *P.gingivalis*) and 0.1 OD_{600} (for *P.aeruginosa*) before transferring 1 mL of the bacterial solution into wells of a 24 well tissue culture plate (Greiner CELLSTAR®). The 24 well plate was allowed to incubate in the above anaerobic conditions for 5 days (for *P.gingivalis*) or 24 h for (for *P.aeruginosa*). The presence of biofilms was confirmed with crystal violet stain.

2.9.2 Photodynamic therapy

All experiments were performed in triplicate. Two 24 plates with biofilms were used for each experiment (for irradiation and dark controls). Three wells of each plate were treated with either PBS (1 mL), 14 (concentrations as stated in discussion) or metronidazole (1 mL, 10 nM) (only for

P.gingivalis). Three extra wells of the dark control plate were treated with industrial methylated spirit (IMS) The biofilms treated IMS was used as the positive control as it is assumed IMS will destroy all biofilms. The plates were allowed to incubate in the dark in an anaerobic cabinet or aerobic incubator for 2 hours. Following removal of the plate cover, each well of the 'light control' plate was irradiated for 3 minutes 405 nm light at 20 $mWcm^{-2}$ with the focal point focused on the centre of the well. All wells of both plates were washed with 2 x 1 mL PBS before being treated with LIVE/DEAD® BacLight™ stain and allowed to incubate in the dark for 15 minutes. Optical density of wells at was recorded on a plate reader (Multiskan fc, Thermo Fisher Scientific, Warrington, UK).

2.10 3D – Skin models

2.10.1 Model preparation

Biopsy samples from Euroskin™ were placed in 1 M NaCl (enough to cover the entire skin) and incubated overnight at 37 °C. The sample was poured into a sterile petri dish. The epidermis was separated from the dermis using blunt forceps to obtain a decellularized dermis (DED). The DED was incubated at 37 °C for 48 hours with DMEM to flood the sample with growth medium. The sample was then transferred to fresh DMEM and stored at 4 °C until needed. To construct the skin, the DED was cut into approximately 6 x 12 mm circular samples using a sterile cork-borer and inserted into tissue culture inserts. The inserts were placed in a 12 well plate. The DED was then seeded with 1×10^5 fibroblasts and 3×10^5 skin keratinocytes each in 250 µL of serum free DMEM/2ng/ml TGFa (plus penicillin and streptomycin/fungizone). The surrounding area around the insert was filled with 1 mL of the same medium. The samples were allowed to incubate for 24 hours at 37 °C before replacing the growth medium. After a further 24 hours of incubation the

medium was removed and fresh medium was added to the base of the skin construct so that it forms an air-liquid interface. The medium was replaced ever 2-3 days for 14 days. The medium was switched to an antibiotic-free medium 72 hours before the experiment.

2.10.2 Infection and PDT experiment

An overnight culture of *P.aeruginosa* was adjusted to 1 x 10^6 bacteria in Lysogeny broth (LB) broth. Incisions on the skin constructs were made using a heated metal inoculating loop. Each construct was infected with 20 µL of the above bacterial solution and allowed to incubate for 24 hours. The samples were washed with PBS (3 x 1 mL). The samples were separated into 2 sets of 3 in 2 12-well plates (for either irradiation or to be kept in the dark). Each sample was treated with either PBS (1 mL) or complex **14** (2 µM or 20 µM, 1mL). Both plates were allowed wrapped in foil and allowed to incubate for 2 hours in an aerobic incubator. 3 samples in one plate was irradiated with light (405 nm, 40 $mWcm^{-2}$, 15 minutes). Samples in both plates were then washed with PBS and weighed. The samples were shredded using sterile scalpels and vortexed in PBS (1 mL) for 1 min. The vortexed PBS was serially diluted to and plated for CFU counting. The bacterial counts were expressed as CFU/mL/mg.

2.11 Confocal microscopy

2.11.1 Planktonic bacteria - sample preparation

For *P.gingivalis* (NCTC 11834) (at a concentration of 0.5 OD_{600}) the bacteria were treated with (1 mL, concentrations as specified in main text) of **13a** or **14** and incubated for 2 hours in an anaerobic cabinet. For *P.aeruginosa* (at a concentration of 0.1 OD_{600}) the bacteria were treated with **14** (1 mL) and incubated for 2 hours in an aerobic incubator. Both bacterial species were washed with PBS (3 x 1 mL) before being fixed in 4% paraformaldehyde for 30 minutes. The

bacteria were re-washed with PBS (3 x 1 mL) and deionised water (1 x 1 mL). The samples were mounted on to microscope slides using SlowFade™ Gold Antifade Mountant (Thermo Fisher).

2.11.2 Biofilms- sample preparation

Biofilms of both *P.gingivalis* (NCTC 11834) and *P.aeruginosa* were grown on 35 mm glass bottom imaging dishes (Ibidi) with the same procedure as for PDT experiments. The biofilms were treated with varying concentrations of **14** and incubated in an anaerobic cabinet (for *P.gingivalis*), or an aerobic incubator (for *P.aeruginosa*). The samples were washed with PBS (3 x 1 mL) before being fixed in 4% paraformaldehyde for 30 minutes. The bacteria were re-washed with PBS (3 x 1 mL).

2.11.3 Imaging

Confocal microscopy was performed using the Nikon A1 microscope with an excitation of 403.55 nm and emission filters set at 450/25, 525/25 and 595/2. Images were processed using ImageJ.

2.12 3D Structured illumination microscopy

2.12.1 Fixed cells

P.gingivalis (NCTC 11834) (at a concentration of 0.5 OD_{600}) the bacteria were treated with of **13a** (10 nM, 1mL) or **14** (10 nM or 20 μM, 1 mL) and incubated for 2 hours in an anaerobic cabinet. The samples were washed with PBS (3 x 1 mL) before being fixed in 4% paraformaldehyde for 30 minutes. The bacteria were re-washed with PBS (3 x 1 mL) and deionised water (1 x 1 mL). The samples were mounted on to microscope slides using SlowFade™ Gold Antifade Mountant (Thermo Fisher).

2.12.2 Live cells

P.gingivalis (NCTC 11834) (at a concentration of 0.5 OD_{600}) were treated with **14** (10 nM, 1 mL) in a 35 mm glass bottom imaging dishes (Ibidi) and incubated for 2 hrs in an anaerobic cabinet. The bacteria were resuspended in PBS (1mL). The sample was treated with BacLight LIVE/DEAD Bacterial Viability Kit (L7012, Thermo Fisher) according to manufacturer's instructions.

2.12.3 Imaging- Fixed cells

3D SIM images were taken on the GE Deltavision OMX with the excitation wavelength set at 405 nm with the detection filter set to 528/48.

2.12.4 Imaging- Live cells

3D SIM images were taken on the GE Deltavision OMX. The sample was initially irradiated with the 405 nm (3 min) line to activate the complex. Images were then collected then taken for 30 minutes with an excitation of 488 nm with a filter set of 528/48 and 609/37.

2.13 Transmission Electron Microscopy

Two experiments were designed. In the first experiment, *P.gingivalis* samples were treated with varying concentrations of **13a** or **14** (0 - 1000 nM) and incubated for 2 hrs. The samples were washed with PBS (3 x 1 mL), and fixed in 3% glutaraldehyde in PBS. The samples were then dehydrated, embedded in Araldite resin, sectioned and imaged. Only OsO_4 was used as a conventional contrasting agent. Therefore, any increase in contrast can be attributed to the complex.

The second experiment was designed to study damage caused by **14** on *P.gingivalis*. The bacteria were treated with **14** as above and incubated for 2 hours and treated with light (405 nm, 20 mW cm^{-2}, 3 min). The samples were washed with PBS (3 x 1 mL) before being fixed in 3%

glutaraldehyde in PBS. The samples were then dehydrated and embedded in Araldite resin and treated with OsO_4, lead citrate and uranyl acetate before sectioning and imaging with TEM. TEM imaging was carried out using a FEI tecnai 120Kv G2 Biotwin TEM with an Orius SC100 bottom mounted camera using Gatan Digital Micrograph software.

Chapter 3

Development of a novel antimicrobial PDT agent

The ability of *P.gingivalis* to invade and hide in host cells and avoid any host immune response or antibiotics presents a major problem.[37] Therefore, any prospective transition metal PDT agent must have the additional ability of crossing the human cell membrane. One such complex was synthesized by Prof Gareth Williams, Durham University and has been heavily investigated by Prof Julia Weinstein and Dr Helen Bryant as potential one- and two- photon anticancer PDT agents.[81] This chapter will consist of two parts. First part will discuss screening for a potential antimicrobial PDT candidate based on previously studied anticancer PDT agents. The second part will be the synthesis of a new antimicrobial PDT complex

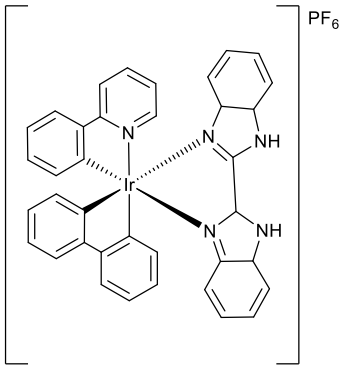

13a

Figure 7- Chemical structure of 13a, a complex previously investigated as an anticancer PDT agent

3.1 An anticancer Iridium complex for antimicrobial PDT

In tandem with the PDT investigations, **13a** has also been studied for its use in optical imaging. Extensive studies carried out by Dr Jonathan Shewring using super-resolution microscopy (3D Structured Illumination Microscopy) shows that the localisation pattern on **13a** changed over a period of 24 hours, following the 2 hour incubation with **13a**.[87] The images recorded after 15 min showed uniform staining of the cytoplasm. Overtime, this staining disappeared giving rise to more punctate staining. At the 2h mark, there was a mixed cytoplasmic and punctate (spot-like) staining. The staining pattern was attributed to the pH sensitive nature of the complex and was therefore likely that its protonated form was trapped by lysosomes, which possess a pH of ~ 4.5.[88]

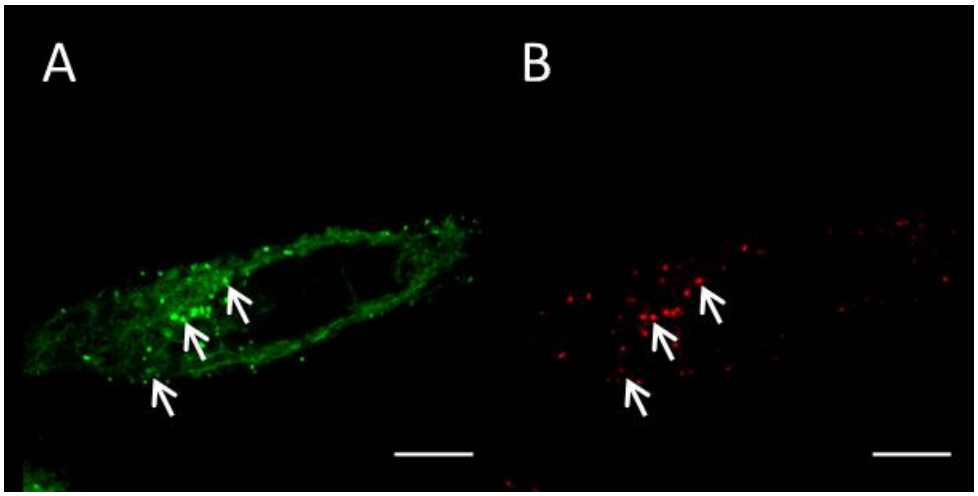

Figure 8- LSCM images of live HeLa cells treated with complex 13a (10 µM, 2 h) and LysoTracker™ Red (50 nM, 35 mins) with lysosome staining pattern highlighted by white arrows (A) emission from complex 13a (λex = 405 nm), (B) emission from LysoTracker™ Red (λex = 561nm). Scale bar = 10 µm (From J. R. Shewring PhD thesis)

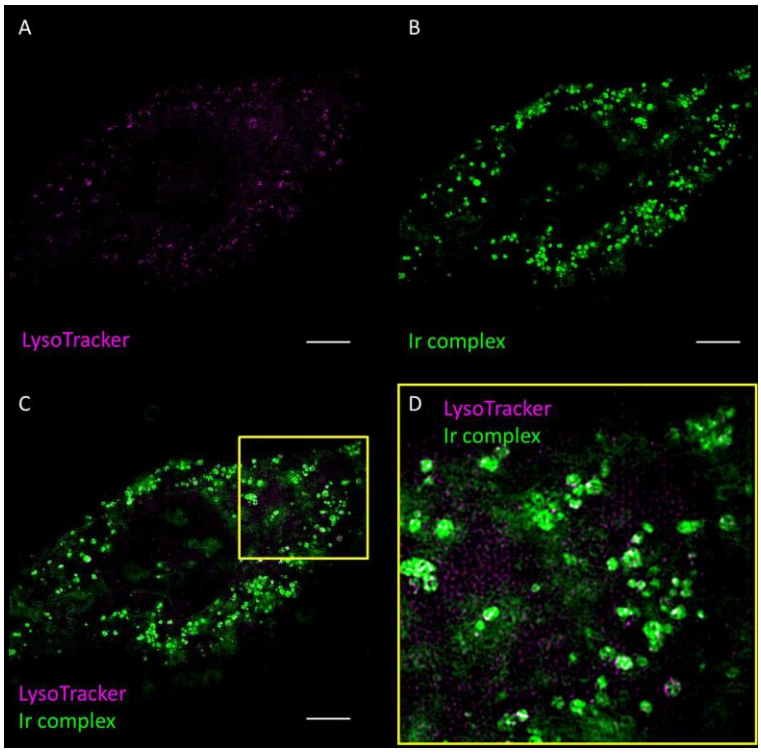

Figure 9 - 3D SIM images of fixed HeLa cells stained with complex 13a (10 µM, 2 h) and LysoTracker™ Red (50 nm, 35 mins) (A) Lysotracker emission(λex = 561 nm), (B) Complex 13a emission(λex = 405 nm), (C) Overlay of A and B, (D) zoomed in ROI demonstrating colocalisation of the Lysotracker and complex 4.6 seen as white areas. (Scales bar = 3 µm) (From J. R. Shewring PhD thesis)

A colocalization study with Lysotracker™ Red confirmed this hypothesis as shown in Figure 8 and Figure 9. These studies confirm the uptake of **13a** by human cells, and provided evidence for changing localisation of the compound inside the cell. Furthermore, the work of Dr Luke McKenzie demonstrated the ability of cells to effectively begin excreting **13a** after 30 minutes (Figure 10).[81]

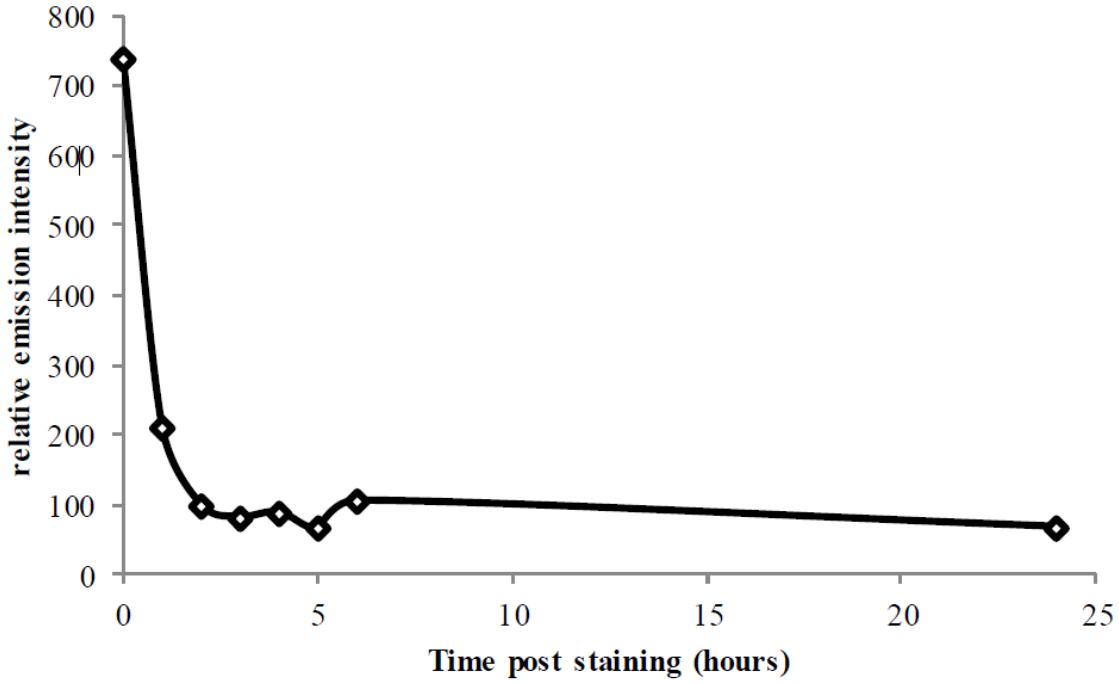

Figure 10 - Depletion data, cells were incubated with 13a (10 μM, 2 h) before fresh media was added. The cells were then fixed at varying times post staining (From L. K. McKenzie PhD thesis)

The PDT properties were confirmed by the clonogenic assay (an assay used to quantify the number of living cells following a toxicity experiment). The upper limit for dark toxicity was shown to be 100 μM, although dark toxicity studies at higher concentrations was restricted by the need to use more than 2% DMSO to dissolve the complex – thus, it is likely that the compound is not toxic in the dark at much higher concentrations. Compound **13a** demonstrated its ability to induce high levels of cell death (Figure 11) when irradiated with a 405 nm light at 20 $mWcm^{-2}$. The closely related compound **13b**, which carried a methylated N-atom on the bis-benzimidazole ligand vs. H-atom in **13a**, showed light toxicity similar to **13a**, but was also found to be highly toxic in the dark (60% cell death observed at 0.01 mM) (Figure 11). Therefore, the methylated derivative **13b** was not studied further.

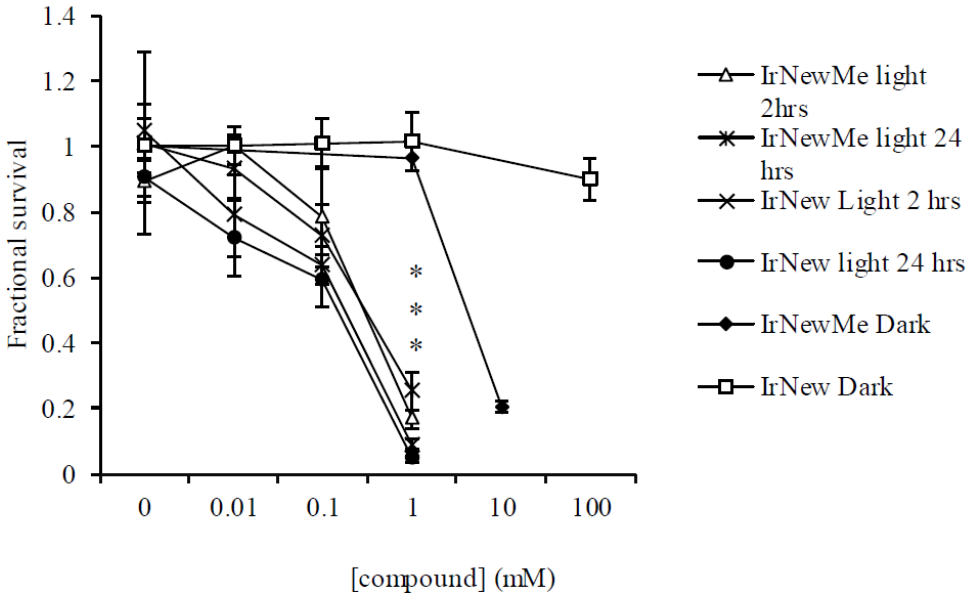

Figure 11 - Long term cell survival of HeLa cells following incubation with 13a or 13b) after treatment with light (405 nm, 3 mins, 20mWcm^{-2}) or kept in the dark (From L. K. McKenzie PhD thesis).

The previous studies were conducted on HeLa cells. In order to investigate the potency of **13a** towards killing bacteria in gums, we replicated the studies of **13a** light toxicity on H357 (human oral squamous cell carcinoma) cells, which are more relevant to this project (Figure 12). H357 cells were chosen as they are routinely used in the invasion assays using *P.gingivalis*. The invasion assay in necessary to determine the PDT effect on internalised bacteria (discussed below). MTT assay was used for toxicity studies due to its time efficiency. The results show that H357 cells are slightly more sensitive to treatment with **13a** and 405-nm light than HeLa cells. The slight difference in results could also be attributed to the difference in toxicity assays used. However, **13a** follows a similar dark and light toxicity pattern in both cell lines; 20% of cell death started to

occur at ~ 0.01 µM and the survival fraction halved at 0.1 µM in the irradiated samples (Figure 12).

These results clearly indicated the ability of **13a** to successfully enter human cells, show minimum dark toxicity and most importantly show PDT effects in the presence of light. This, therefore, presented a solid starting point for the development of antimicrobial PDT agents.

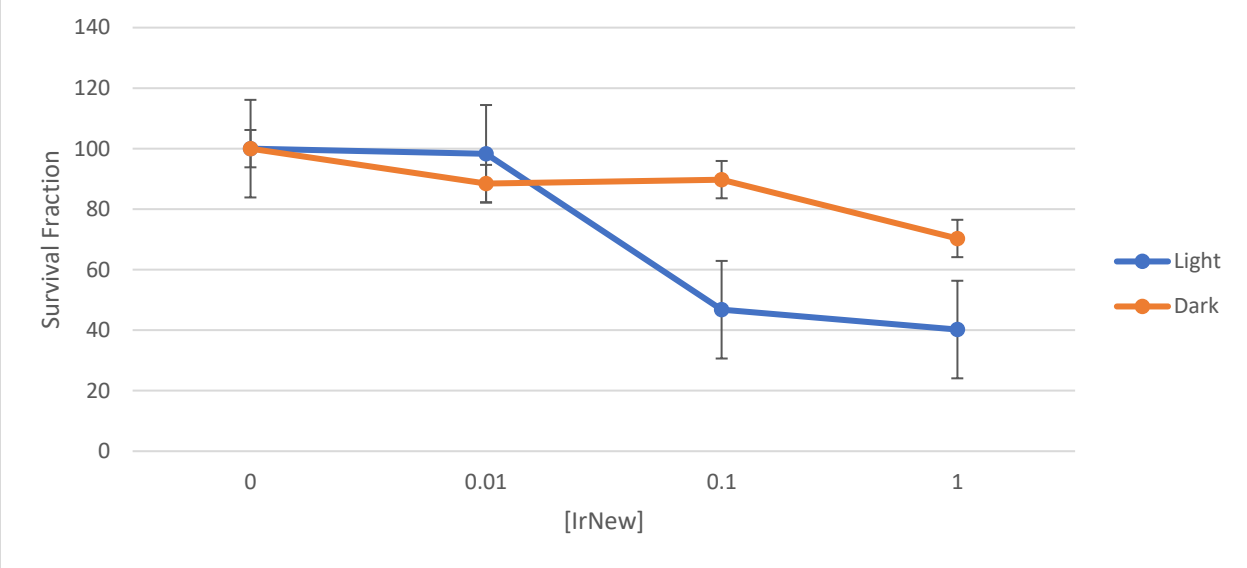

Figure 12- Survival of H357 cells after incubation with 13a (2 h) after treatment with light (405 nm 3 min, 20 mW cm-2) or kept in the dark. Data obtained using MTT assay (n = 3).

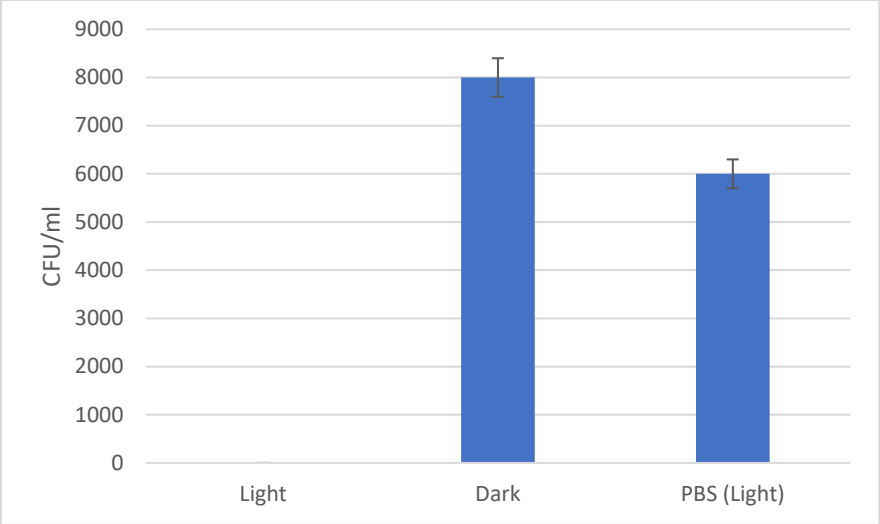

Figure 13 - Survival of P.gingivalis (0.1 OD at 600 nm) after incubation with 13a (2 h) followed by treatment with light (405 nm, 3 min, 20 mW cm^{-2}) (n = 3).

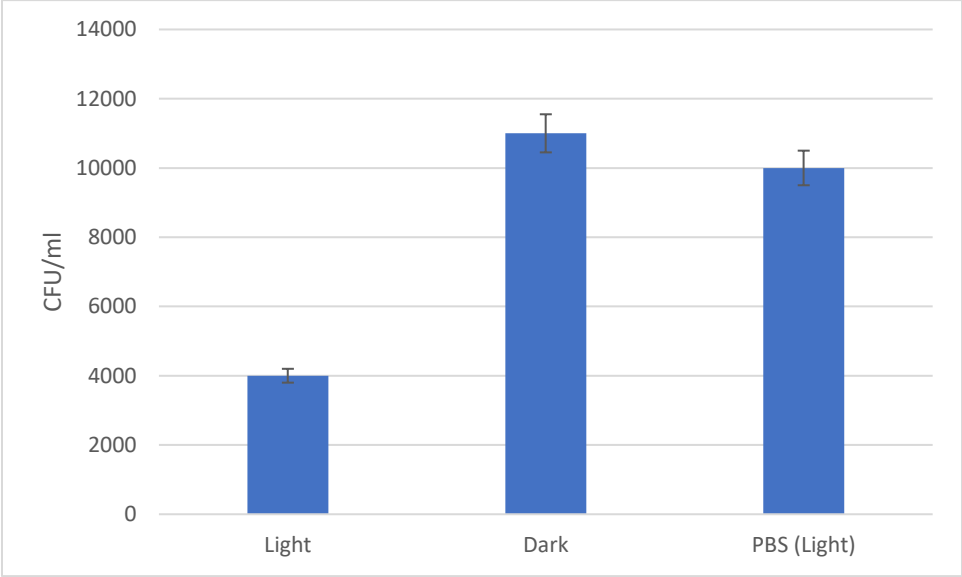

Figure 14 - Survival of P.gingivalis (0.2 OD at 600 nm) after incubation with 13a (5 nM, 2 h) followed by treatment with light (405 nm 3 min, 20 mW cm^{-2}) (n = 3).

3.2 The effect of 13a on *P.gingivalis*

Compound **13a** with a concentration of 5 nM was tested on *P.gingivalis*. According to Figure 11 and Figure 12**, 13a** at this concentration has no effects on human cells in the presence or the absence of light. Due to their smaller size and less sophisticated cellular structure, we hypothesised that bacteria will be more sensitive to **13a** than human cells. This would allow the use of the same complex without any modifications to kill bacteria without any adverse effects on host cells. The experimental conditions previously used for cell killing studies were modified for bacterial studies, as follows. A bacterial concentration of 0.1 OD_{600} was used. Bacteria were incubated with a solution of **13a** (5 nM) for 2 hours. This was followed by irradiation with 405 nm light, and CFU assays. The results, shown in Figure 13**,** indicate significant light toxicity of **13a** for *P.gingivalis* at 5 nM concentration, at which no light toxicity was detected for cells. Therefore, our results proved that the bacteria are indeed more sensitive to light activated **13a** than cells are.

The colonies of sample treated with **13a** and light were completely irradicated whereas the sample kept in the dark was unharmed, showing lack of dark toxicity. The absence of dark toxicity in antimicrobial-PDT may be pivotal to prevent the development of resistance towards potential aPDT agents in the future. A sample treated with only PBS was also treated with light (405 nm, 20mWcm^{-2}, 3 min). The 20% decrease in colonies of this sample was attributed to the damage done by the laser diode alone. Indeed, treating periodontal disease with the use of UV alone (310 nm) light has been suggested in the literature, although the effectiveness of this technique is not conclusive.[89,90]

The experiment was repeated at a higher bacterial concentration of 0.2 OD_{600}. The results are shown in Figure 14. The killing pattern is similar to that of experiments with 0.1 OD_{600}. However, due to overall increase in the number of bacteria in the initial inoculant, the overall bacterial count has increased.

3.3 Microscopy studies with 13a

3.3.1 Confocal and super-resolution microscopy.

Iridium(III) complexes have attracted interested as biological probes in the past decade. The work of Shewring *et al* mentioned above demonstrated the ability of iridium (III) complexes to be used as luminescent probes for confocal and 3D SIM imaging of cells.[91] Consequently, this can be extended into studying the localisation pattern of **13a** in bacteria. The bacteria were treated with **13a** (10 nM, 2 h), fixed in 4% in paraformaldehyde (PFA) and mounted on to a slide. Clear bacterial emissions were observed using 405 nm excitation and is shown in Figure 15. However, due to the smaller size of bacteria, bacterial morphology or localisation patterns of **13a** could not be elucidated with confocal microscopy due to insufficient spatial resolution.

Further structure and localisation information was pursued using 3D-SIM microscopy. The rejection of out-of-focus light along the z-axis caused by small precipitates, due to the poor solubility of the complex, proved to be an obstacle in the 3D construction of the image. Nevertheless, a rough idea of localisation was obtained using a z-slice of a SIM image (Figure 16), which indicates accumulation of **13a** along the bacterial cell wall and concentrating in cytoplasm.

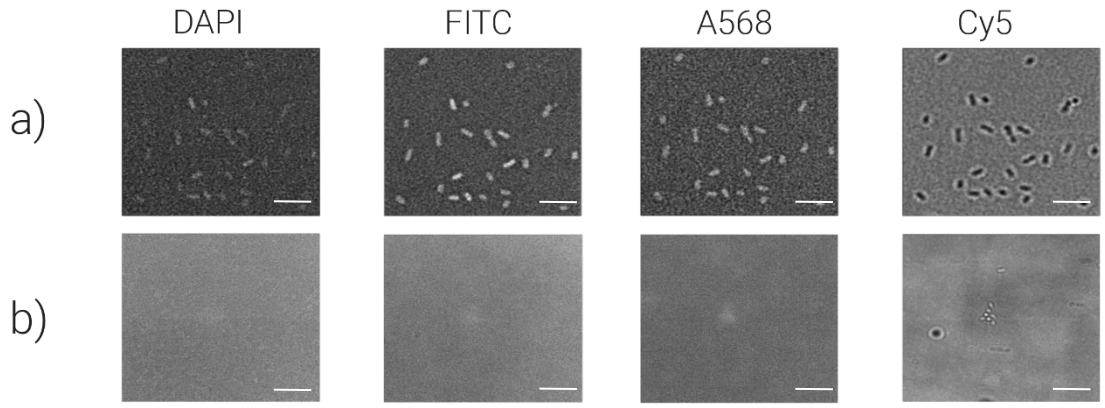

Figure 15 - Confocal images of P.gingivalis (λ_{exc} = 405 nm). a) stained with 13a (10 nM, 2h). b) PBS. The images show the uptake of 13a by P.gingivalis as the bacteria can only be seen in the samples treated with 13a and not with PBS scale bar = 6 µm

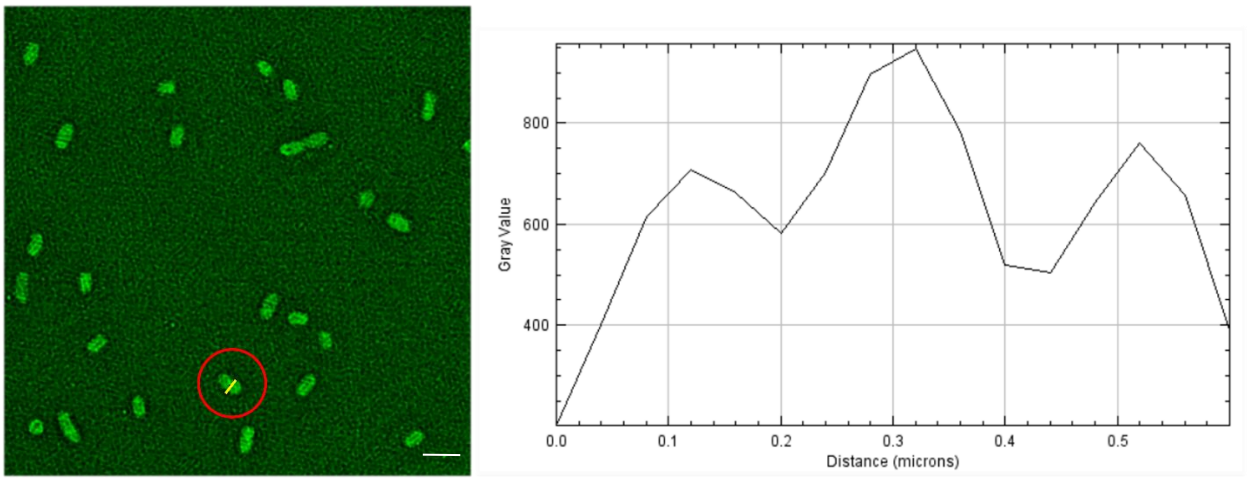

Figure 16 - A single z-slice of P.gingivalis SIM image of P.gingivalis (left) and emission lines (right) along the yellow line on the left, indicating uptake of the metal complex by bacteria. scale bar = 6 µm

3.3.2 Electron Microscopy

Due to their electron rich nature, transition metal complexes have the ability to scatter electrons and enhance contrast in electron microscopy. Despite this potential, only a few transition metal complexes have been studied for contrast enhancement in electron microscopy of cells, and none for studying bacteria.[92] With an increase in interest in correlative microscopy, the potential for **13a** to be a dual probe for both optical microscopy and electron microscopy was investigated. Furthermore, if successful, the high resolution of electron microscopy would allow for a better understanding of the distribution of **13a** within *P.gingivalis*.

The bacterial samples were incubated for 2 hours with varying concentrations of **13a**, and fixed in 3% glutaraldehyde in PBS. The sample was then dehydrated, embedded in Araldite resin, sectioned and imaged by Dr Chris Hill using Transmission Electron Microscopy (TEM). Only OsO_4 was used as a conventional contrasting agent in all samples. Therefore, any increase in contrast can be attributed to the complex. The resulting TEM images are shown in Figure 17.

The TEM images show a clear increase in contrast between the unstained sample and a sample stained with **13a** at a 10 nM concentration. The contrast becomes more prominent when the concentration of **13a** is increased to 100 nM. At this concentration a high amount of contrast and detail is seen in the cell wall. These images confirm what was suggested by the SIM images, the metal complex is able to stain the bacterial cell wall and concentrate in the cytoplasm. It should be noted that, according to previous work, a much higher concentration of at least 50 μM of **13a** was required to see significant contrast in HeLa cells.[87]

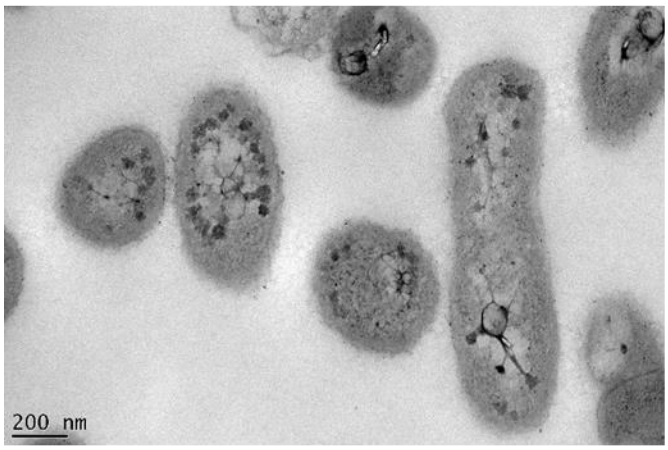

0 nM

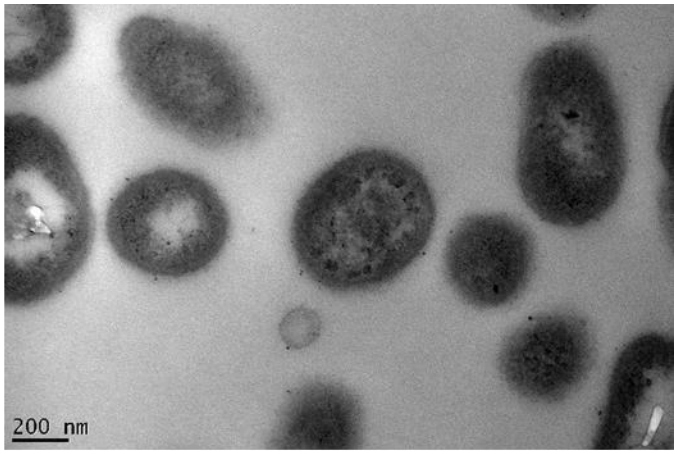

10 nM

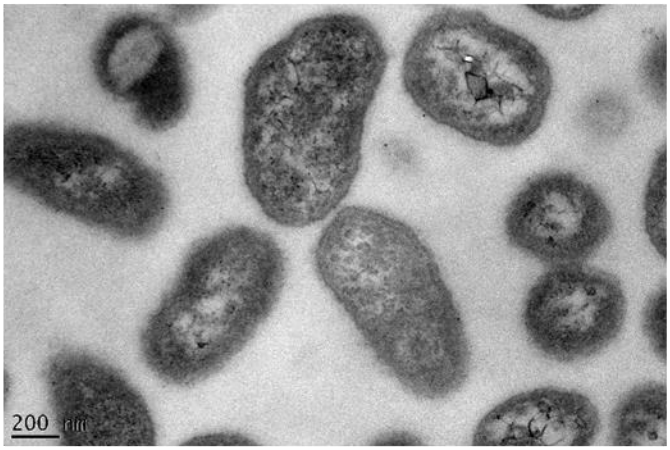

100 nM

Figure 17- TEM images of P.gingivalis with stained with 13a (concentrations shown, 2h). The sample treated with only OsO_4 shows depositions around the membrane. This contrast in the membrane is increased as the concentration of 13a is increased.

3.4 A novel antimicrobial-PDT agent based on 13a

Bacterial toxicities data with **13a** at a relatively low concentration of 5 nM is a promising start. However, it is clear that a higher dosage of **13a** is required for the complete destruction of bacterial colonies. It is important that any potential aPDT completely kill all bacteria to prevent development of resistance. While increasing the concentration of **13a** is a viable option, this would also potentially cause collateral damage to the host cells since the concentration of **13a** required to kill bacteria will overlap with the concentrations that harm cells. It is therefore, necessary for **13a** to target bacteria better. **13a** would also be more clinically accepted if the absorption wavelength has a higher wavelength; 405 nm is not optimal for tissue penetration although it should be noted this problem is not as significant for antimicrobial-PDT as it is in anticancer treatments since lasers can be shone directly on to the periodontal pocket and other infection sites. To answer these questions, the synthesis of a derivative of **13a**, compound **14** was proposed. The structural modifications to **13a** are shown in Figure 18.

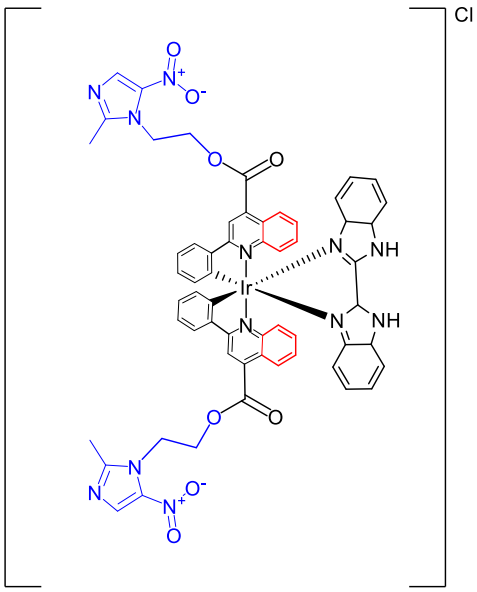

*Figure 18: Structure of new antimicrobial-PDT agent, compound **14**. 13a (black) has been modified with metronidazole (blue) and extra benzene rings (red).*

The two cyclometalating ligands were modified by adding 2-Methyl-5-nitroimidazole-1-ethanol moieties joined by an ester bond. 2-Methyl-5-nitroimidazole-1-ethanol is better known as metronidazole, an antibiotic used for targeting Gram-negative anaerobic bacteria. After entering the cell, the nitro group is reduced by electron donors such as pyruvate:ferredoxin oxidoreductase (PFOR) (Figure 19), thioredoxin reductase (TrxR)or nitroreductase 1 (NTR1) into a radical species. The exact source of the electron donation is dependent on the pathogen.[93,94] These radical species react with the DNA and proteins of bacteria leading to its death. In the presence of oxygen, the radicals are reoxidized into the parent drug. Indeed, it is possible for host cell components to be caught in the crossfire leading to side-effects.

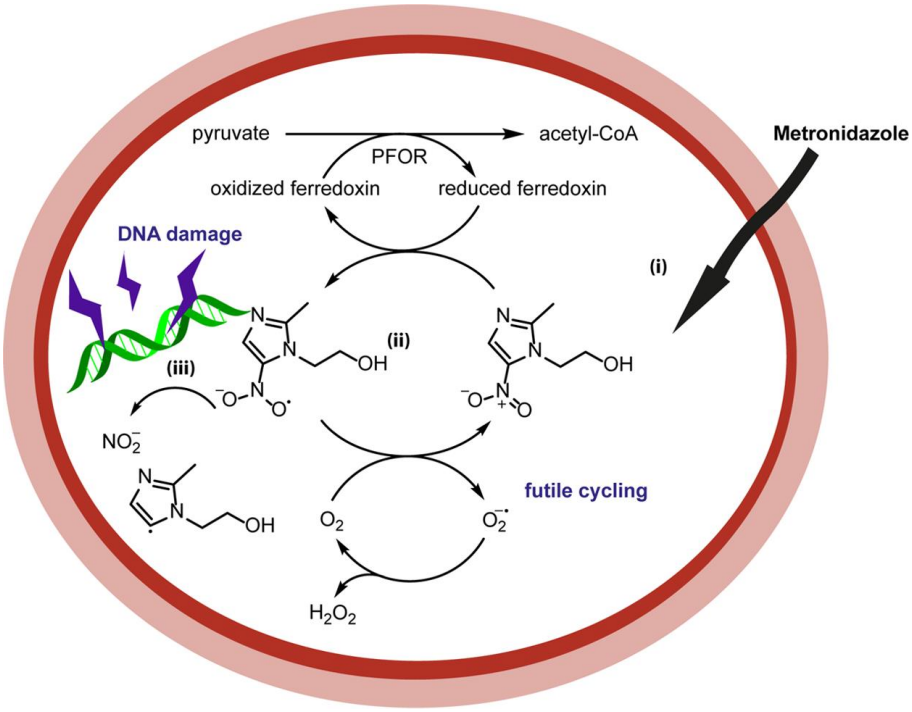

Figure 19: Activation of metronidazole by pyruvate:ferredoxin oxidoreductase (PFOR) (from ref [95])

There are two features of the design of **14**. Firstly, it is hypothesised that the addition of metronidazole on to the iridium complex will enhance the antibacterial characteristics of the

complex by acting as both an antibiotic and an antimicrobial-PDT agents. This will allow for maximal antimicrobial activities with smaller doses.

We note that metronidazole, despite being one of the most used antibacterial agents, does not, by itself, penetrate the bacterial cell wall. Complex **13a**, on the other hand, readily accumulates in both eucaryotic cells, and bacteria. There is therefore additional potential advantage of carrying metronidazole inside the cells using metal complex as a "cargo".

The second design feature is the addition of the two extra benzene rings on to the 2-phenylpyridine. The extension of the aromatic system increases conjugation, lowers the energy of the LUMO, and therefore decreases the energy of the metal-to-ligand charge-transfer transition, thus shifting the absorption band towards the red region, as reported by e.g. Pope *et al* for complexes with a similar modification.[96]

3.5 Initial approach to the Synthesis of 14

3.5.1 Synthesis of the 2-(2-methyl-5-nitro-1H-imidazol-1-yl)ethyl 2-phenylquinoline-4-carboxylate (mdz-pqc)

The cyclometalating ligand, 2-(2-methyl-5-nitro-1H-imidazol-1-yl)ethyl 2-phenylquinoline-4-carboxylate (**mdz-pqc**), was synthesised via a Steglich esterification of 2-phenylquinoline-4-carboxylic acid and 2-methyl-5-nitroimidazole-1-ethanol (metronidazole) using N,N'-dicyclohexylcarbodiimide (**DCC**) as the coupling agent with 4-dimethylaminopyridine (**DMAP**) as the catalyst (Scheme 5). The reaction also yielded dicyclohexylurea (**DCU**). This biproduct is partially soluble in the solvent used (DCM) and most of it can be separated using a simple filtration. The remaining DCU was removed by recrystallising the ligand mdz-pqc in hexane. The reaction was also attempted using 1-ethyl-3-(3-dimethylaminopropyl)carbodiimide (EDC) instead of DCC. However, the reaction is highly water sensitive and has a much lower yield compared to DCC (35% with EDC and 93% with DCC).

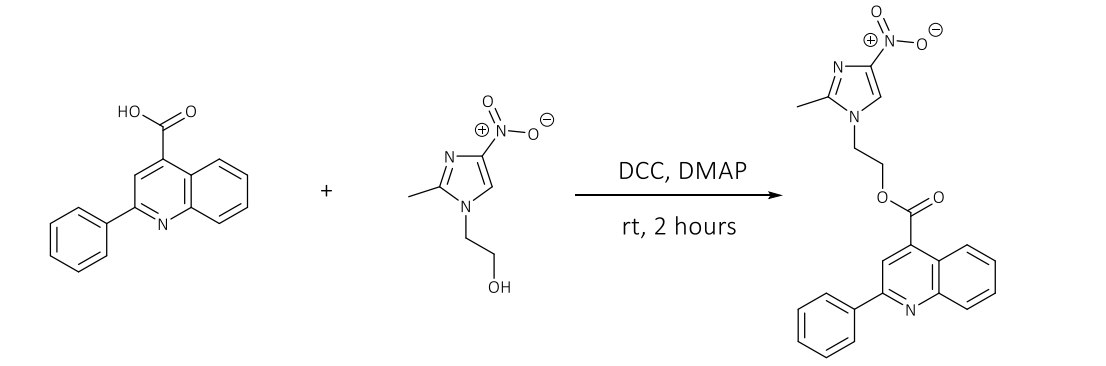

Scheme 5- Synthetic pathway to cyclometalated ligand using a Steglich esterification. Yield 93%.

The product was characterised by ^{1}H NMR spectroscopy (Figure 20)

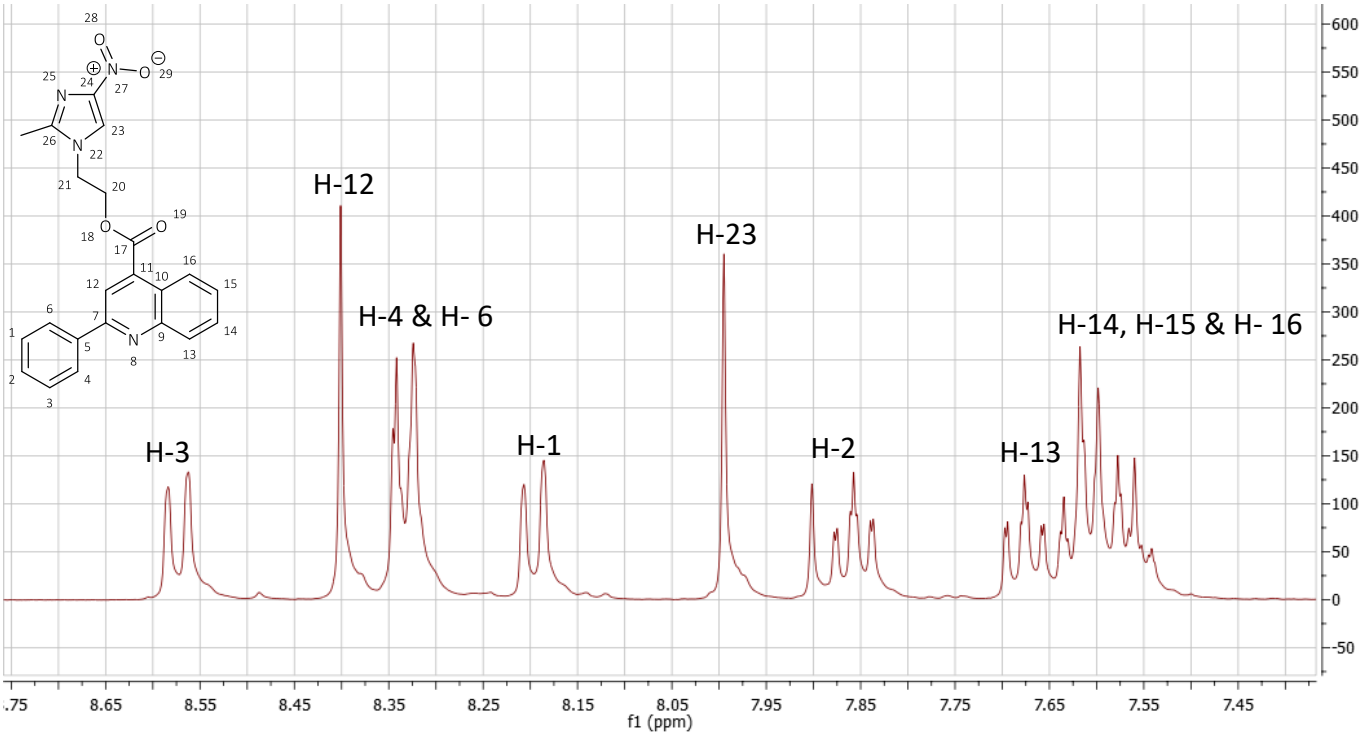

Figure 20- Aromatic region of ^{1}H (400 MHz, 298K, acetone) spectrum of mdz-pqc

Upon esterification into mdz-pqc, the ^{1}H NMR resonances of metronidazole and 2-phenylquinoline-4-carboxylic acid change their position. Generally, the peaks of 2-phenylquinoline-4-carboxylic acid move more up-field upon esterification. The doublet at 8.57 ppm has shifted up-field from 8.82 ppm and the singlet at 8.40 ppm has shifted up-field from 8.60 ppm. This is possibly due to the increased shielding that occurs after the esterification. In this orientation, the COO- group is able to donate electrons into the aromatic ring, which leads to more shielding. The singlet corresponding to the aromatic proton of the metronidazole shows a shift from 7.90 ppm to 7.99 ppm, as the electron density of the corresponding C-atom has decreased upon addition of the electron-withdrawing ester group. These spectra are compared in Figure 21.

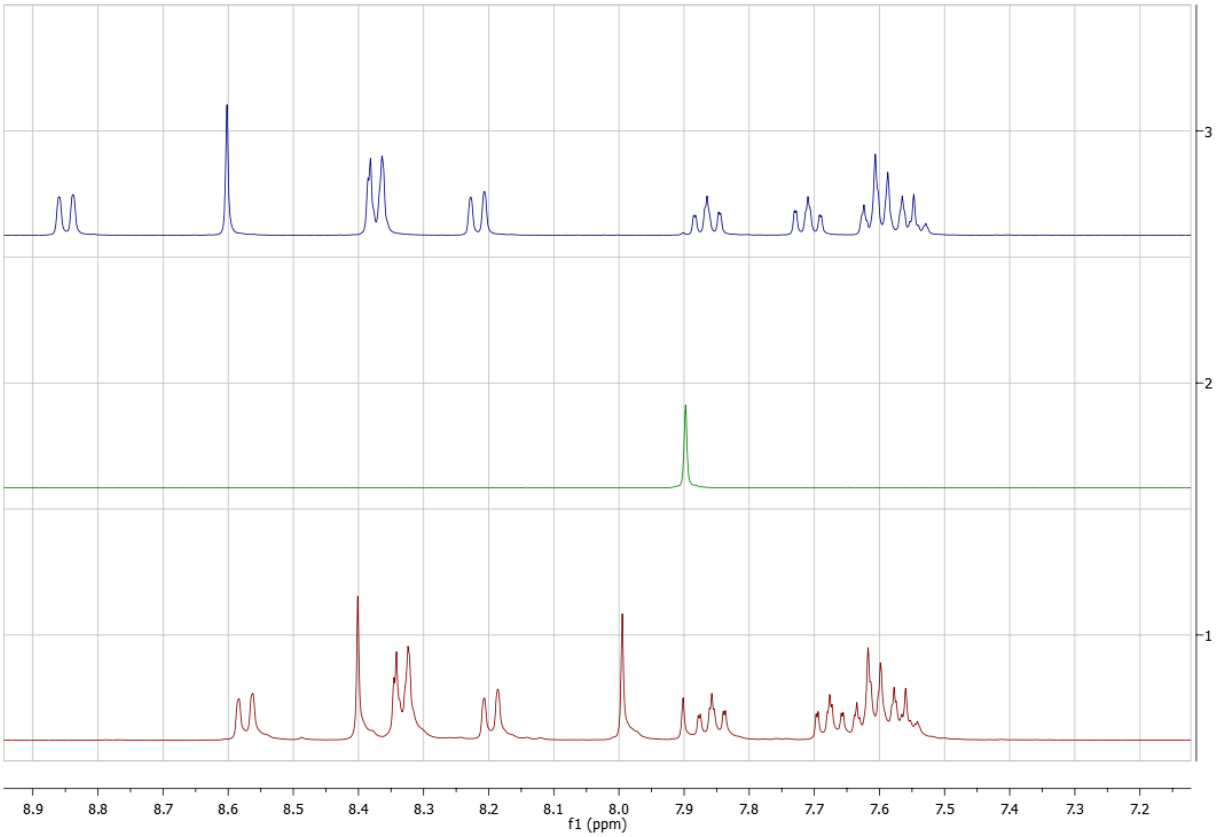

Figure 21- Stacked 1H spectra (400 MHz, 298K, acetone) of 2-phenylquinoline-4-carboxylic acid (blue), metronidazole (green) & mdz-pqc (red)

3.5.2 Synthesis of the [Ir(mdz-pqc)$_2$(μCl)]$_2$

The mdz-pqc ligand was refluxed with $IrCl_3$ in 2-methoxyethanol to form a dimer of bridged by two chlorides, which is the characteristic intermediate in the synthesis of cyclometalated iridium complexes. The resulting dimer, [Ir(mdz-pqc)$_2$(μCl)]$_2$, showed a different ^{1}H NMR spectrum (Figure 22) from the ^{1}H NMR spectrum of mdz-pqc. The loss of a proton at the carbon atom number 4 (H-4) causes the doublet at 8.32 ppm to change into a multiplet. The doublets at 8.20 ppm & 8.60 ppm also split into a doublet of doublets and a multiplet, respectively. Most importantly, the doublet at 8.34 ppm which corresponds to H-4 and H-6 changes its integration

from 2 to 1, confirming that a proton has been lost (In the free ligand this peak integrates to 2 protons). The changes to the ^{1}H NMR are shown in Figure 23. The experimentally obtained m/z value is half of the expected value. This was thought to be cleaving of the sensitive chloride bridge by the solvent (dichloromethane in this instance). The isotopic pattern confirms the presence of the half-dimer.

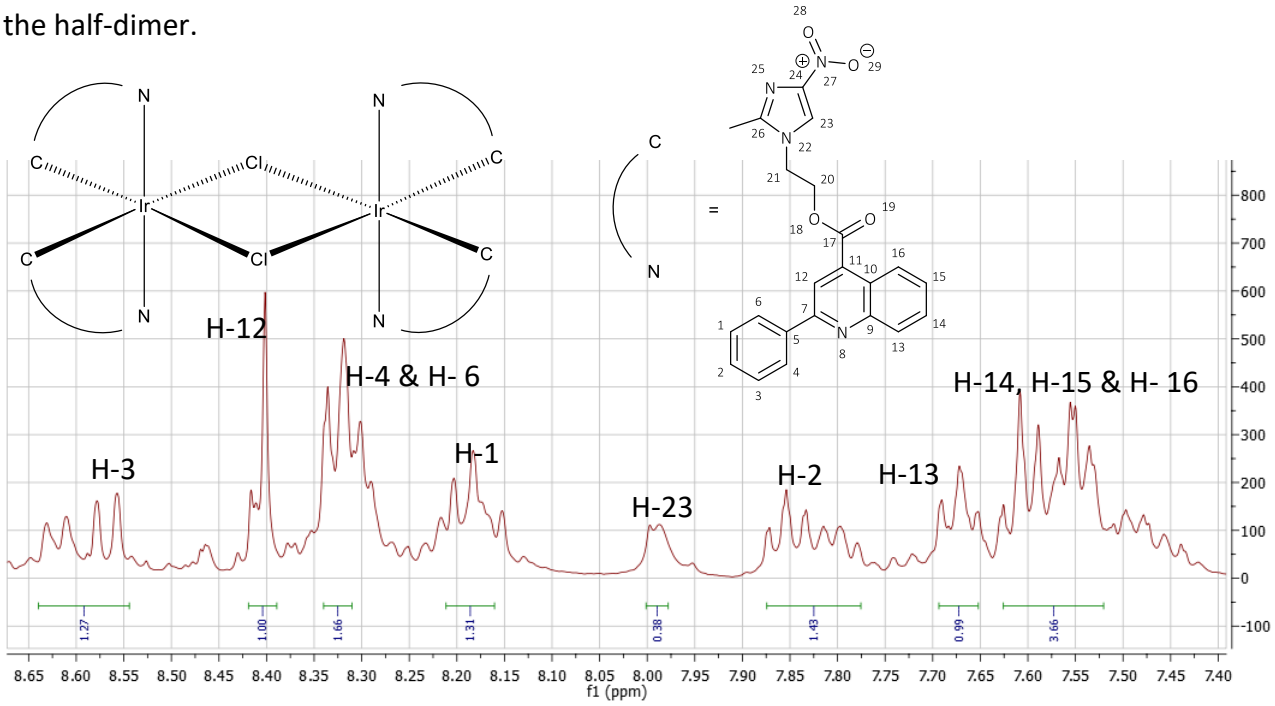

Figure 22- Aromatic region of ^{1}H spectrum (400 MHz, 298K, acetone) of [Ir(mdz-pqc)$_2$(μCl)]$_2$

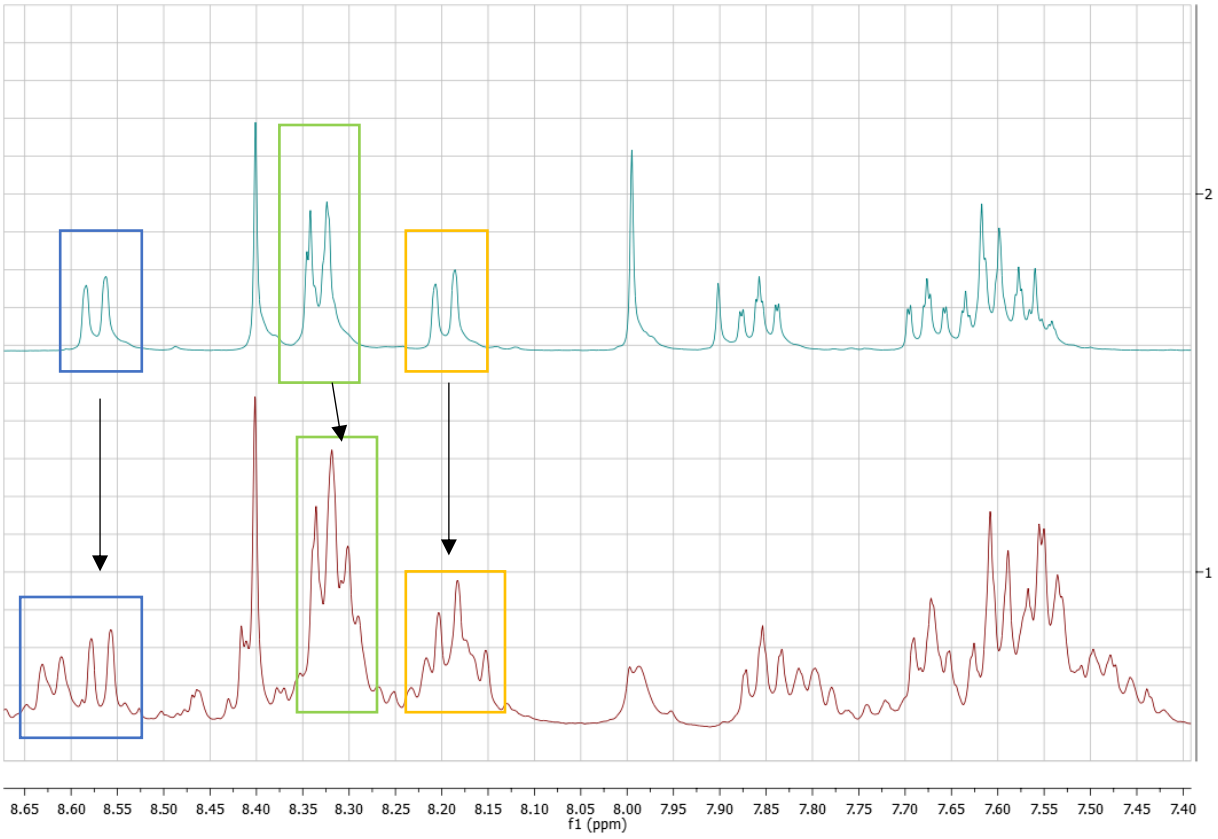

Figure 23- Stacked ^{1}H NMR spectra (400 MHz, 298K, acetone) of aromatic regions of mdz-pqc (cyan) & $[Ir(mdz\text{-}pqc)_2(\mu Cl)]_2$ (red)

3.5.3 Synthesis of bis-benzimidazole.

The ancillary ligand of this complex is bisbenzimidazole. The synthesis of this ligand had been attempted before the start of this project with the use of prior literature.[97] This synthesis used a dehydration reaction between *o*-phenyldiamine and oxalic acid, utilizing poly-phosphoric acid as the catalyst. However, this reaction had poor success rate and yields. This could be due to the accumulation of water by poly-phosphoric acid under reflux conditions. The purification involved Soxhlet extraction, which contributed to further diminished yields. A new method was attempted by replacing oxalic acid with dithiooxamide. This reaction too had poor success rates and

returned the starting products for majority of the time. A better method using microwave heating resulted in excellent yields and reproducibility. This is discussed further in the section below.

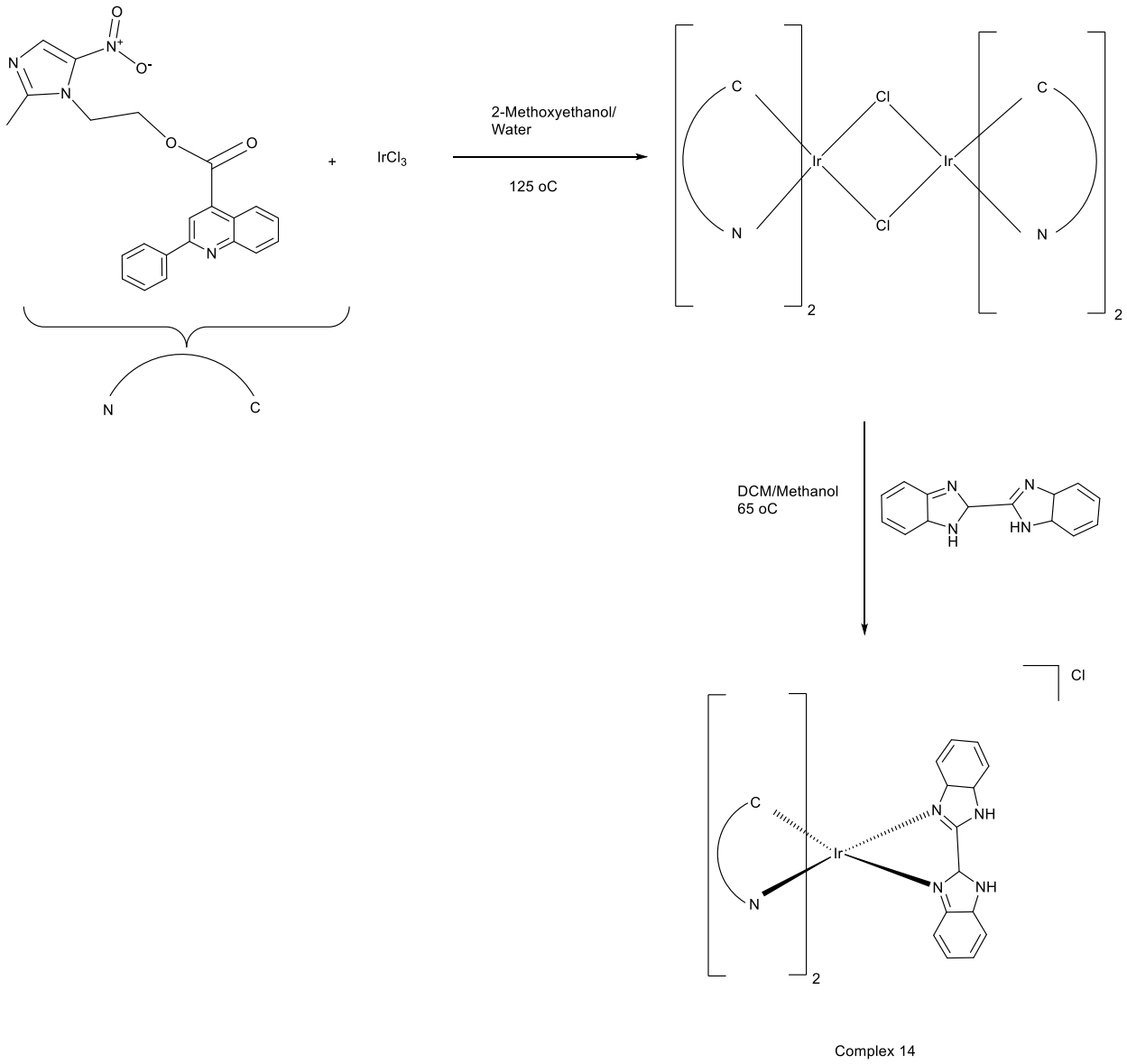

Scheme 6- Reaction pathway to complex 14

3.5.4 Synthesis of 14.

To obtain the final complex, $[Ir(mdz\text{-}pqc)_2(\mu Cl)]_2$ was refluxed with 2.1 equivalents of bisbenzimidazole in MeOH:DCM (1:1). The bisbenzimidazole breaks the di-chloride bridge and

coordinates to the iridium centre. The solvent mixture was evaporated resulting light green precipitate was dissolved minimum amount of the solvent mixture (5 mL) and precipitated with acetonitrile. The resulting ^{1}H NMR spectrum showed significant amount of impurities, mostly from unreacted starting material. The crude precipitate was dissolved in a minimum amount of acetone, and the resulting acetone solution was added dropwise to a concentrated brine solution to obtain a light-yellow precipitate. This method removed most of the impurities but the ^{1}H NMR spectrum still showed some signals from the unreacted staring materials. Further purification was attempted using column chromatography using various permutations of eluents on silica gel and neutral alumina. Due to the high polarity of both the reactants and the final complex, column chromatography continued to be unsuccessful as coelution became a recurring problem. Separation was ultimately achieved using preparative HPLC using 40% THF in water. The aromatic region of the ^{1}H NMR spectrum of the purified **14** is shown in Figure 24.

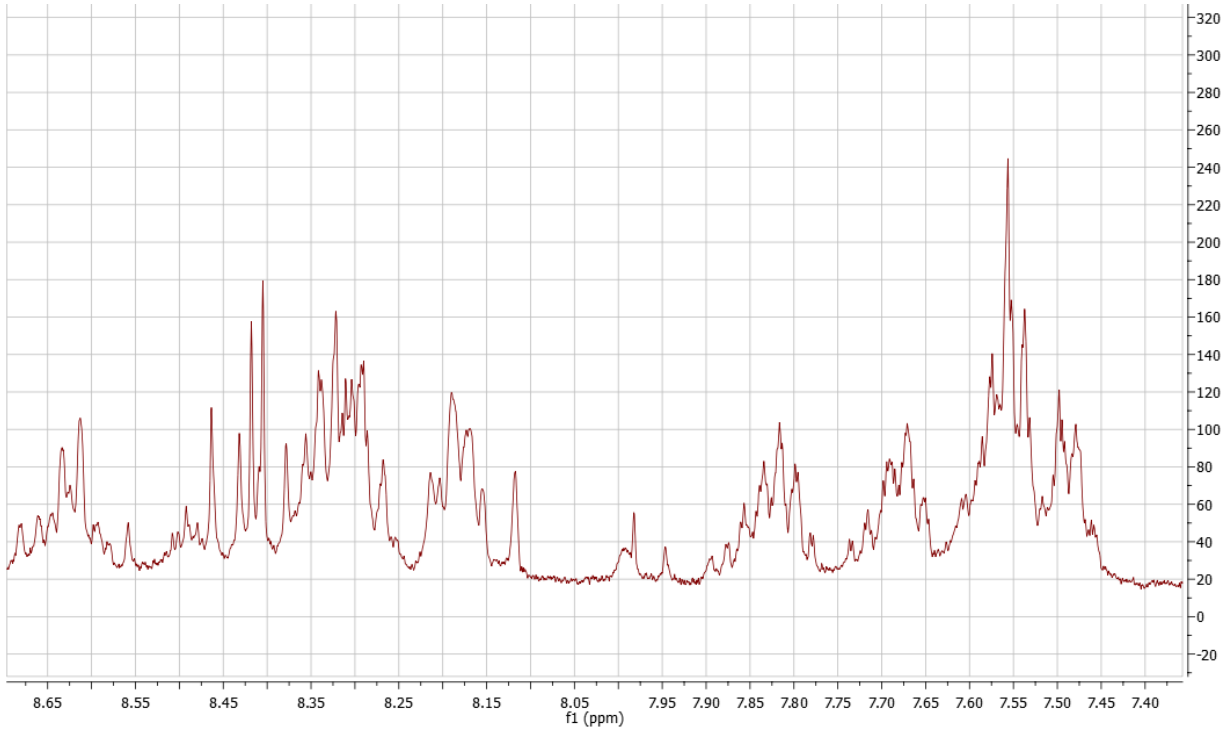

Figure 24-Aromatic region of ^{1}H spectrum (400 MHz, 298K, acetone) of $[Ir(mdz\text{-}pqc)_2(bbzH_2)]Cl$

The ^{1}H NMR spectrum of complex **14** shows complex splitting patterns and peak broadenings. The metronidazole moiety of the complex can be classed as an azole. Azoles are capable of undergoing complicated mechanisms known as annular tautomerism. Imidazoles in particular are known to exhibit prototropic annular tautomerism and often exist as a mixture of tautomers, where one tautomer will be favoured over another depending on conditions such temperature, solvent, pH and substituents.[98,99]

The exchange of the nitroimidazole's aromatic proton with the nitro group explains the reason for broadening of the corresponding resonance at 7.98 ppm. Despite the peak splitting the integration of the multiplets is equal to the expected values (except for the imidazole proton's

peak mentioned above which is integrating to a lower than predicted value), which indicates the formation of the desired product **14**.

The changing of positions between the imidazole aromatic proton and the nitro-group breaks the symmetry of the molecule as the NMR detect complexes with 4-nitro or 5-nitroimidazoles. This results in the splitting of peaks into multiplets. It has been found that although the 5-nitroimdazole is more stable, the 4-nitro tautomer dominates due to its higher dipole moment, which increases solubility.[100,101] The tautomers are shown in Figure 25. It is interesting to note that some studies suggest that addition of electron-withdrawing groups favour the 3-nitroimidazole or shift the equilibrium towards 5-nitroimidazole.[102] The coordination of the ligand mdz-pqc to Iridium will cause shift of electron density from the ligand to Ir atom, and could explain why larger splitting of ^{1}H-NMR resonances is observed in the ^{1}H-NMR spectrum of complex **14**, but not in the ^{1}H-NMR spectrum of its Ir-dimer precursor.

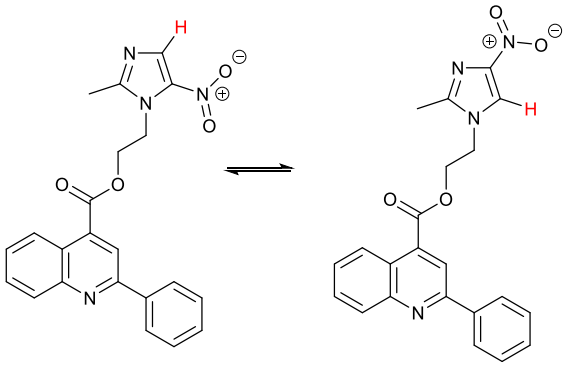

Figure 25- The tautomers of mdz-pqc

In order to investigate if the tautomerism was the reason for the complex NMR pattern observed, ^{1}H NMR spectrum was recorded at 223 K (Figure 26). It was thought that the lower temperature

would slow down the exchange of the proton and yield a clearer spectrum. Indeed, lowering the temperature reduced the splitting observed above. The singlet from the aromatic proton of the nitroimidazole at 7.98 ppm is clear, sharp and shows no broadening. However, there are splitting occurring, as evident by the overlapping doublets at 7.90 ppm. This is consistent with studies of imidazoles, which state it is not possible to detect individual tautomers even at lower temperatures.[103] Mass spectrometry analysis of the pure mixture confirmed the presence of complex **14** (m/z = 1144). Neither the NMR or the mass spectroscopy can be used to confirm purity of the complex. This was done using analytical HPLC.

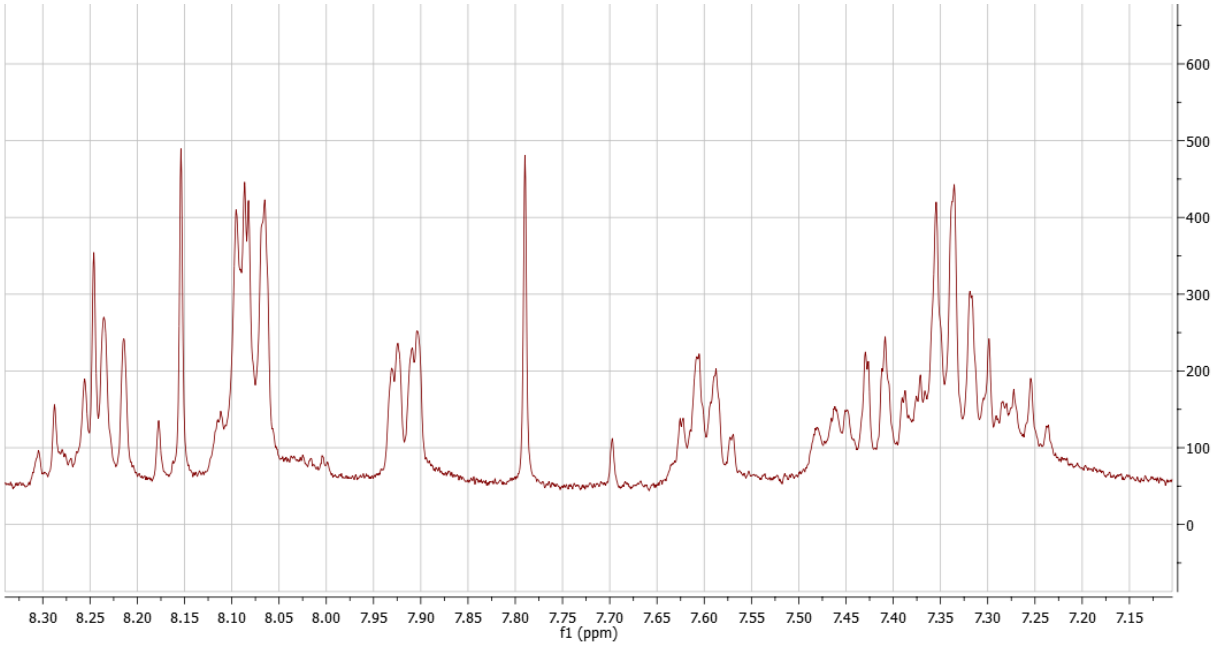

Figure 26- Aromatic region of ^{1}H (400 Hz, 223 K, acetone) spectrum of $[Ir(mdz\text{-}pqc)_2(bbzH_2)]Cl$

3.6 Optimisation of the Synthetic procedure for 14

The reactions used to synthesise the target complex **14** described in the previous section resulted in poor yields (15%). In the case of bisbenzimidazole synthesis, the originally used reaction gave poor yields and inconsistent results (10%). To solve both of these problems, the reactions were optimised my using microwave-assisted synthesis. Microwave-assisted synthesis occurs due to dielectric heating. Dielectric heating is the interaction of the electric field of the microwave radiation (wavelength 1 mm – 1 m) with the molecules. One such interaction is dipolar polarisation. When irradiated with microwaves, the dipole moment of the molecules will rotate to align themselves with the electric field. However, the microwave frequency is not high enough for the perfect alignment of the dipole. This causes a phase difference between orientation of the dipole moment and the electric field, resulting in dielectric heating due to the energy loss from the dipole moment due to friction and collisions between molecules. Alternatively, if ions are present in solution, these ions will follow the electric field and cause heating through collisions, which leads to kinetic energy being converted to heat. Heating caused by ionic conduction is much stronger than dipolar polarisation. However, despite the mechanism utilised by the system, microwave heating is far more efficient than conventional heating. In conventional heating, the heat needs to passed through the walls of the vessel. This is in contrast to microwave heating where the microwaves reach the reaction mixture directly. The result is a more uniform and efficient distribution of heat (Figure 27).

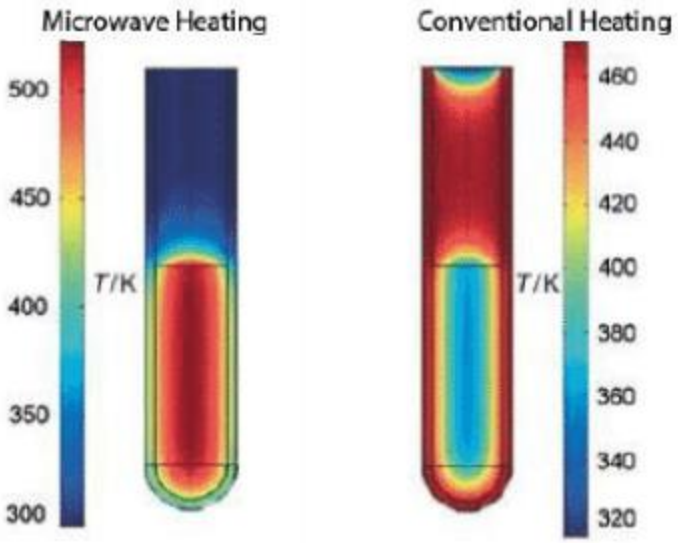

Figure 27- The distribution of heat from microwave heating vs conventional heating (from ref [104])

In commercial microwave reactors (both domestic and industrial) the frequency is set at 2.45 GHz.[105] This means that only temperature can be used to control the dielectric constant as dielectric constant decreases with increasing temperatures. Therefore, the most effective solvents to be used in microwave-assisted synthesis are solvents with high dielectric constants (e.g. ethylene glycol, water, DMSO, DMF).

The synthesis of ancillary ligand, mdz-pqc, using microwaves was no attempted as the initial reaction was reproducible at room temperatures and produced high yields of the ligand. In contrast, the synthesis of the Ir-dimer, $[Ir(mdz\text{-}pqc)_2(\mu Cl)]_2$, required refluxing for 48 hours and resulted in only 54% yield. The reaction was then attempted using microwave heating. The reaction temperature remained the same at 120 °C. The solvent mixture, 2-methoxyethanol and water (3:1) was also kept the same as both 2-methoxyethanol and water are highly polar solvents and meet the needs for microwave heating. The reaction mixture was heated in 10 mL microwave tube for 30 min (max 20 Watt). The workup remained the same. The reaction yielded 79% of

product. In addition, the crude mixture showed greater purity than the crude mixture from the synthesis performed using conventional heating, as shown by the ^{1}H NMR spectra in Figure 28.

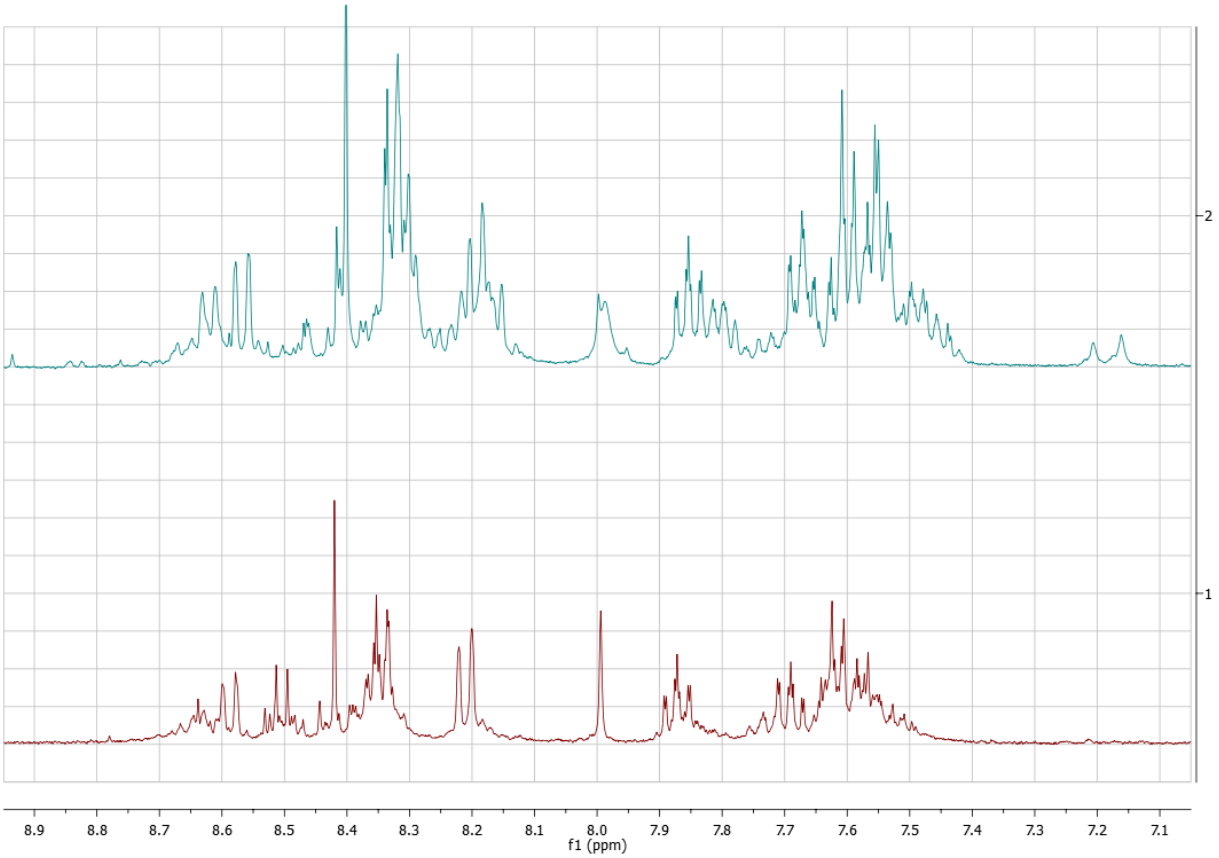

Figure 28- ^{1}H NMR spectra (400 MHz, 298K, acetone) of crude reaction mixtures of $[Ir(mdz\text{-}pqc)_2(\mu Cl)]_2$ after reflux (top) and microwave heating (bottom) approaches

To obtain the equatorial ligand, bisbenzimidazole, o-phenylenediamine and oxalic acid were reacted in a 10 mL microwave tube at 160 °C for 30 minutes. Polyphosphoric acid was used as the catalyst and ethylene glycol was used as the solvent. This reaction proved to be efficient and high yielding (77% yield). Furthermore, the work up was a simple precipitation in water. The ^{1}H-NMR spectrum of the product, bisbenzimidazole, is shown in .

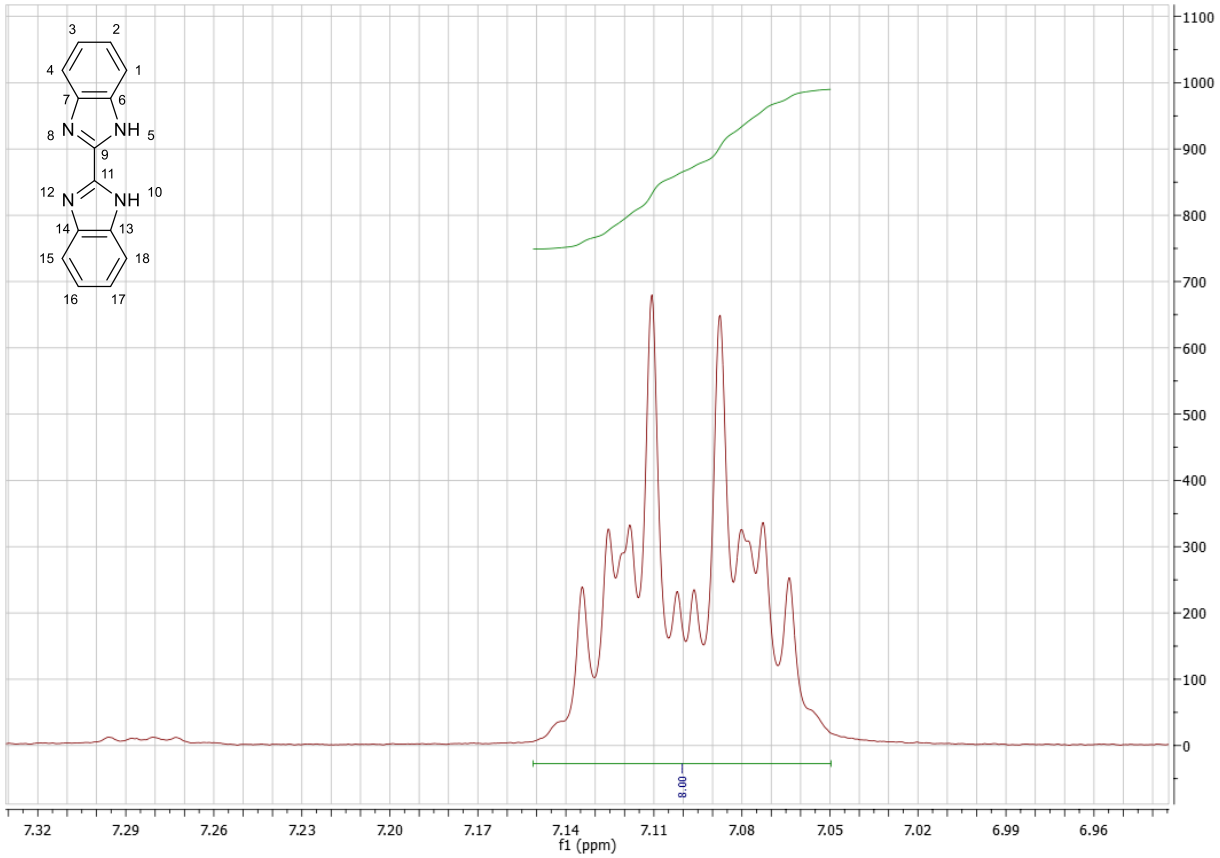

Figure 29- Aromatic region of 1H NMR spectrum (400 MHz, 298K, DMSO) of bisbenzimidazole

The ^{1}H NMR obtained for bisbenzimidazole is consistent with literature and shows a single multiplet at 7.01 ppm.[106]

This success could not be replicated for the synthesis of complex **14**. $[Ir(mdz\text{-}pqc)_2(\mu Cl)]_2$ and bisbenzimidazole was dissolved in a variety of solvents and irradiated with microwaves for various times at different temperatures (see table below) . The optimum solvent system for refluxing this reaction is DCM:MeOH (1:1). However, this system is not ideal for microwave reactions. Due to the low dipole moment of DCM and MeOH, the actual working temperature of the solvent is below 65 °C. Therefore, while the reaction produced some product, the yields were

lower than when heating to refulx. Changing the solvent to the more polar ethylene glycol resulted in the decomposition of the reactants and/or product. This is evident in the ^{1}H NMR spectra of the crude reaction mixtures (Figure 30). A singlet expected at ca 8.00 ppm and a doublet of doublets expected ca 6.00 ppm are completely missing. These peaks correspond to the protons of metronidazole. The spectrum indicates that the dimer and ligand have decomposed. This could be due to the high working temperature of 160 °C

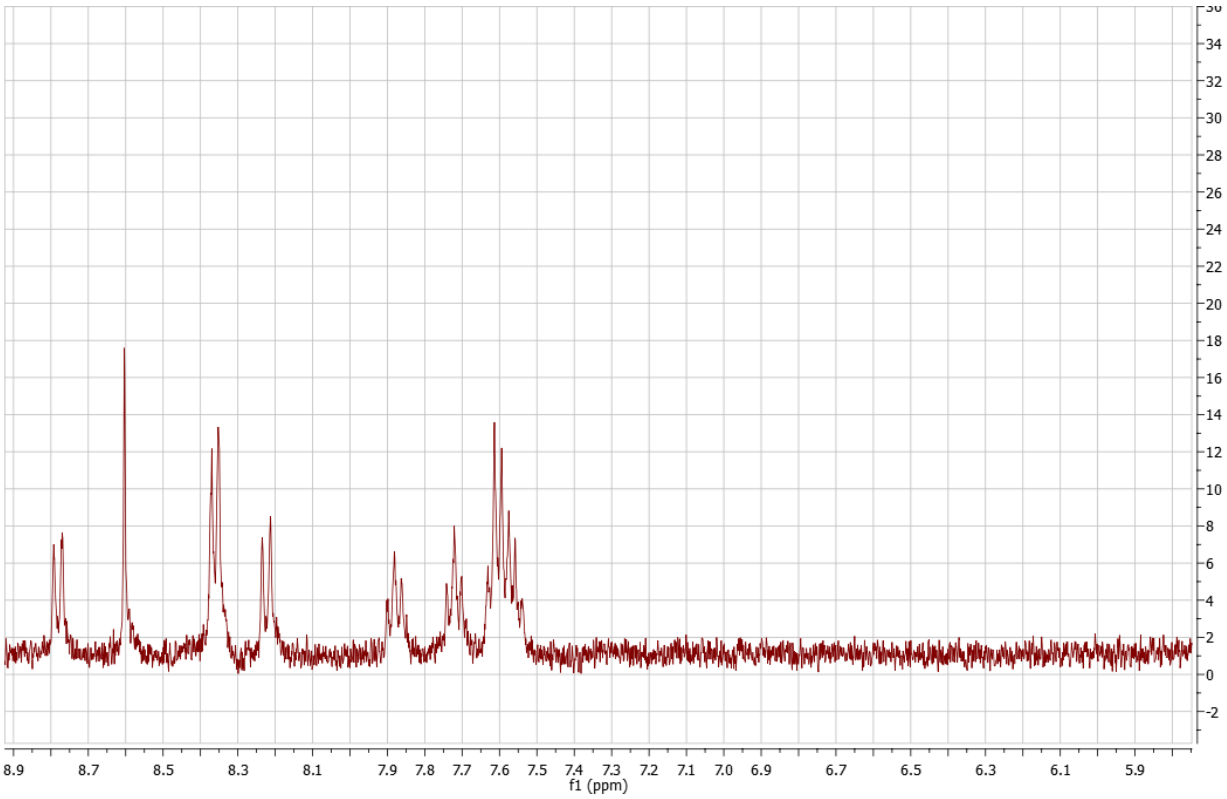

Figure 30- ^{1}H NMR spectrum (400 MHz, 298K, acetone) of a crude reaction mixture after a microwave assisted reaction between $[Ir(mdz\text{-}pqc)_2(\mu Cl)]_2$ and bisbenzimidazole.

The best results were achieved with 2-methoxyethanol as the solvent, at 70 °C, and 30 minutes reaction time. Higher temperatures seem to decompose the product as was the case with ethylene glycol. Reducing the temperature to negate the effects of high temperature reaction resulted in the recovery of the product. Heating the reaction at 70 °C for 30 minutes in 2-methoxyethanol resulted in 50% yield. Although relatively low, it is a significant improvement from the yield of the standard reflux reaction, which was 15%.

Temperature/°C	**Solvent**	**Time**	**% crude yield**	**comment**
65	DCM:MeoH (1:1)	30 min	15	
120	2-Methoxyethanol	30 min	0	-
120	2-Methoxyethanol	1 h	0	Recovered decomposed dimer
120	2-Methoxyethanol	10 min	0	Recovered reactants
70	2-Methoxyethanol	30 min	50	
160	Ethylene glycol	30 min	0	Recovered decomposed product
70	2-Methoxyethanol	1 h	50	

Table 1 - Various reaction conditions used for the microwave assisted reaction between $[Ir(mdz\text{-}pqc)_2(\mu Cl)]_2$ and bisbenzimidazole.

3.7 Synthesis of a control complex

In order to verify the hypothesis behind complex **14**, another control complex was needed, complex **15**. This complex should have the backbone of **14** except for the metronidazole moiety. If complex **14** causes more bacterial death than complex **15** it would indicate that the metronidazole, in particular the nitro group, is involved in the mechanism.

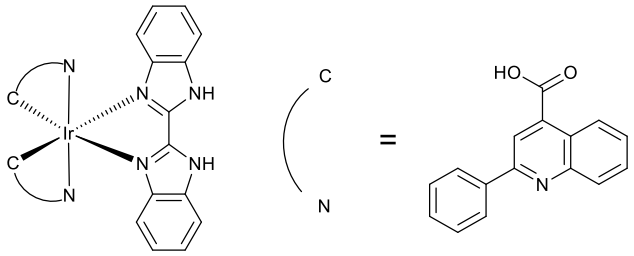

15

The synthetic route used was similar to the one used for the initial preparation of complex **14**. 2-phenylquinoline-4-carboxylic acid was reacted directly with $IrCl_3$ without any modifications to obtain the iridium dimer. The reaction was resulted in the dimer, $[Ir(pqc)_2(\mu Cl)]_2$, as a dark purple precipitate in poor yields (10 %). This precipitate was extremely insoluble and was only partially soluble even in DMSO. Due to this, the clarity of the ^1H NMR (Figure 31) was poor and accurate integration was not possible. However, the spectrum showed significant shifts in peaks arising from the proton on the 13th carbon atom, moving downfield from 7.85 ppm to 7.98 ppm. There splitting pattern for the peak at 8.60 ppm corresponding to H-3 changes from a singlet to a multiplet. These changes are consistent with the changes from the dimer of complex **14**.

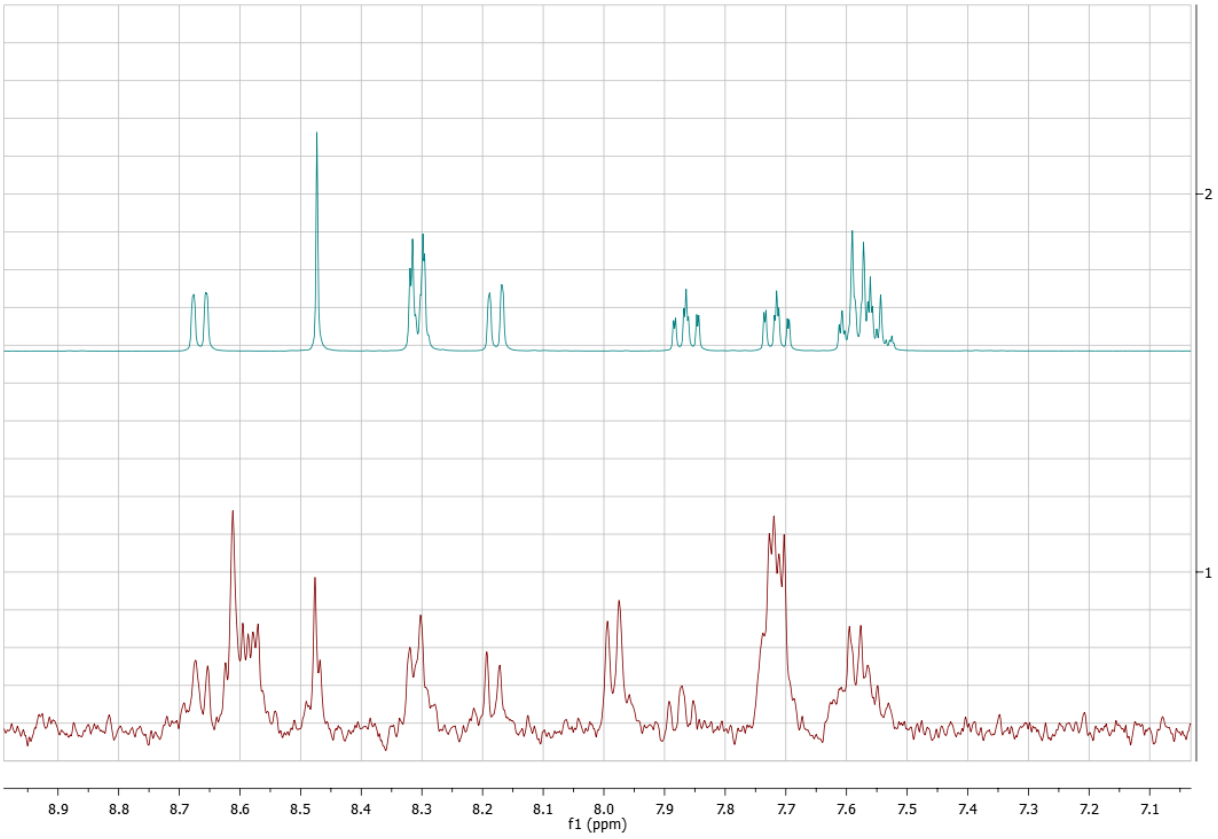

Figure 31-Stacked ^{1}H NMR spectra (400 MHz, 298K, acetone) of aromatic regions of pqc (cyan) & $[Ir(pqc)_2(\mu Cl)]_2$ (red)

$[Ir(pqc)_2(\mu Cl)]_2$ was then heated to reflux temperature with bisbenzimidazole to obtain complex **15**. This reaction was inefficient and yielded only 10% of the product.

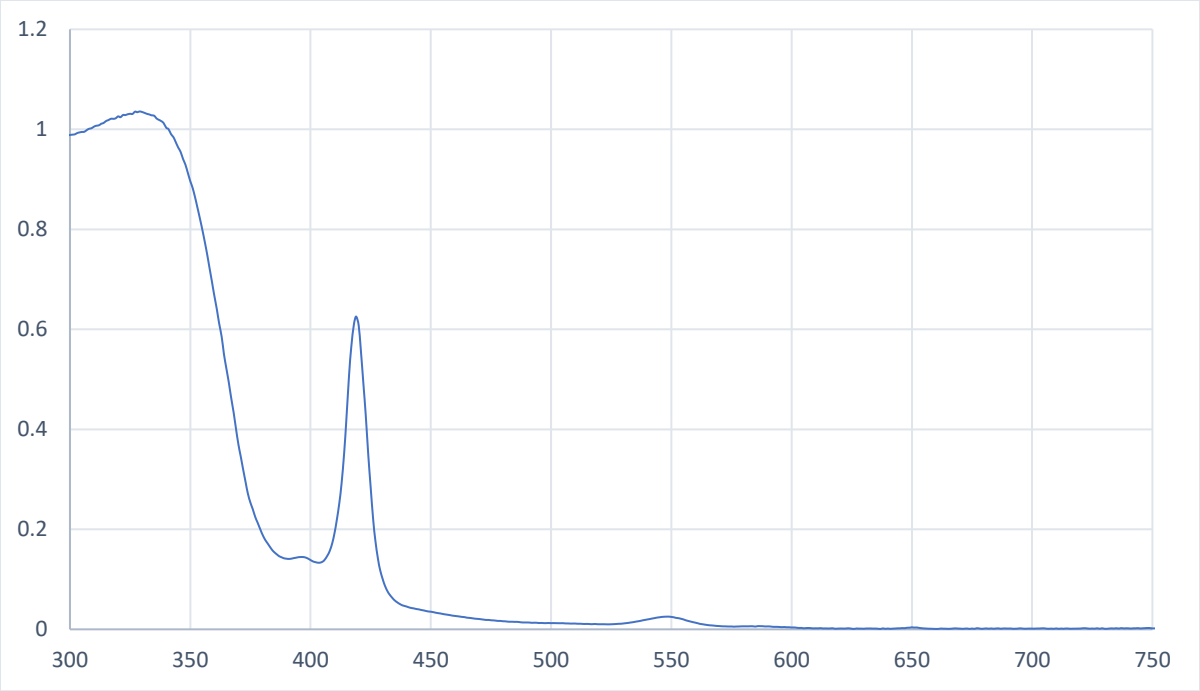

Figure 32- Absorbance spectrum of Complex 14, in CH_2Cl_2

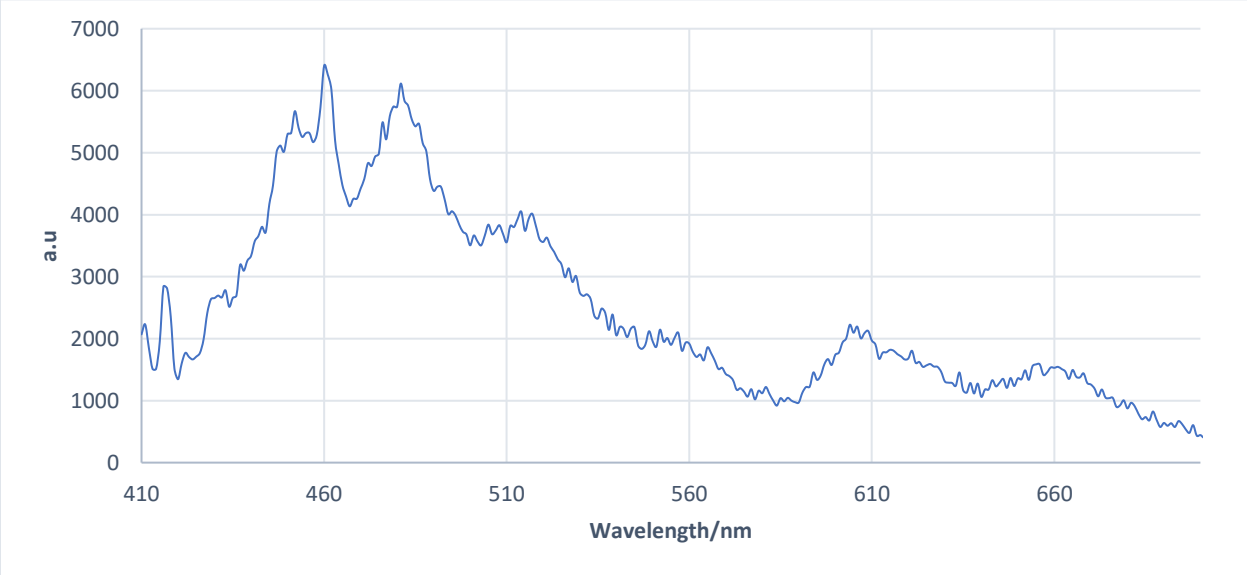

Figure 33- Emission spectrum of an aerated Complex 14at 405 nm excitation, in CH_2Cl_2

3.9 Conclusion

A previously reported Ir(III) complex (**13a**) used in anticancer PDT treatments was tested on *P.gingivalis*, a pathogen responsible for severe periodontal disease. Initial results indicate that **13a** is able to successfully kill *P.gingivalis* at a relatively low concentration of 5 nM, which is a concentration that is not harmful for human cells. The effectiveness of **13a** decreased with an increase in bacterial concentration, indicating the need for better targeting towards bacteria. A new Ir(III) complex based on **13a** was proposed. This new compound, complex **14**, possesses an additional antibiotic moiety, on the ancillary ligand, leading to a dual antibiotic/PDT effects. The new ancillary ligand was synthesised using an esterification reaction. It was then reacted with $IrCl_3$ to form a di-Ir dimer bridged by chloro groups. The dimer was cleaved with bisbenzimidazole to obtain the final complex. The final complex shows evidence of tautomerism as a result of exchanging an aromatic hydrogen and the nitro group of the antibiotic moiety. The synthesis was optimised using microwave assisted synthesis. Overall, microwave assisted synthesis resulted in quicker reactions times and produced higher yields compared to refluxing.

Chapter 4

Antimicrobial effects of complex 14 on Porphyromonas gingivalis

4.1 Antimicrobial effects on planktonic *P.gingivalis*

Complex **14** was tested on *P.gingivalis* (W50). A concentration of 5 nM was used as this was thought to be non-toxic to host cells (please see cell toxicity studies below). Complex **14** was compared against its closely related complex **15** and pure metronidazole. A bacterial concentration of 0.5 OD_{600} was used. The samples were either irradiated with a 405 nm laser diode at 20 $mWcm^{-2}$ for 3 min or kept in the dark. Two bacterial solutions were treated with PBS. One of these was treated with light to investigate if there is any damage done by the laser alone. The second PBS sample was the negative control. The results are shown in Figure 34.

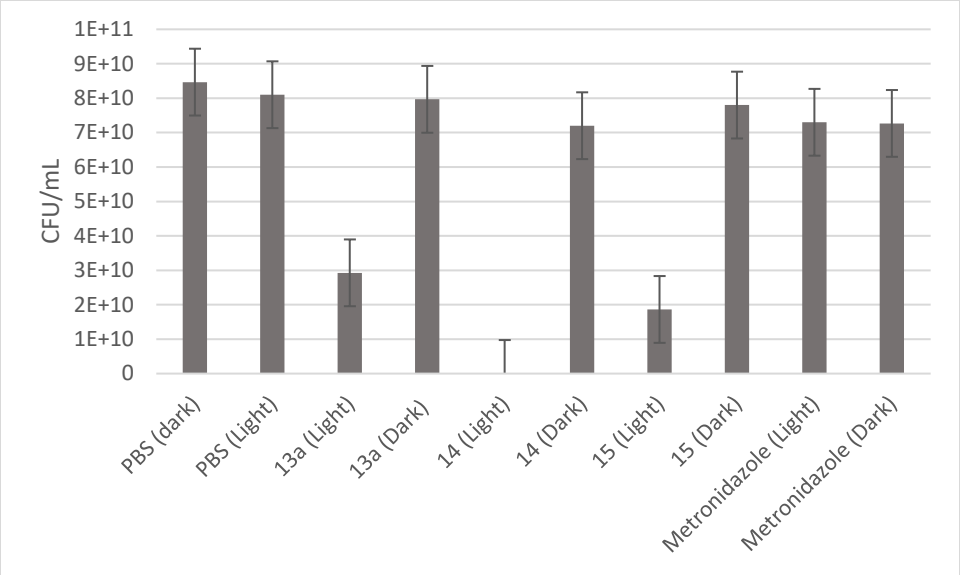

Figure 34- Survival of P.gingivalis (0.5 OD_{600}) after incubation with complexes 13a, 14 and 15 (5 nM, 2 h) & metronidazole (10 nM, 2 h) after treatment with light (405 nm 3 min, 20 mW cm-2) or kept in the dark (n = 4).

The bacterial sample treated with complex **14** (+ light) showed a significant reduction in colonies. When compared to sample treated with PBS and kept in the dark, the colonies treated with complex **14** was reduced by 99.9%, which equates to $3\log_{10}$ reduction. Complex **14** also shows much better aPDT activity than its anticancer counterpart **13a**. Interestingly, pure metronidazole had little antibacterial activity (+/- light) at the concentration used. The very slight reduction is equal to that in the presence of complex **14** (- light). This suggests that the enhanced antimicrobial capabilities is due to a synergistic effect of metronidazole and the cyclometalated iridium center. Further PDT experiments show the minimum inhibitory concentration (IC_{50}) to be ≤ 5 nM as shown in Figure 35. The IC_{50} of most commonly used antibiotics to treat periodontal disease is > 70 nM.

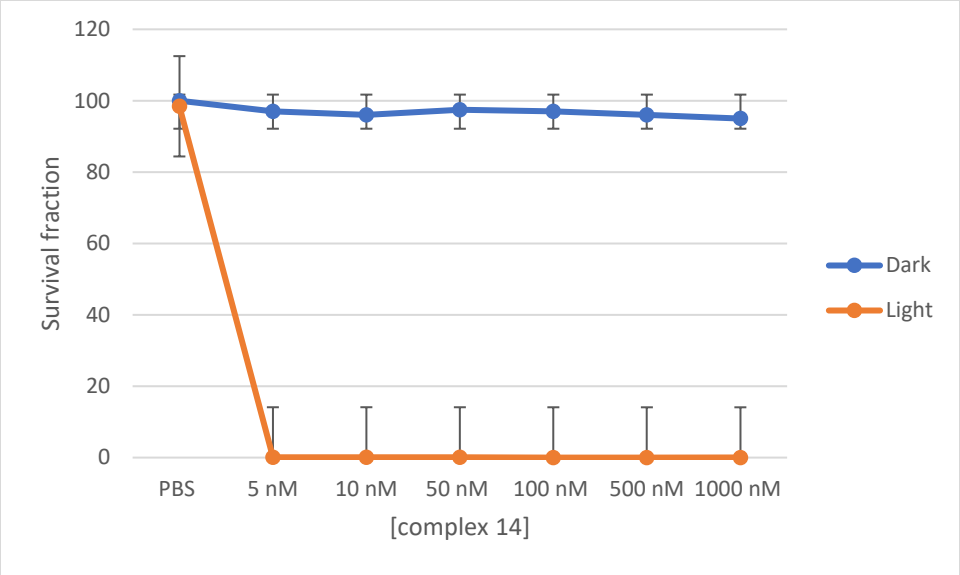

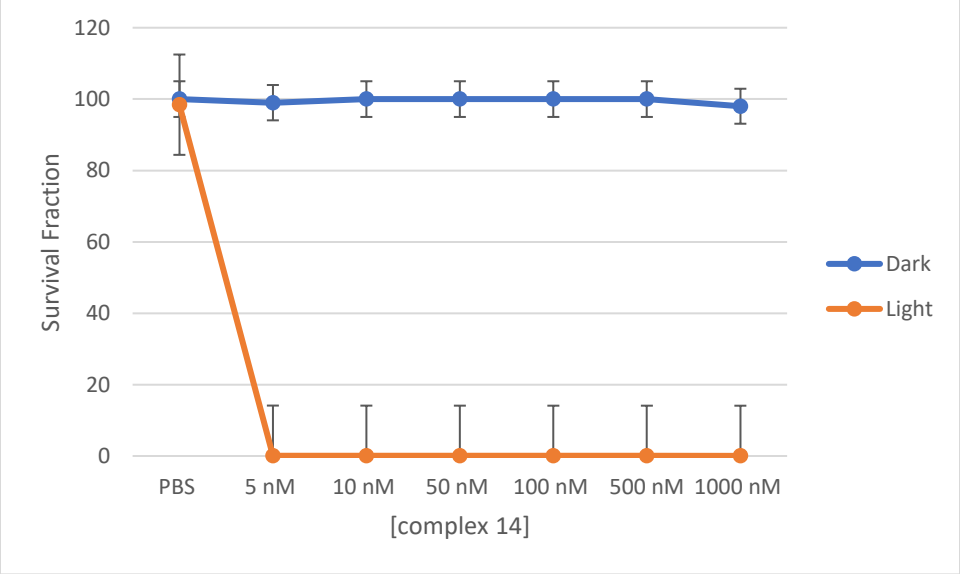

Figure 35-PDT activity of complex 14 at various concentrations P.gingivalis (W50) (top) & P.gingivalis (NCTC 11834) bottom treated with light (405 nm 3 min, 20 mW cm^{-2}) or kept in the dark (n=3)

The viability of both strains was unaffected by the presence of complex **14** in the dark. This is an advantage as more control can be gained over the drug action. Furthermore, this will reduce the likelihood of bacteria developing resistance in the future.

4.2 Comparison with Periowave system

Periowave™ treatment is a PDT treatment currently in the market for treatment of periodontal disease. It is a formulation has methylene blue as its active ingredient, which is administered to a patient and irradiated locally with light of the wavelength of ≈ 620 nm. Two samples of undiluted treatment solution were incubated with NCTC 11834 for 10 minutes. One sample was kept in the dark while the other was irradiated with 625 nm light. The results are shown in Figure 36.

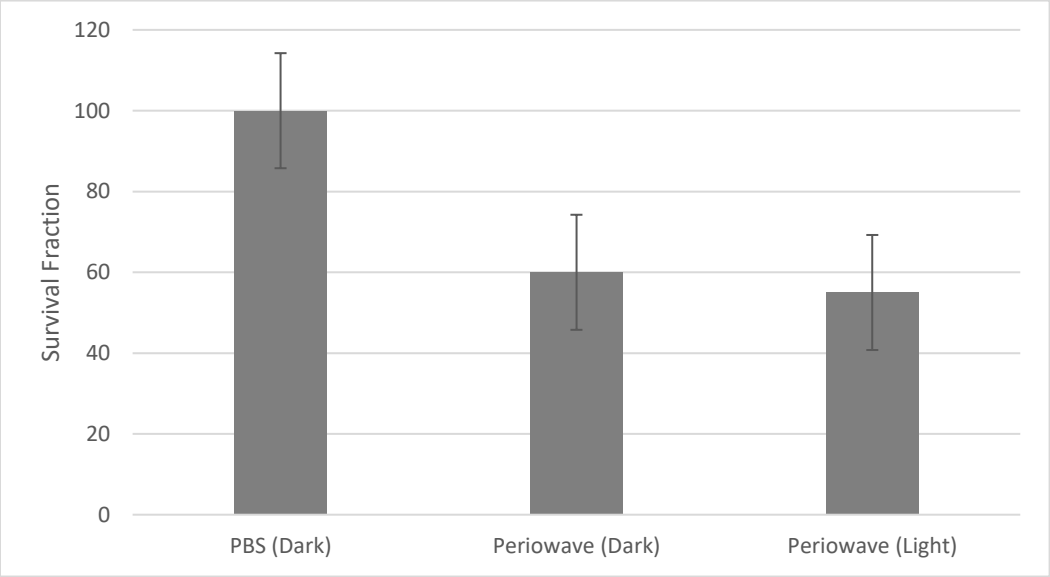

Figure 36- Survival of P.gingivalis (NCTC 11834) with Periowave treatment. Bacterial suspensions were incubated with the Periowave treatment (undiluted, 10 min) followed by treatment with light (625 nm, 33 mW cm^{-2}, 1 min) or kept in the dark. (n=8) This treatment was done following a similar protocol prescribed by Periowave.

When irradiated with light the Periowave treatment reduces bacterial count by approximately 45%, which is significantly less than the 99.9% reduction caused by complex **14**.

4.3 Cell toxicity

Cellular uptake of complex **14** was confirmed by confocal microscopy (Figure 37) and shows cytoplasmic localization, similar to previously reported cyclometalated iridium complexes.[87]

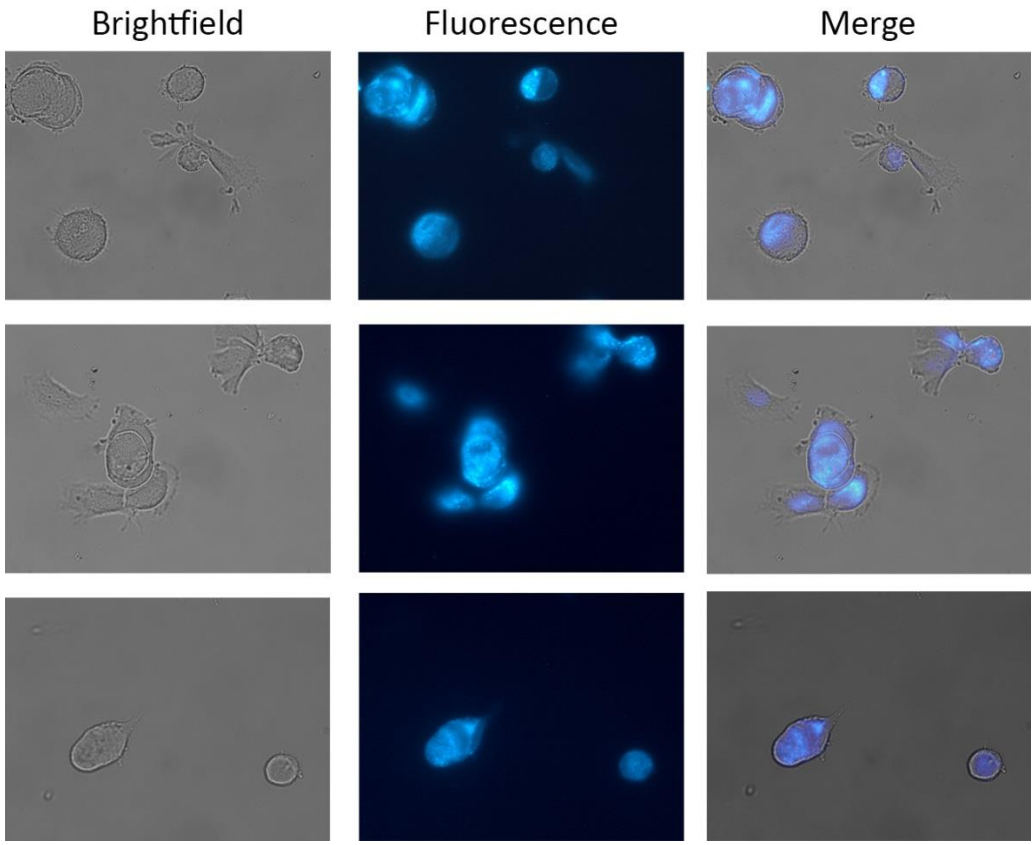

Figure 37- Confocal images of H357 cells treated with 14 (10 μM) (images taken by Dr Callum Jones)

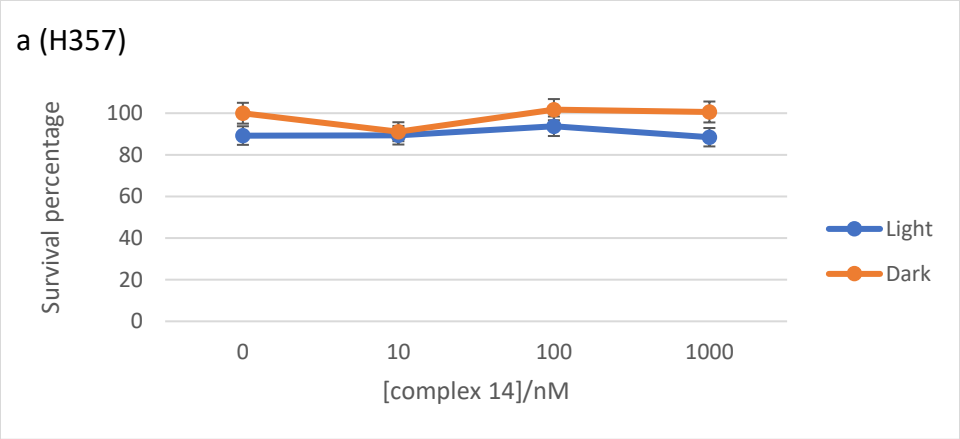

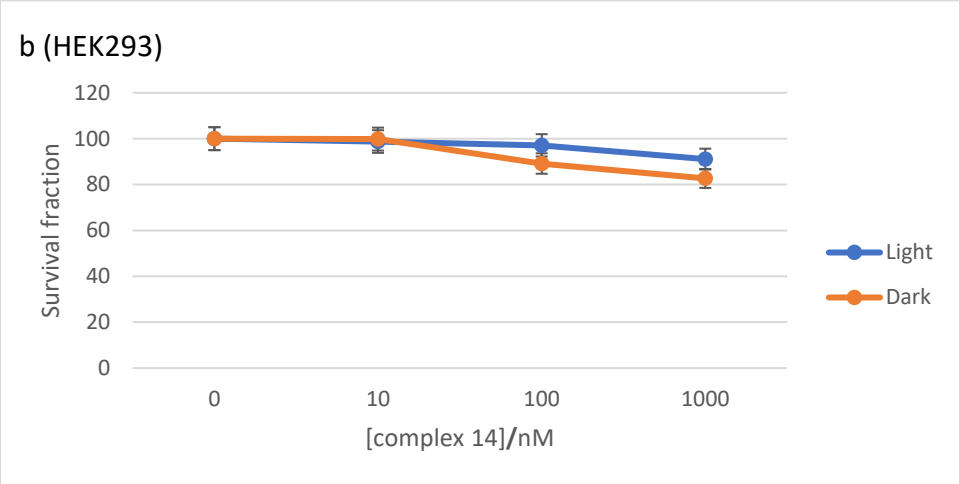

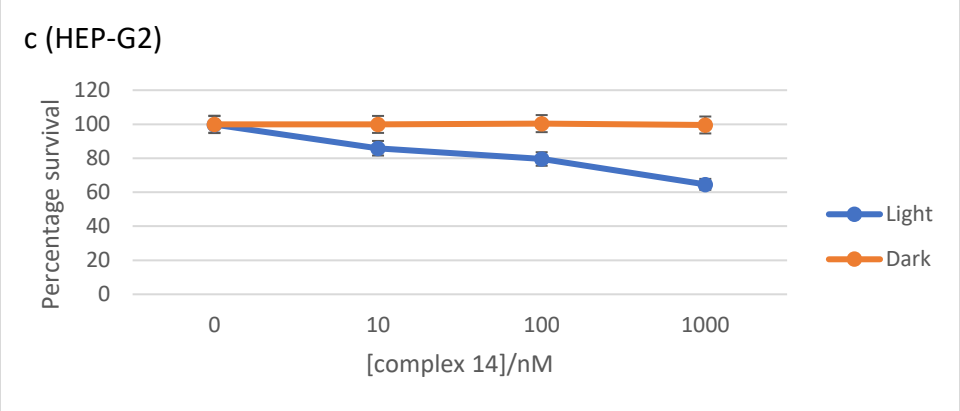

Figure 38- Survival of H357 (a), HEK293 (b), and HEP-G2 (c) cell lines pre-incubated for 2 h with complex 14 (+/- light). See text for details.

Once the localization within the cell was confirmed, complex **14** was tested for any toxic effects against a range of host cells. Three cell lines were chosen, H357 (epithelial squamous cell carcinoma), Hep-G2 (human hepatocellular carcinoma) and HEK293 (human embryonic kidney cells). The results are shown in Figure 38. Complex **14** showed least toxicity towards H357 cells with the viability being unaffected, even at higher concentrations, with or without light. Complex **14** exhibit low levels of cytotoxicity towards HEK293 cells, with over 80% of the cells surviving at the highest concentration used in both the light and dark samples. Hep-G2 cells were the most sensitive to treatment with some reduction in viability at 10 nM and 60% of cells surviving the 1000 nM concentration. All cells were unaffected by the highest concentration (0.2%) of DMSO used.

4.4 Targeting internalised bacteria

After establishing complex **14** is non-toxic to cells, especially at concentrations sufficient to kill bacteria, its ability to kill bacteria that are internalized in human cells was investigated. The results are shown in Figure 39.

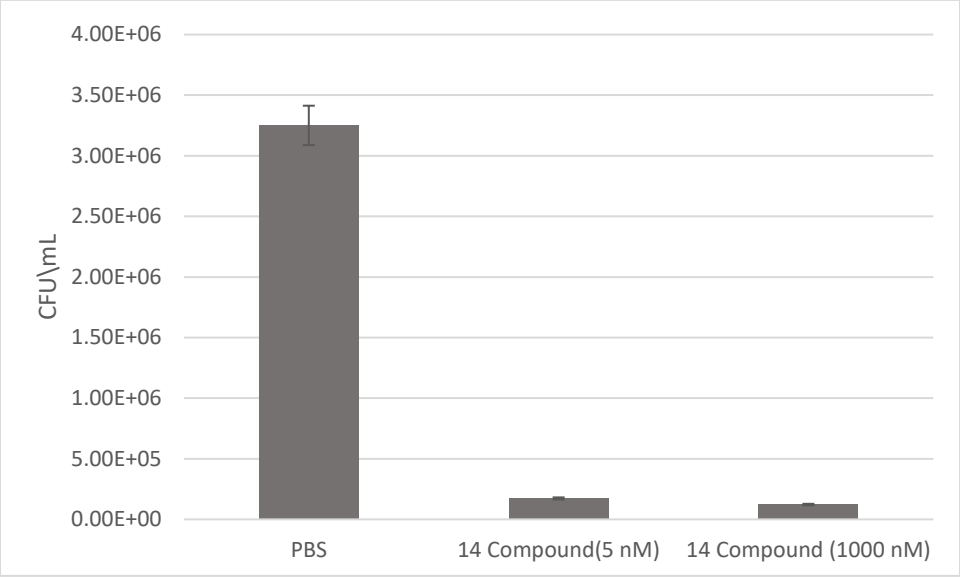

Figure 39- Survival of internalised P.gingivalis (NCTC 11834) treated with varying concentrations of complex 14 and irradiated with light (405 nm 3 min, 20 mW cm^{-2})

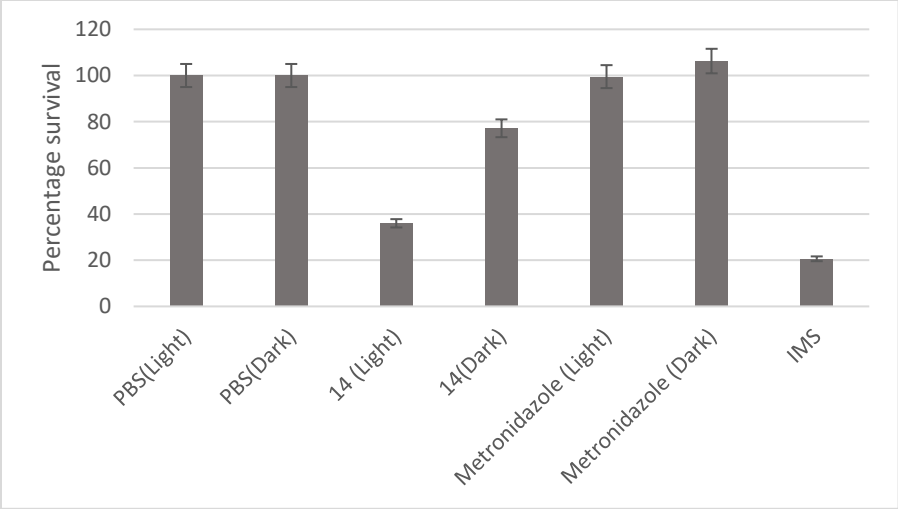

Figure 40- Survival of P.gingivalis (NCTC 11834) biofilms incubated with complex 14 (10 nM, 2h), metronidazole or Industrial Methylated Spirit (IMS) (positive control). Light dose = 405 nm 3 min, 20 mW cm^{-2} (n = 3)

The results show that intracellular bacteria are also sensitive to the aPDT treatment with an approximate reduction in viability of 99.9%. Thus complex **14** can target both internalised and external bacteria.

4.5 Antimicrobial effects on *P.gingivalis* biofilms

The effect of **14** on biofilms was also investigated. A primitive biofilm model consisting of *P.gingivalis* (NCTC 11834) was formed. As shown in Figure 40**,** complex **14** was able to reduce the viability of bacteria in biofilms by over 60% whereas metronidazole had no effect. It should be noted that due to the quantification technique used 100% killing could not be detected as shown by the IMS control.

4.6 Light microscopy studies

Confocal & Structured Illumination Microscopy (SIM) was used to examine the localisation of complex **14** inside *P.gingivalis*. The images were taken at two concentration (10 nM & 20 nM).

Z-slices of the SIM images (Figure 41) shows the rough localisation of complex **14** in *P.gingivalis*. The change in localisation pattern when increasing the concentration suggests complex **14** accumulates along the bacterial cell wall first followed by concentrating in the cytoplasm. The mechanism by which this occurs is not yet known.

The PDT effects of the complex on *P.gingivalis* was observed in real time on live cells using SIM with the help of the LIVE/DEAD® BacLight Bacterial Viability Kit. The kit consists of two stains, SYTO-9 and propidium iodide. SYTO-9 is able to bind to all types of nucleic acids irrespective of the cell integrity. Propidium iodide is only able to penetrate cells with damaged membranes and is able to displace SYTO-9 that is bound to nucleic acids. SYTO-9 and propidium iodide have excitation/emission maxima at 480/500 nm and 490/635 nm, respectively. Therefore, when combined together it is possible to observe the death of bacterial cells in real time by monitoring the emissions intensities at 500 nm & 635 nm. As bacteria die the intensity of 500 nm emission decreases and the intensity of the 635 nm emission increases. The DeltaVision OMX microscope consists of a 405 nm laser. This was used as the light source to activate the PDT effects of complex **14**. After 3 minutes of irradiation with the 405 nm, the changes in the A568 & FITC (525 nm & 595 nm, respectively) channels were observed. As seen on Figure 42, the intensity of the A568 channel increases significantly while the intensity of the FITC channel decreases over the course of 30 minutes. There is already some emission at timepoint 0 minutes. We believe this is due to the damage done prior to collecting data in these channels (i.e. during irradiation/activation with the 405 nm laser). Even so, this experiment suggests bacteria continue to die even after the initial irradiation. Furthermore, this also suggests that complex **14** does significant damage to bacterial membranes. This is evident from the increase

in emission from propidium iodide as it would not be able to penetrate membranes that are intact.

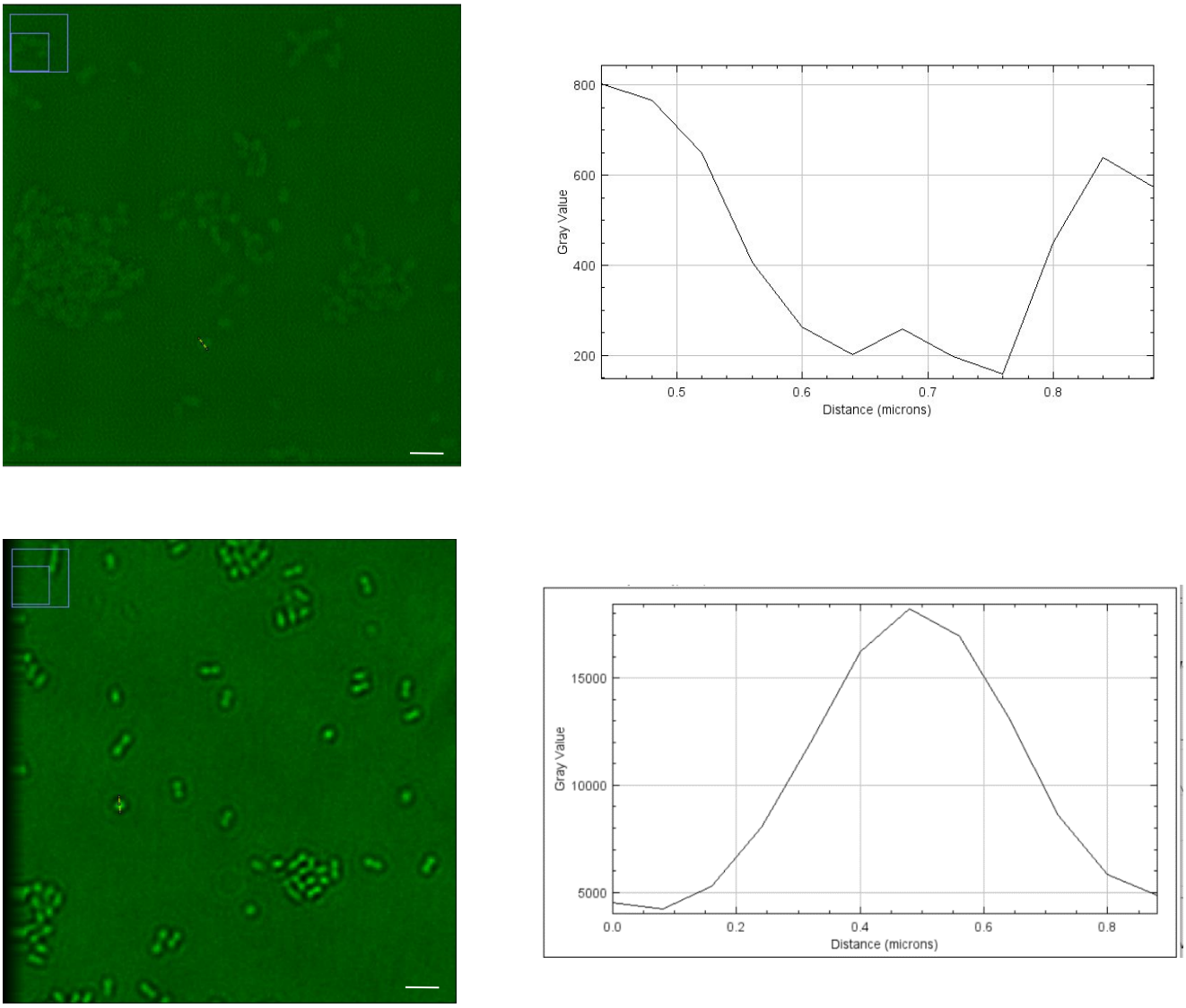

Figure 41- A single z-slice of SIM image (left) and emission line (right) along the yellow line on the left, indicating uptake complex 14 by P.gingivalis. Concentration = 10 nM (top) & 20 µM (bottom) scale bar = 6 µm

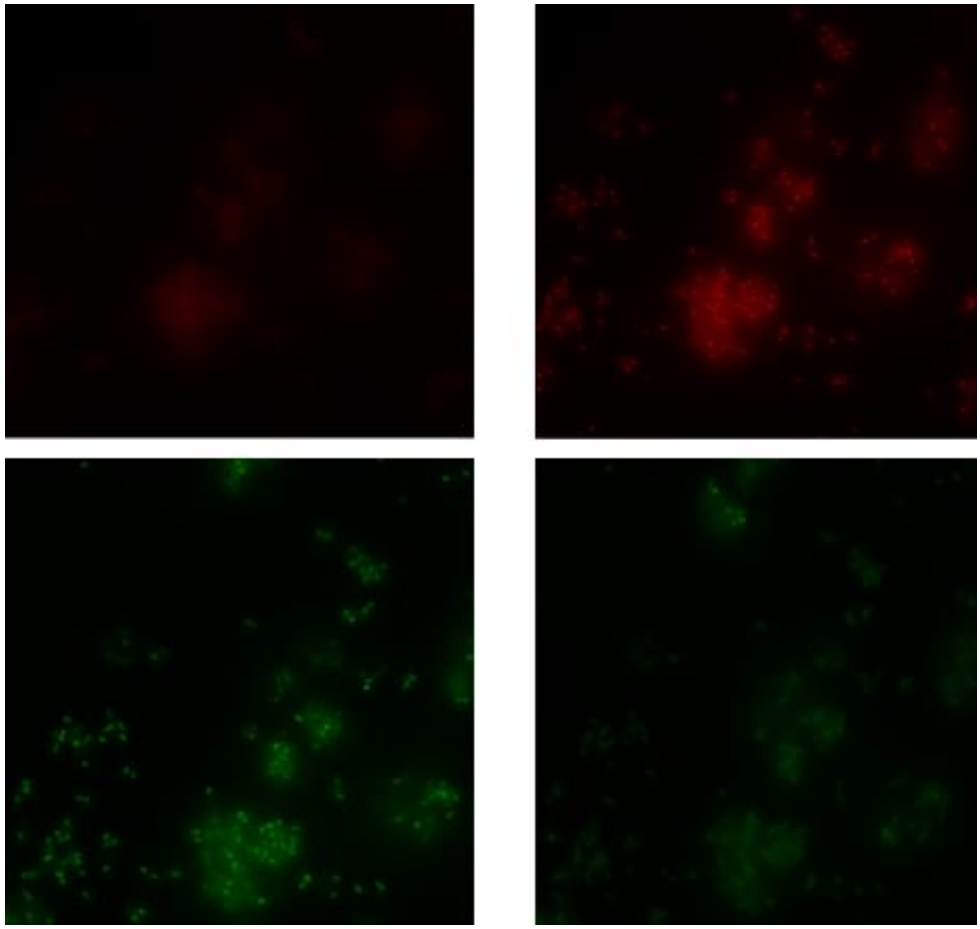

Figure 42- Live SIM images of P.gingivalis treated with complex 14 (10 nM, 2h) followed by BacLight LIVE/DEAD stain Top- A568 Time= 0s (left) and Time = 30 min (right) after being irradiated with 405 nm laser. Bottom- FITC Time= 0s (left) and Time = 30 min (right) after being irradiated with 405 nm laser (need to add emission graphs over the 30 mins)

The LIVE/DEAD stain kit was also used to observe the effect complex **14** has on *P.gingivalis* (Figure 43) and we were able to observe a concentration dependent increase in the red emissions for both bacterial biofilms. This confirms the above PDT experiment on biofilms (Figure 40) which shows complex **14** to be effective at damaging bacterial biofilms.

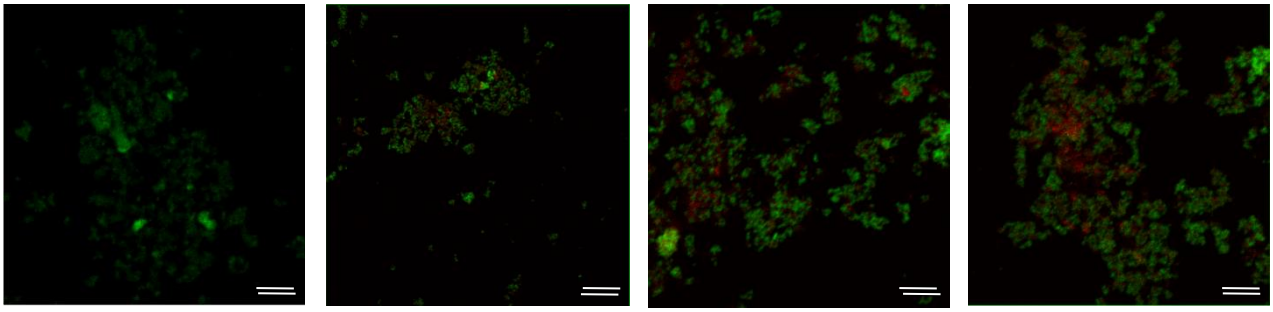

Figure 43- Confocal images (A568/FITC channel merge) of P.gingivalis (11834) complex 14 (2h) and treated with light (405 nm, 20 mWcm^{-2}, 3 min). The biofilms were then treated with BacLight LIVE/DEAD stain. scale bar = 19 µm

4.7 Electron microscopy studies

Lastly, the uptake of **14** and the damage it causes to bacteria was studied using transmission electron microscopy. The resulting TEM images are shown in the following Figure 44.

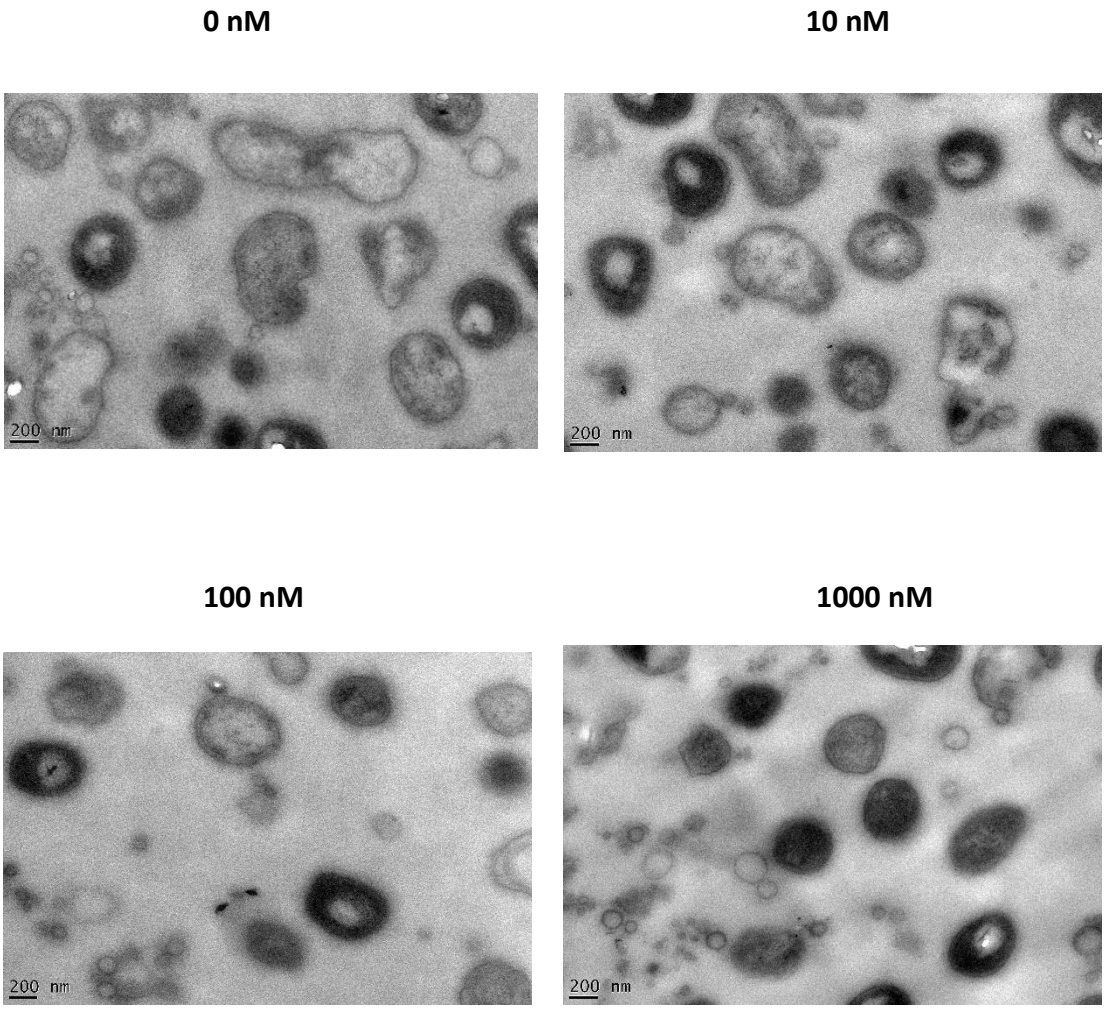

Figure 44- TEM images of P.gingivalis treated with only complex 14 and OsO4

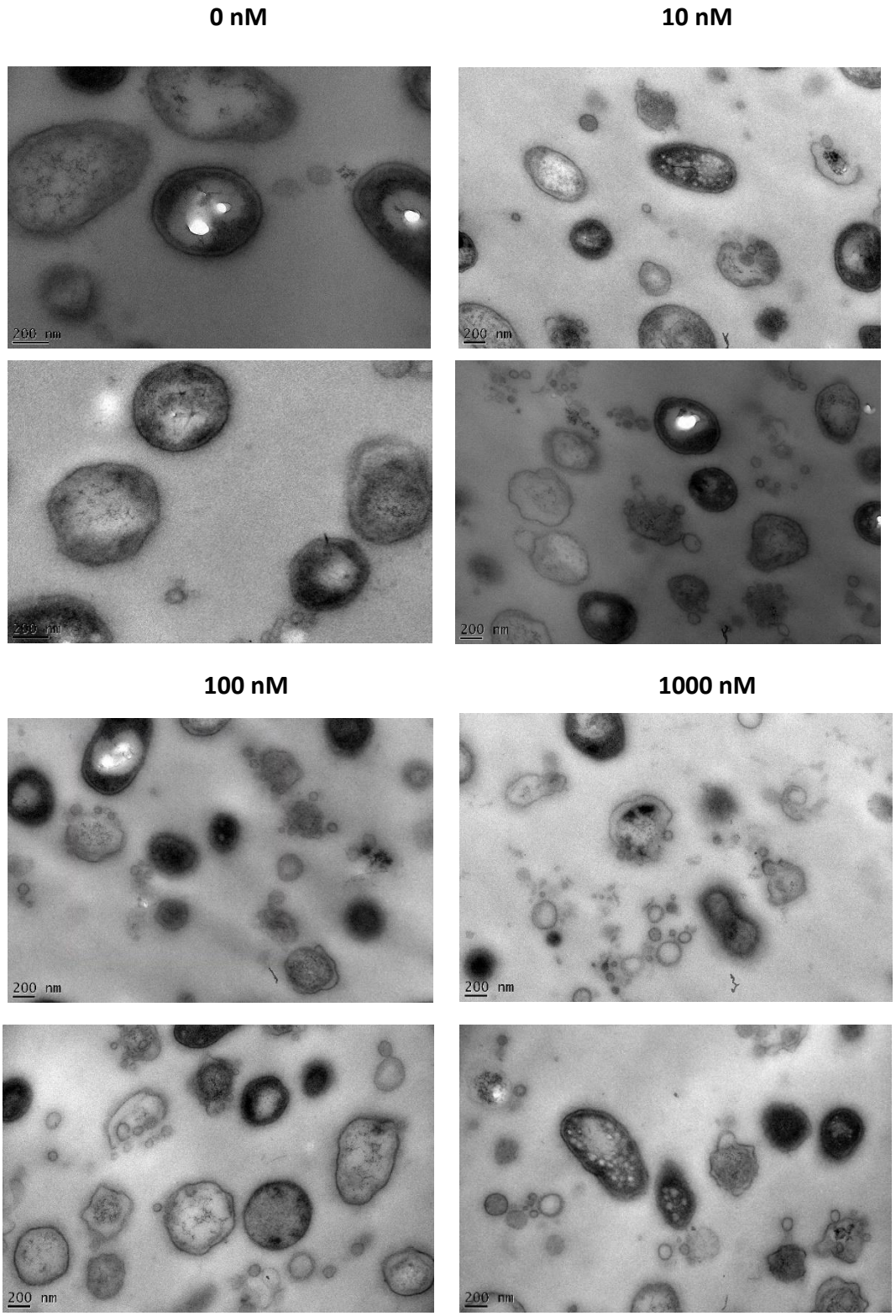

Figure 45- TEM images showing damage caused by complex 14 to P.gingivalis, following irradiation. The sample not treated with compound 14 shows well-structured and turgid bacterial cells, indicating they are healthy. As the concentration is increased the bacteria start to show more damage to the cell wall. They are also shown to release more vesicles. This shows that they have been damaged by the PDT treatment and are under stress.

The TEM images show a clear increase in contrast going from the unstained sample to a sample stained with **14** at a 10 nM concentration. The contrast becomes more prominent when the concentration is increased to 1000 nM. At this concentration a high amount of contrast and detail is seen in the cell wall. Furthermore, the bacteria seem fully intact even at higher doses confirming that there is no dark toxicity.

A second set of TEM images were taken following a PDT treatment with complex **14**. The samples were treated with standard TEM contrast reagents this time to get a full understanding of the damage caused by the complex on the bacteria. The images (Figure 45) show increased membrane damage as the concentration is increased. At 5 nM concentration bacteria show membranes with pores or misshaped membranes indicating they are stressed. At 100 nM the membranes look increasingly misshaped with some cells appearing to be bursting. At the highest concentration the bacteria show marked increase in burst membranes. The TEM images are also in agreement with the light microscopy studies. The increase in contrast of the cell wall as the concentration increases confirms the results of the SIM images, which showed affinity of complex **14** towards the cell wall. The live imaging also suggested complex **14** damages membranes. This is clearly confirmed in the TEM images.

4.8 Conclusions

The novel cyclometalated iridium complex, complex **14**, was investigated for PDT effects against *P.gingivalis,* a pathogen involved in severe forms of periodontal disease.. The new complex, **14**, at a concentration of 5 nM, demonstrated its ability to reduce *P.gingivalis* colonies by 99.9% ($3\log_{10}$ reduction) in the presence of a 405 nm light while not being active against bacteria in the dark even at high concentrations. This is a very low concentration when compared to the current antibiotic treatment against *P.gingivalis*, metronidazole, which has a minimum inhibitory concentration of approximately 73 nM.[107] It was also significantly better than the current PDT system in the market, which shows only a 50% reduction in bacterial colonies. Most importantly, the complex is able to enter cells and kill internalised bacteria. Although bacteria in biofilms are more resistant to conventional antibiotic treatment, the new complex performed well against a primitive *P.gingivalis* biofilm model with more than 60% reduction in bacterial biofilm. TEM images show that the complex localises in the outer-membranes of the bacteria and is causing its rupture when irradiated with light. It is important that the treatment is not toxic to host cells. The toxicity of the complex was tested against three cells lines (H357, HEK293 and HEP-G2) and all cell lines were unaffected by the complex without treatment of light. H357 and HEK293 showed little or no toxicity in the presence of light, whereas HEP-G2 were more sensitive at higher concentrations of the complex.

.

Chapter 5

Antimicrobial effects of complex 14 on Pseudomonas aeruginosa

After successfully showing the ability of complex **14** to induce death of *P.gingivalis* without harming human cells *in-vitro,* the potential commercialisation of the complex was explored. This involved conducting market research through the Lean Launch Program, a pre-accelerator programme designed for researchers to verify the market needs for their research. A major finding of the market research was that there is a great need for antimicrobials that can cure infections on the skin caused by conditions such diabetic foot ulcers, surgery and burns. The bacteria that are most active in these infections include *Pseudomonas aeruginosa*. This chapter explores the experiments conducted to investigate the efficacy of complex **14** against *P.aeruginosa*.

5.1 Introduction to *Pseudomonas aeruginosa*

P.aeruginosa is an ubiquitous, aerobic opportunistic Gram-negative bacteria. In the UK, it accounts for 25% of ventilator associated pneumonia and has become the biggest global cause of healthcare-associated infections.[108] The number of infections caused by this bacteria in the UK has increased by 16% from 2009. This is at a rate of approximately 8.1 infections per 100,000 people.[109] The colonisation rate is shown to increase from 0-24% to 50% during hospitalisation.

The increase in *P.aeruginosa* cases globally has led the World Health Organisation to list the bacteria as a priority pathogen in its global priority (group 1) list of antibiotic-resistant bacteria.[110]

P.aeruginosa is a highly tactful in developing resistance to antibiotics. The treatment options for *P. aeruginosa* are very limited due to the bacteria's ability to quickly form resistance through genetic mutations and/or exchanging of resistant plasmids. It has developed all known mechanisms of resistance and has become resistant to the all of the common classes of antibiotics, namely, aminoglycosides, quinolones and beta-Lactams (including penicillin). *P. aeruginosa* has evolved to express enzymes that are capable of destroying antibiotics such as the enzyme cephalosporinase, which catalyses the breakdown of beta-Lactams.[111] It also has a low number of OprD proteins and high number of efflux systems causing it to have reduced permeability in its outer membrane.[112,113] These factors have caused an urgent need for the development of alternatives to antibiotics in order to counteract the increasing threat of *P.aeruginosa*.

5.1.1 P.aeruginosa biofilms

One of the biggest factors contributing to its formation of resistance to antibiotics is its ability to form strong biofilms allowing it to survive in harsh conditions, both biological (e.g. immune response, antibiotics etc.) and non-biological (e.g. mechanical washing, scrapping etc.).[60] It is thought *P. aeruginosa* biofilms are the main factor contributing to its thriving in hospitals. However, unlike *P.gingivalis*, *P.aeruginosa* does not need an attachable surface to form biofilms. For example, there have been reports of *P.aeruginosa* biofilms forming in the lungs of cystic fibrosis patients.[114] *P.aeruginosa* biofilms are very sophisticated and have complex networks of channels optimised for better distribution of nutrients and plasmids across the biofilms.[115]

The extracellular proteins contribute towards the critical function of maintaining the biofilm's rigidity as well as connecting the bacteria to the extracellular polysaccharides (EPS) matrix consisting of polysaccharides such as galactose and glucose. These biomolecules are essential for the integrity of the biofilm architecture.[116] For example, it was shown that increased expression of amyloid protein causes increase in the number of aggregate phenotypes leading to enhanced biofilm formation.[117]

Another important factor in *P.aeruginosa* pathogenesis is extracellular DNA (eDNA) which was first reported in 2002.[118] eDNA plays the essential role in acquiring resistance from other resistance species through the exchange of resistance genes. The eDNA can be produced endogenously or exogenously.[119] Endogenously produced eDNA is released into the environment after lysis of bacteria upon exposure to sub-inhibitory concentrations of antibiotics. This is thought to be a mechanism for the increase in resistance of bacteria within patients who do not adhere to the complete treatment.[120] A simplified diagram for the stages of biofilm formation in *P.aeruginosa* is shown in Figure 46.

It is now well accepted that bacteria in biofilms are about 1000-times more resistant to antibiotics. Several factors contribute towards this increased resistance. Firstly, the biofilm acts as a physical barrier for antibiotics. Another is that the biofilm contains large volumes of water, which will reduce the working concentration of the antibiotics.[121] Thirdly, there is a gradient of nutrients and oxygen within the biofilm. It is possible that areas with lower concentrations of oxygen reduce the efficacy of antibiotics such as tobramycin and ciprofloxacin.[122] The nutrition gradient also means that areas with low nutrition have low metabolism, leading to reduced efficacy of antibiotics which require active metabolism to function. Finally, bacteria in biofilms

are in close proximity to one another when compared to their planktonic counterparts. This makes the exchange of resistance genes much easier.[123]

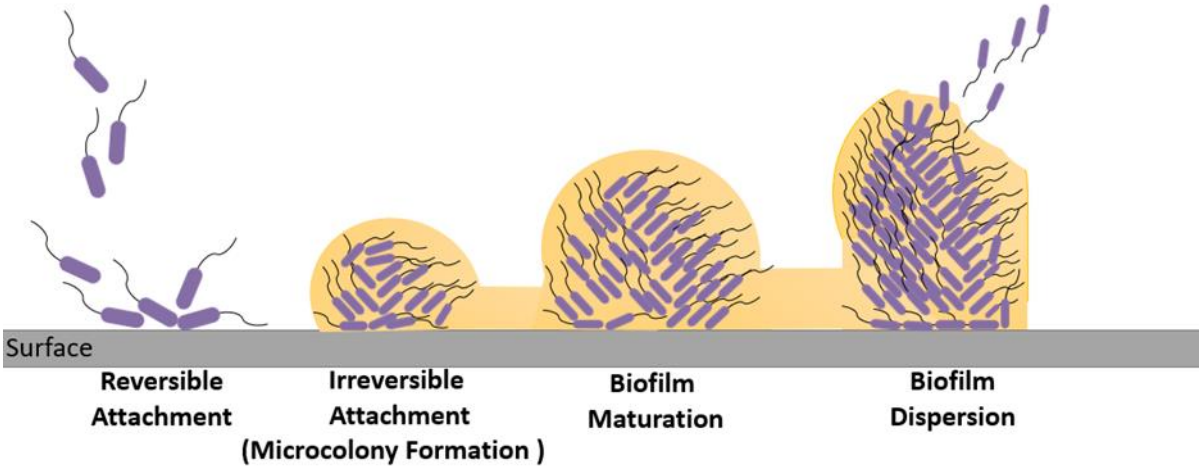

Figure 46- Stages of biofilm formation in P.aeruginosa (from ref[124])

5.1.2 Treatments for P. aeruginosa infections

Traditional antibiotics are the first line of treatment against *P. aeruginosa*. However, this bacteria accounts for the highest rates of resistance against levofloxacin and ciprofloxacin with resistance rates of about 20 -35%. It is also highly resistant to gentamicin and exhibits a resistance rate of 12 -22%. The problem is magnified when multidrug resistant strains are taken into account; the prevalence of strains resistant to 3 or more antibiotics have increased from 4% to 15% from 1993 to 2020.[60] It is possible that PDT could serve as an alternative to treat *P.aeruginosa* infections. PDT does involve not traditional antibiotic mechanisms. This means that the chances of *P.aeruginosa* already having resistance to complex **14** are low. PDT mechanism can also be better controlled than antibiotic mechanisms since the compound is active only when irradiated with

light. Lastly, the activation wavelength for complex **14** is 405 nm. This is also in the same range as light treatment for wounds where blue light is used to improve blood flow to the wounds and aid in healing. Some clinicians we have interviewed believe that the PDT treatment at 405 nm could have a dual effect of increasing blood flow to the wounds while treating the infection directly.

5.2 Complex 14 on *P.aeruginosa*

Complex **14** was tested on *P.aeruginosa*, initially at 5 nM, which was the initial concentration used for *P.gingivalis*. The bacterial reduction at this concentration was insignificant. In order for the complex to do the same rate of damage as to *P.gingivalis*, the concentration had to be increased to 2 µM as shown on Figure 47. At this concentration approximately, $1\log_{10}$ reduction in bacterial colonies was observed. The complex continued to reduce bacterial counts until 20 µM after which the reduction rate plateaued at 2Log_{10} reduction. The IC_{50} is approximately 1 µM. Although the reduction in bacterial count is significant, the concentrations used are likely to cause harm to human cells, especially to hepatic cells. It should be noted that this toxicity is only present in the present of the light source. Harm to the liver can be avoided if the liver is not irradiated.

Confocal microscopy was used to confirm the uptake of complex **14** by *P.aeruginosa* (Figure 48). The images show that *P.aeruginosa* has taken up complex **14** evident from increased emission in the all three channels. Interestingly, there is emission in DAPI channel in the sample treated only with PBS. This is possibly due to fluorescent pigments produced by the bacteria (discussed below).

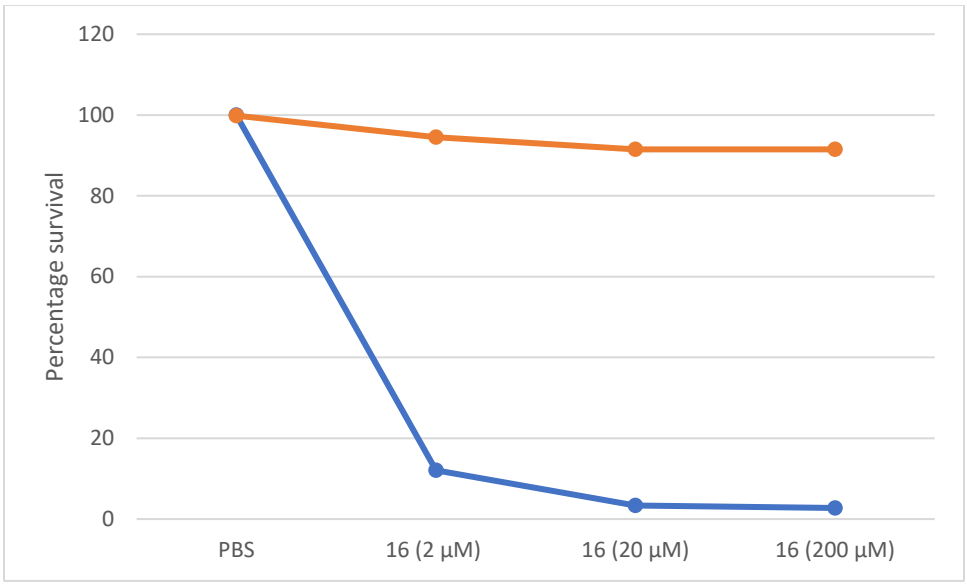

Figure 47- Percentage survival of P. aeruginosa incubated with complex 14 (+/- light) (n =2)

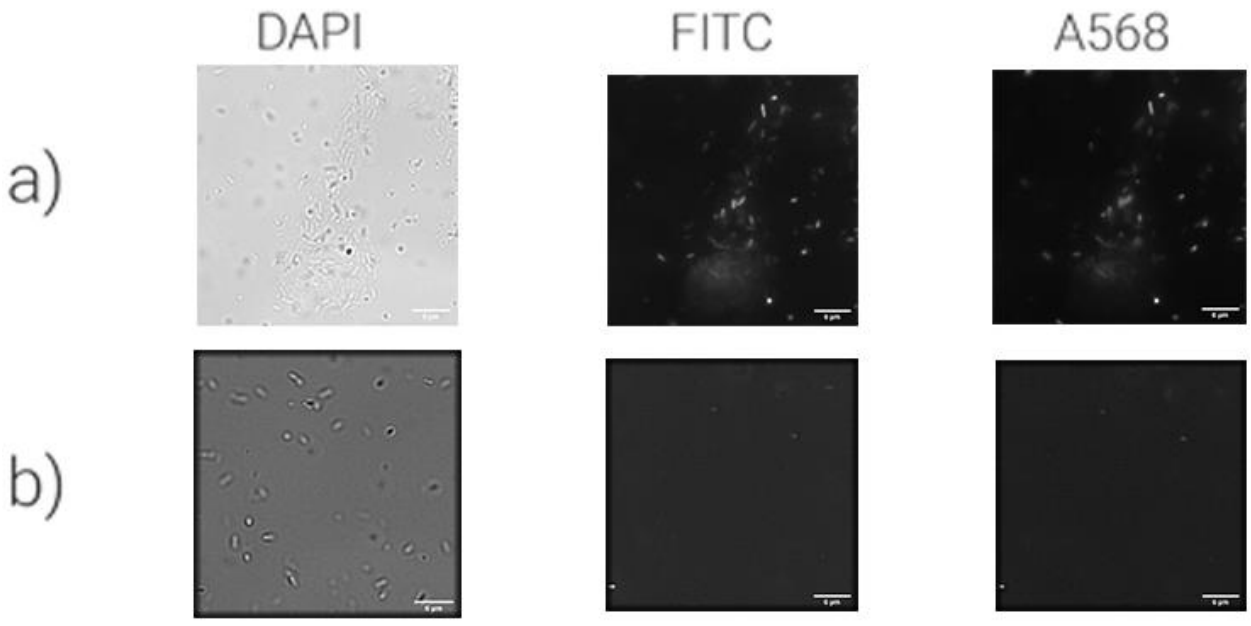

Figure 48- Confocal image of P. aeruginosa treated with a) complex 14 (20 µM, 2h incubation) or b) PBS scale bar = 6 µm

There is a significant difference between the IC_{50} values of **14** against *P.gingivalis* and *P.aeruginosa* (5 nM and 1 µM respectively). This stark difference can be explained by the intrinsic resistance of *P.aeruginosa* towards ROS. The mechanism of ROS inhibition by *P.aeruginosa* are complex and the studies are still in their infancy.[125] That said, the literature is in agreement that the resistance to ROS comes from a combination of detoxifying enzymes, transcriptional regulators, pigment production, quorum sensing (coordination among individual bacteria within a colony to share genetic information) and carbon metabolism. In context of PDT, the most important factors to ROS resistance are arguably the detoxifying enzymes and pigment production. The detoxifying enzymes include catalase, peroxidase, superoxide dismutase and alkyl hydroperoxidase.[126] Most living cells have some or all of these enzymes. However, the utilisation of these enzymes by *P.aeruginosa* particularly within its biofilms makes them troublesome for the immune system and antimicrobials. For example, *P.aeruginosa* has three varieties of catalases and four variants of alkyl hydroperoxidases. This allows the bacteria to survive within host macrophages.[127]

The pigments secreted by *P.aeruginosa* are pyocyanin, pyomelanin and pyoverdine as shown in Figure 49. The chemical mechanisms by which these pigments neutralise ROS were not reported. However, it is possible these are highly conjugated and fluorescent systems and are capable of neutralising the effects of ROS by accommodating radical species in the aromatic orbitals. This reduces the potency of the free radicals. There has been a report of the pigments generated by

P.aeruginosa showing protection against oxidative stress caused by PDT.[128] Here, the researchers exposed *P.aeruginosa* mutants, which produce a higher volumes of pigments the PDT effects of Toluidine Blue-O & 5,10,15,20Tetrakis-(1-methyl-4-pyridyl)-21H,23porphine,tetra-p-tosylate (TMPyP) and compared the bacterial death with wild type *P.aeruginosa* exposed to the same compound. They discovered that bacteria which possess larger volumes of the pigment pyomelanin led to increased counteracting of the effects caused by both Type I and Type II PDT pathways (i.e. bacterial death due to ROS and singlet oxygen respectively).

Detoxifying enzymes and pigment production will directly affect the PDT mechanism by essentially inhibiting the Type I PDT pathway and partially inhibiting the Type II pathway. This could also potentially lead to new forms of resistance towards PDT agents.

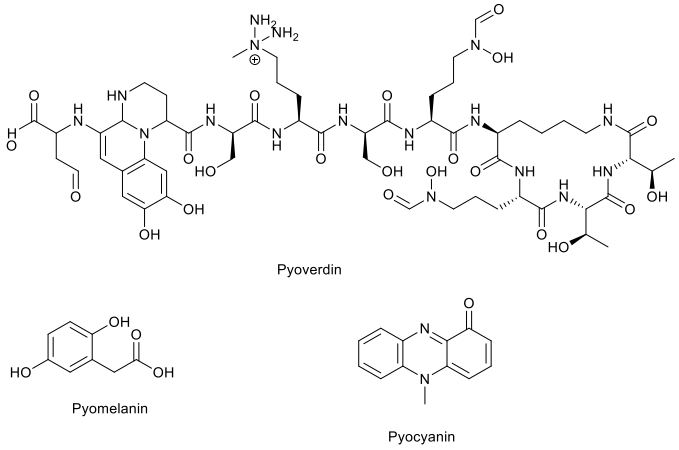

Figure 49- Pigments produced by P.aeruginosa

5.3 Antimicrobial effects on *P.aeruginosa* biofilms

Complex **14** was tested on a primitive biofilm model of *P.aeruginosa.* As shown in Figure 50, complex **14** showed great efficacy against the biofilms, reducing bacterial colonies by over 60%

while showing minimal toxicity in the dark. Due to the quantification technique used 100% killing could not be detected as shown by the IMS control (positive control). Whilst this indicates that complex **14** has potential to be efficient against *P.aeruginosa* biofilms, this model is a primitive model consisting of only bacterial species. In reality biofilms will have multiple bacterial species and will likely be more resistant to antimicrobial effects of **14.** Confocal images of the *P.aeruginosa* biofilms were taken following treatments (Figure 51). LIVE/DEAD stain was used to observe the bacterial cell death. The images confirm the above findings. The emissions in the red channel increases with increasing concentration of complex **14**, indicating bacterial cell death. Interestingly, the distribution of the dead cells appear uniform throughout the biofilm. This is very evident in the sample treated with 20 µM. This would indicate that despite the uneven distribution of oxygen in the biofilm, the PDT effect appears to be uniform.

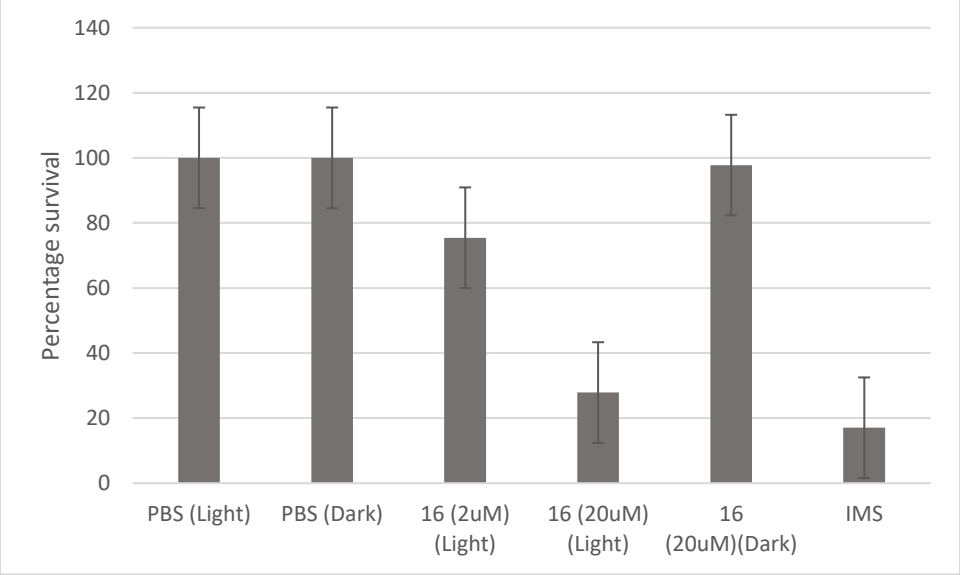

Figure 50- Survival of P.aeruginosa incubated with treated with 14 (2 or 20 µM. 2h). Positive control = IMS & light dose = 405 nm, 3 min, 20 mW cm^{-2} (n = 2)

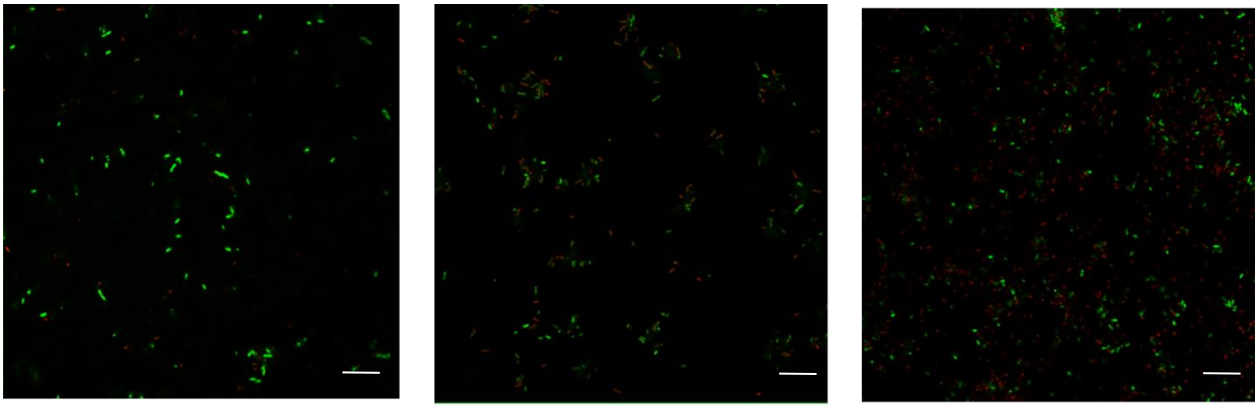

0 µM 2 µM 20 µM

Figure 51- Confocal images (A568/FITC merge) of P.aeruginosa (bottom) biofilms treated with varying concentrations complex 14 (2h incubation) and treated with light (405 nm, 3 min) scale bar = 19 µm

5.4 Three-Dimensional (3-D) model experiments

The PDT experiments conducted on planktonic *P.aeruginosa* and *P.aeruginosa* in biofilms the bacteria undergo cell death in the presence of a light activated complex **14**. In order to gauge the performance of the complex on human skins, we tested the effects of complex **14** on 3-D skin models infected by *P.aeruginosa*. 3-D skin models are considered a better alternative to animal models. In addition to ethical reasons, the skins of animals used for testing are very different from humans, especially in the innate immune responses.[129]

Previously, human skins remaining from surgeries have been used. However, experiments conducted using these models are difficult to replicate. A more reliable, physiological relevant 3D model that can be grown in the lab has been developed by Dr Joanna Shepherd and co-workers at the University of Sheffield.[130] Here, a sterile decellularized dermis (DED) acts as the base to seed a known number of fibroblasts and keratinocytes supplemented with known amount of growth medium.

In collaboration with Dr Shepherd, we utilised these skin models to investigate the PDT effects of complex **14** on a physiologically relevant model. The models were wounded by creating burning them with a heated metal inoculating loop. The wounds were then infected with an overnight culture of *P.aeruginosa*. The infection was allowed spread for 24 hrs (Figure 52). It is possible to let the infection spread up to 72 hours. Beyond this point, the model will be destroyed by the bacteria.

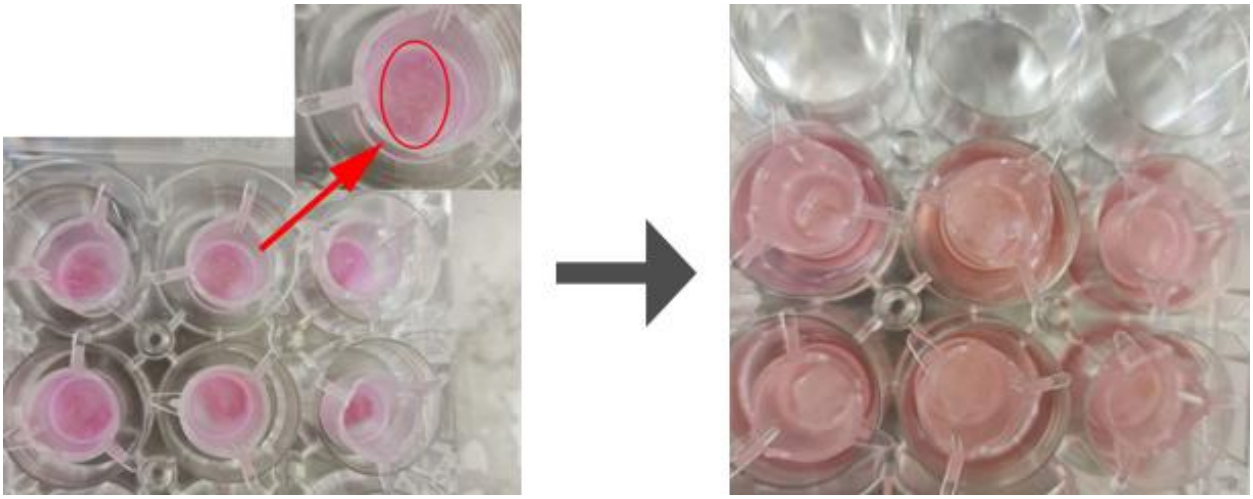

Figure 52- 3-D Skin models after wounds were introduced via burning (left). The red circle shows the appearance of the burn wound. The wounds were then infected and the infection was allowed to spread for 24 hour (right)

After the 24 hour infection period, the growth media were removed and treated with complex **14**, in a similar fashion to the planktonic and biofilm experiments. The light dose was changed slightly; the wavelength remained the same at 405 nm but the power was increased to 40 $mWcm^{-2}$ and the exposure time was increased to 15 minutes. This was to ensure complete penetration

of the light into the model and ensure even illumination. The results are shown in Figure 53.

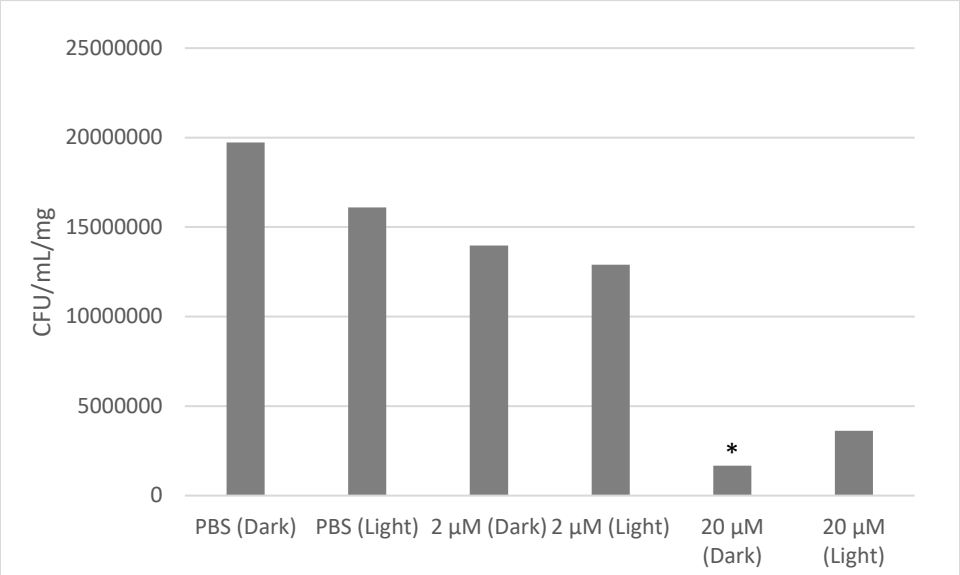

Figure 53- Efficacy of complex 14 (concentrations shown & +/- light) in treating 3D skin models infected with P.aeruginosa. Light dose = 405 nm, 40 mWcm^{-2}, 15 minutes (n = 1). The asterisk indicates an anomalous data (discussed in main text)

The results show a linear relationship between the concentration of complex **14** and the rate of bacterial cell death. At 20 µM (+light) a 1log$_{10}$ reduction in bacterial colonies is observed. This is lower than the 2log$_{10}$ reduction observed at the same concentration on planktonic bacteria. It has been shown that after 24 hours *P.aeruginosa* is able to invade the underlying dermis.[130] They are also likely to form stronger biofilms as well as invade cells. These factors may be contributing to the increased resistance of *P.aeruginosa* in 3-D skin models. The results also indicate that the light source alone maybe killing the bacteria as shown by the sample treated with PBS and light. The sample treated with 20 µM of complex **14** and kept in the dark show the greatest reduction. This is an anomaly since previous experiments showed no activity at this concentration without being illuminated with light. During the experiment this particular skin sample lost its integrity

and disintegrated into a semi-solid material. It is possible some bacteria trapped in the skin were lost from the sample leading to a reduced bacterial count.

5.5 Conclusions

Complex **14** was investigated on *P.aeruginosa,* a bacteria responsible for severe skin infections and fatal sepsis, for PDT activity. Although more resistant that *P.gingivalis* at lower doses, complex **14** was able to reduce bacterial colonies by 90.0% when the concentration was increased to 2 μM. This is still relatively a low dose compared to compared to the minimum inhibitory concentrations of antibiotics such as gentamicin and ciprofloxacin which are greater than 10 μM.[131] The uptake of the complex was confirmed by confocal microscopy. Complex **14** was also tested on *P.aeruginosa.* At 20 μM concentration, the complex was able to reduce the size of biofilms by 60%. Furthermore, the complex was tested on 3D skin models infected with *P.aeruginosa*, which is a more physiologically relevant testing method. The complex was able to reduce the infection at 20 μM but not as strongly as with planktonic bacteria.

Concluding remarks and future work

With an increase in antibiotic resistance, there is an urgent need to replace antibiotics. During this project we have attempted to address this issue by developing an antimicrobial based on a form of light therapy known as PDT. A previously reported anticancer PDT agent (complex **13a**) was modified with an antibiotic moiety, metronidazole to form complex **14**. Complex **14** was first synthesised using conventional refluxing methods. The synthesis was optimised using microwave-assisted synthesis. The synthesis leading up to the final step, coordinating the equatorial ligand to the iridium dimer, was greatly improved by the use of microwave-assisted synthesis. The final step needs be more optimised to improve yields. Optimisation may be done using different reaction times, temperatures and solvent mixtures.

Complex **14** showed great efficacy is reducing the colonies of *P.gingivalis*. The IC_{50} was very low at 5 nM. The most common antibiotic used to treat *P.gingivalis* infections is metronidazole, which has an IC_{50} of 73 nM. The efficacy of complex **14** was compared against a commercially available system called Periowave™ that is used to cure periodontal disease using PDT. The data suggests that the Periowave™ system has minimal effects against *P.gingivalis* with the system reducing the colony count by only 63%.

Complex **14** showed more killing than its closely related complex **15**, which had the same basic structure as complex **14** but without the metronidazole. Interestingly, pure metronidazole did not show any killing in this experiment. This indicates that the increased bacterial killing shown by complex **14** is due to a factor other than pure antibiotic effects from its metronidazole. That

is, metronidazole may be involved in the photochemistry of the complex and generates free radicals of its own, which enhances the PDT capabilities of the complex. In the future, the radical forming mechanism should be studied using radical scavengers such as galvinoxyl. Further free radical studies can be done with electron paramagnetic resonance spectroscopy, which should be able to detect if an unpaired electron is present on the metronidazole moiety upon excitation. Transient absorption spectroscopy also needs to be carried out on complex **13a**, **14** and **15**. This is needed to investigate any changes to the electron transfer mechanism that may occur to complex **14** due to the addition metronidazole.

The TEM and SIM images indicate complex **14** has an affinity towards the cell wall of bacteria and TEM images show evidence of it causing bacterial cells to burst upon irradiation with light. However, the biological mechanism by which this happens needs to be investigated further. Uptake of the complex by live bacteria can be investigated further with stimulated emission depletion microscopy. We demonstrated the ability of complex **14** to kill bacteria using live SIM imaging. The studies using live bacteria to study PDT effects can be enhanced using Atomic Force Microscopy (AFM). The resolution of AFM can be used to study the cell wall further and elucidate the damage shown by TEM. Furthermore, the use of mutants with varying structural differences to the cell wall can be used to investigate the targeting mechanisms used by complex **14**.

The new complex **14** was also tested on *P.aeruginosa*. The complex bacterial killing pattern was similar to *P.gingivalis*. But the concentration needed to be increased to 2 μM to observe any significant killing. After successfully demonstrating its ability to reduce colonies of *P.aeruginosa* we tested the ability of complex **14** on a more physiologically relevant system. This was done by testing its ability to reduce *P.aeruginosa* colonies that have infected a 3-D skin model. Whilst it

showed dose dependent bacterial killing, the rate at which it kills bacteria was reduced. However, this was only shown on one experiment and many more repeats are needed to confirm these findings. The next steps in this research would be to further investigate the effects of complex **14** on more clinically relevant systems such as 3-D skin models and 3-D oral tissues. The Franz cell chamber is an assay used to investigate the depth of skin penetration by a topical therapeutic agent. In order to move to the clinical trials, the depth of penetration of complex **14** into the skin needs to be investigated using the Franz cell using human skin models. Histology assays coupled with confocal microscopy should be used to get a deeper understanding of the mechanism within a more clinically relevant system.

Although complex **14** showed great efficacy in reducing both *P.gingivalis* and *P.aeruginosa* colonies with PDT, its structure needs to modified to absorb in the visible light region to improve its clinical efficacy by increasing the depth of penetration of the light source. This can be done by tuning the energy gap between the HOMO and the LUMO. The HOMO is located on the phenyl ring of C^N ligand and Ir(III) centre, whereas the LUMO is distributed on the pyridine ring of the same ligand. Addition of electron withdrawing groups in the pyridyl moiety stabilises the LUMO and reduce the energy gap between the HOMO and LUMO. Variants of complex 14 with electron withdrawing groups on the C^N ligand can be synthesised to improve the absorption wavelengths.

Complex 14 shows great potential. Its prospects of reaching a clinical setting can be greatly improved with these additional data and mechanistic studies.

Appendix 1

Components	**Molecular Weight**	**Concentration (mg/L)**	**mM**
Amino Acids			
Glycine	75	30	0.4
L-Arginine hydrochloride	211	84	0.398104
L-Cystine 2HCl	313	63	0.201278
L-Histidine hydrochloride-H2O	210	42	0.2
L-Isoleucine	131	105	0.801527
L-Leucine	131	105	0.801527
L-Lysine hydrochloride	183	146	0.797814
L-Methionine	149	30	0.201342
L-Phenylalanine	165	66	0.4
L-Serine	105	42	0.4
L-Threonine	119	95	0.798319

L-Tryptophan	204	16	0.078431
L-Tyrosine	181	72	0.39779
L-Valine	117	94	0.803419
Vitamins			
Choline chloride	140	4	0.028571
D-Calcium pantothenate	477	4	0.008386
Folic Acid	441	4	0.00907
Niacinamide	122	4	0.032787
Pyridoxine hydrochloride	206	4	0.019417
Riboflavin	376	0.4	0.001064
Thiamine hydrochloride	337	4	0.011869
i-Inositol	180	7.2	0.04
Inorganic Salts			
Calcium Chloride (CaCl2-2H2O)	147	264	1.795918
Ferric Nitrate (Fe(NO3)3"9H2O)	404	0.1	2.48E-04
Magnesium Sulfate (MgSO4-7H2O)	246	200	0.813008

Potassium Chloride (KCl)	75	400	5.333334
Sodium Bicarbonate (NaHCO3)	84	3700	44.04762
Sodium Chloride (NaCl)	58	6400	110.3448
Sodium Phosphate monobasic (NaH2PO4-2H2O)	154	141	0.915584
Other Components			
D-Glucose (Dextrose)	180	1000	5.555555
Sodium Pyruvate	110	110	1

Table 2- Composition of Dulbecco's Modified Eagle Medium (DMEM)

Distilled Water	1 L
brain extract	7.8 g/L
dextrose	2.0 g/L
disodium phosphate	2.5 g/L
heart extract	9.7 g/L
proteose peptone	10.0 g/L
sodium chloride	5.0 g/L

Table 3- Composition of Brain Heart Infusion Broth

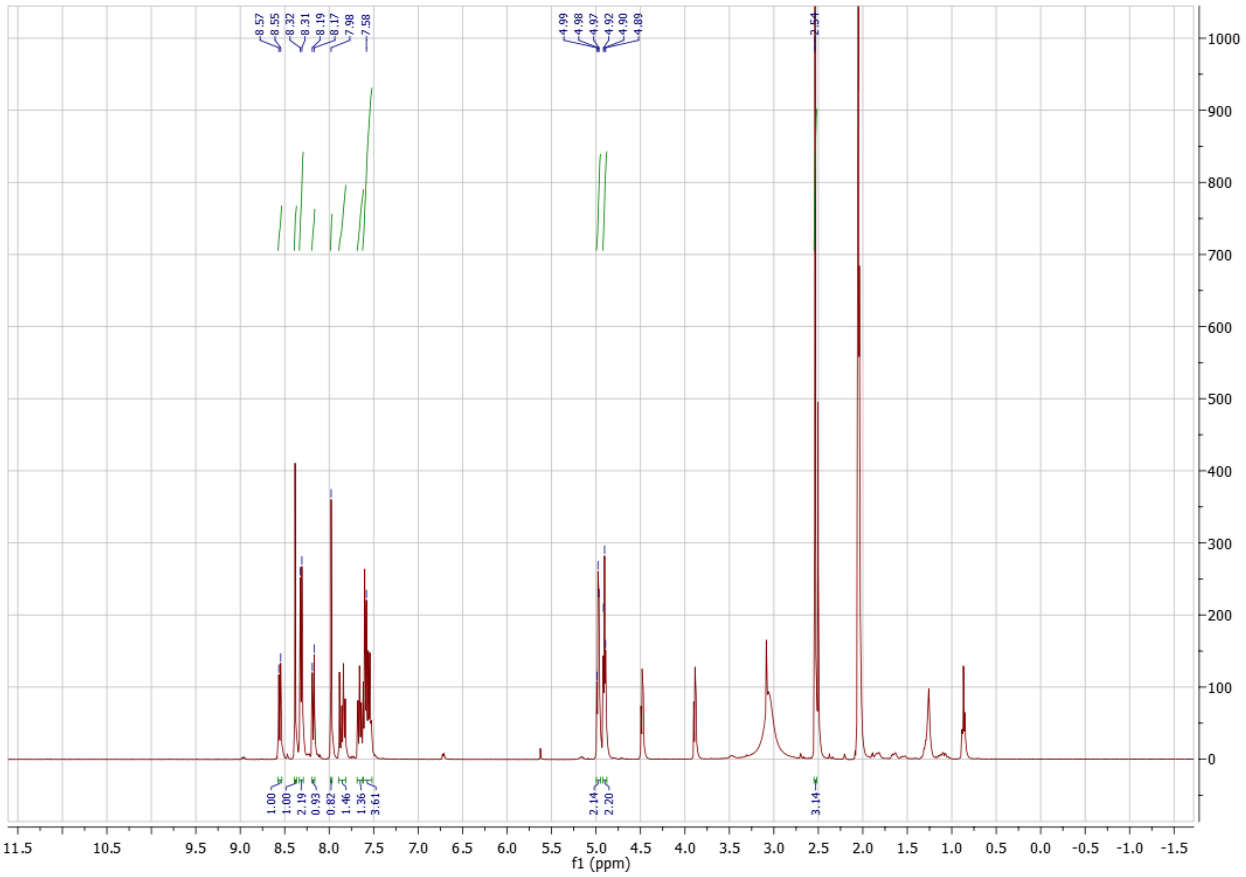

Figure 54- ^{1}H-NMR (400 MHz, 298K, acetone) spectrum of mdz-pqc

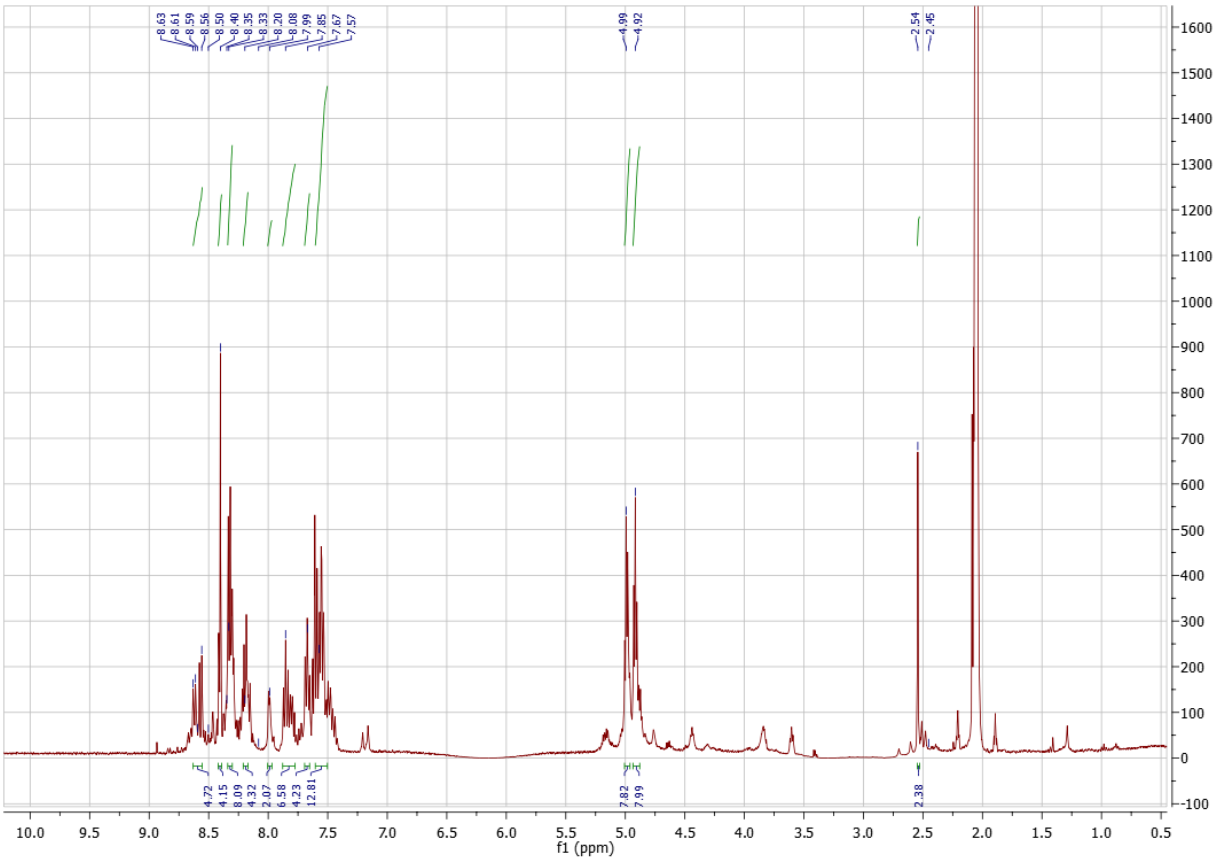

Figure 55 - ^{1}H-NMR spectrum (400 MHz, 298K, acetone) of $[Ir(mdz\text{-}pqc)_2(\mu Cl)]_2$

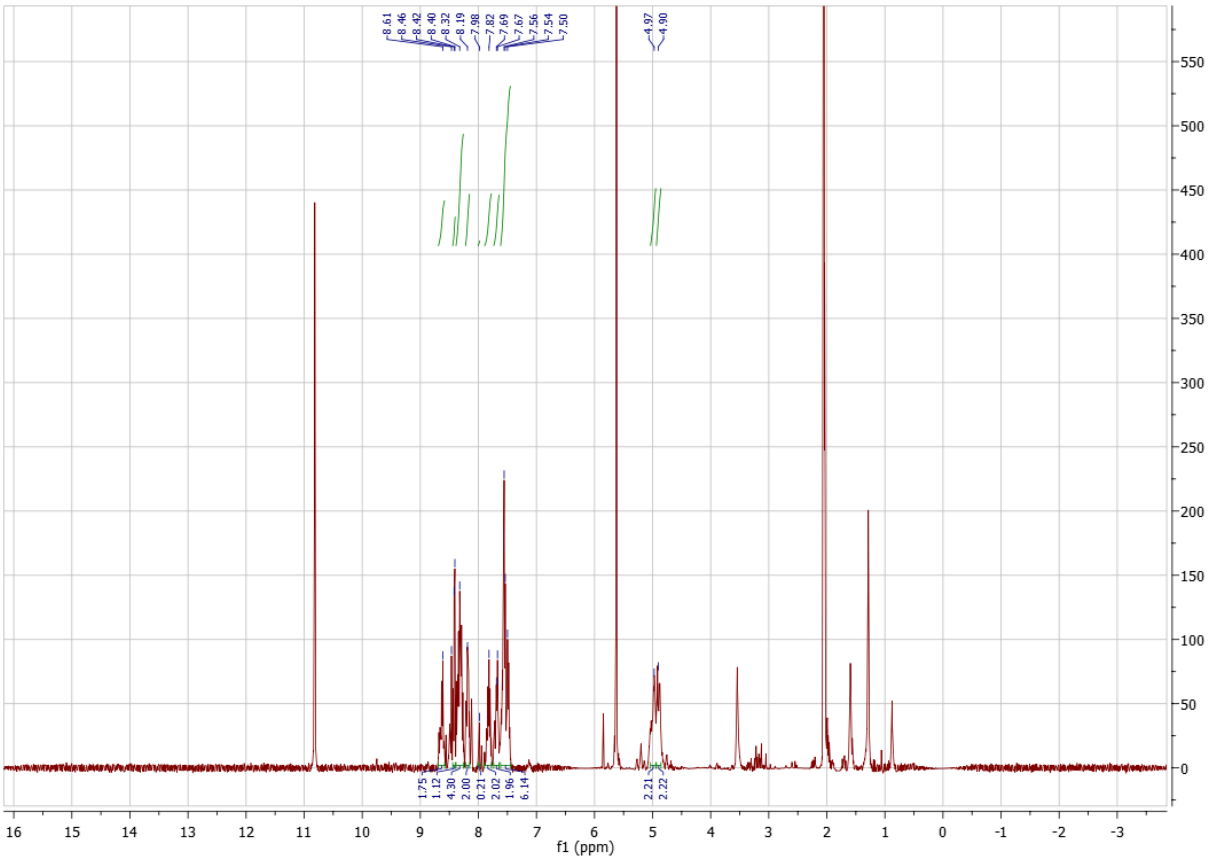

Figure 56- ^{1}H-NMR spectrum (400 MHz, 298K, acetone) of [Ir(mdz-pqc)$_2$(bbzH$_2$)]Cl

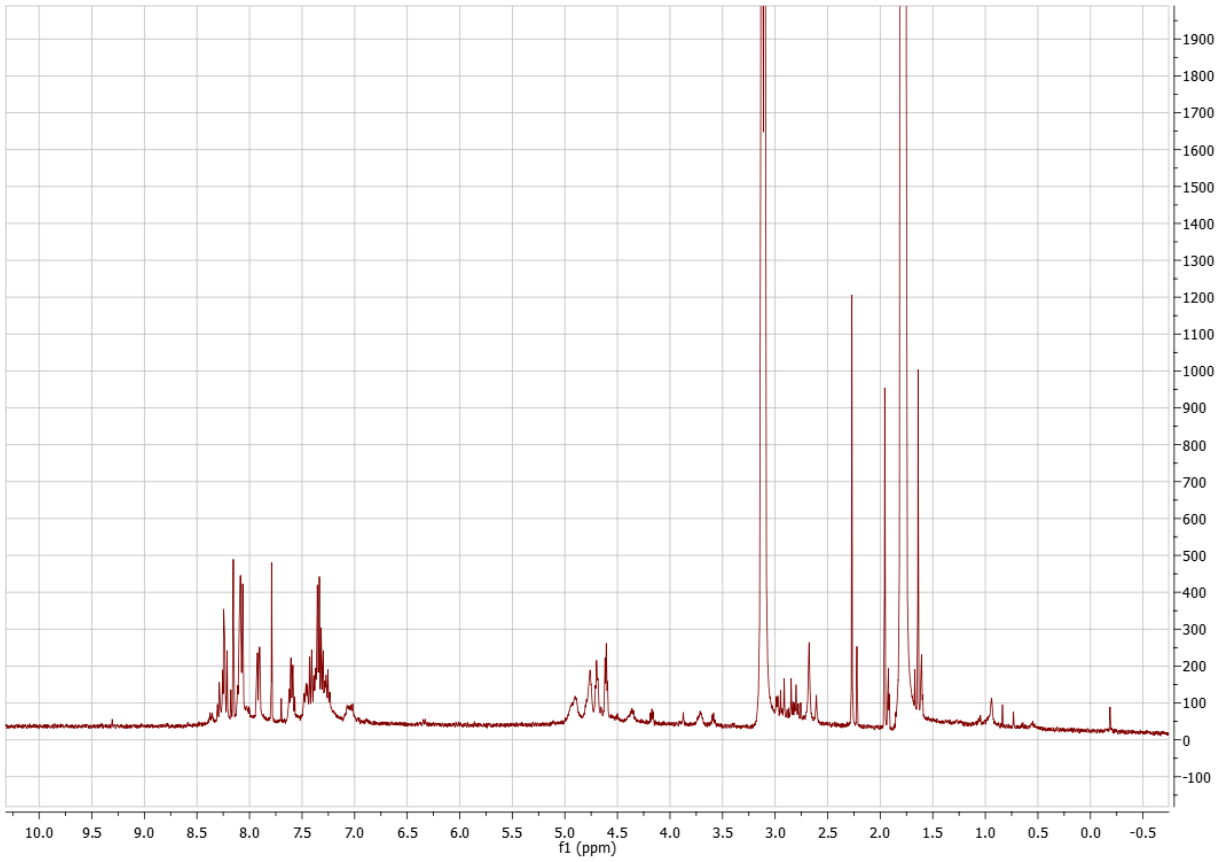

Figure 57- ^{1}H-NMR (400 Hz, 223 K, acetone) spectrum of [Ir(mdz-pqc)$_2$(bbzH$_2$)]Cl, Complex 14

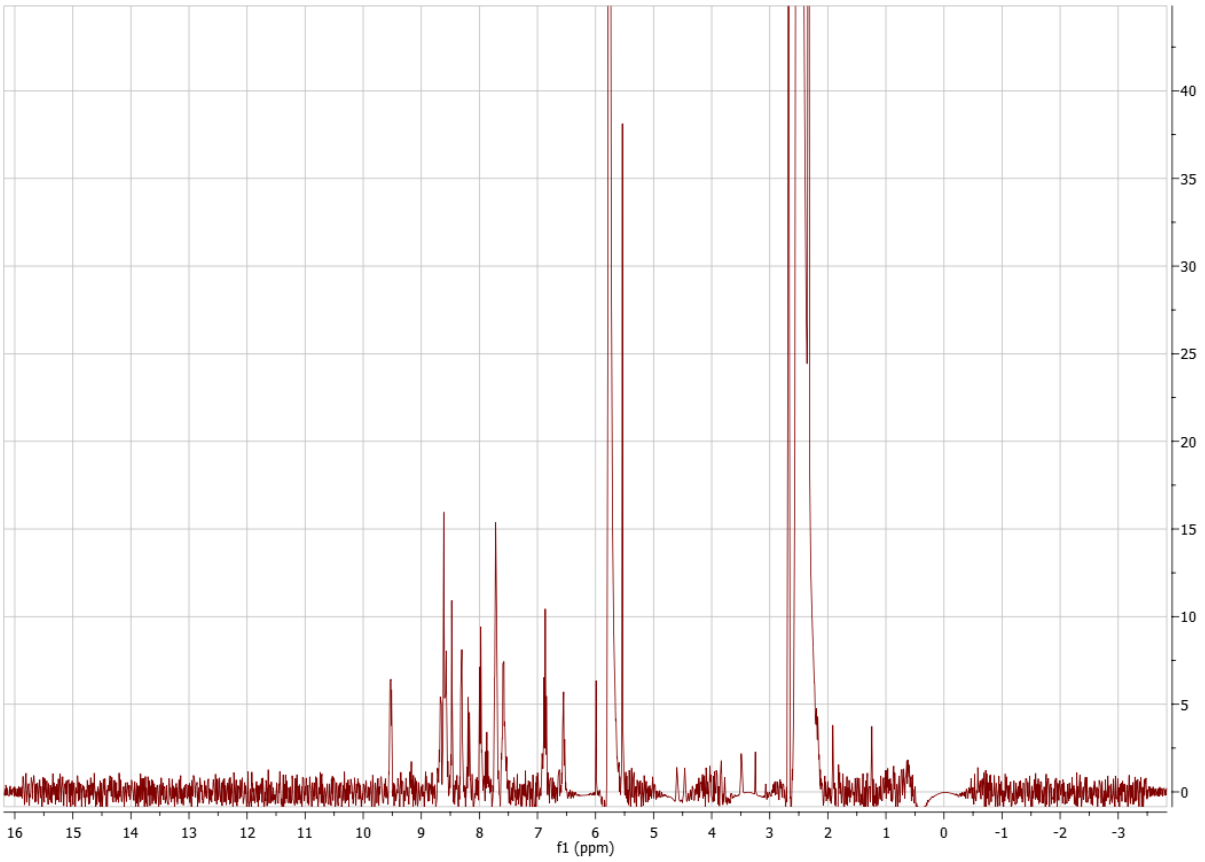

Figure 58- ^{1}H-NMR spectrum (400 MHz, 298K, acetone) of $[Ir(pqc)_2(\mu Cl)]_2$

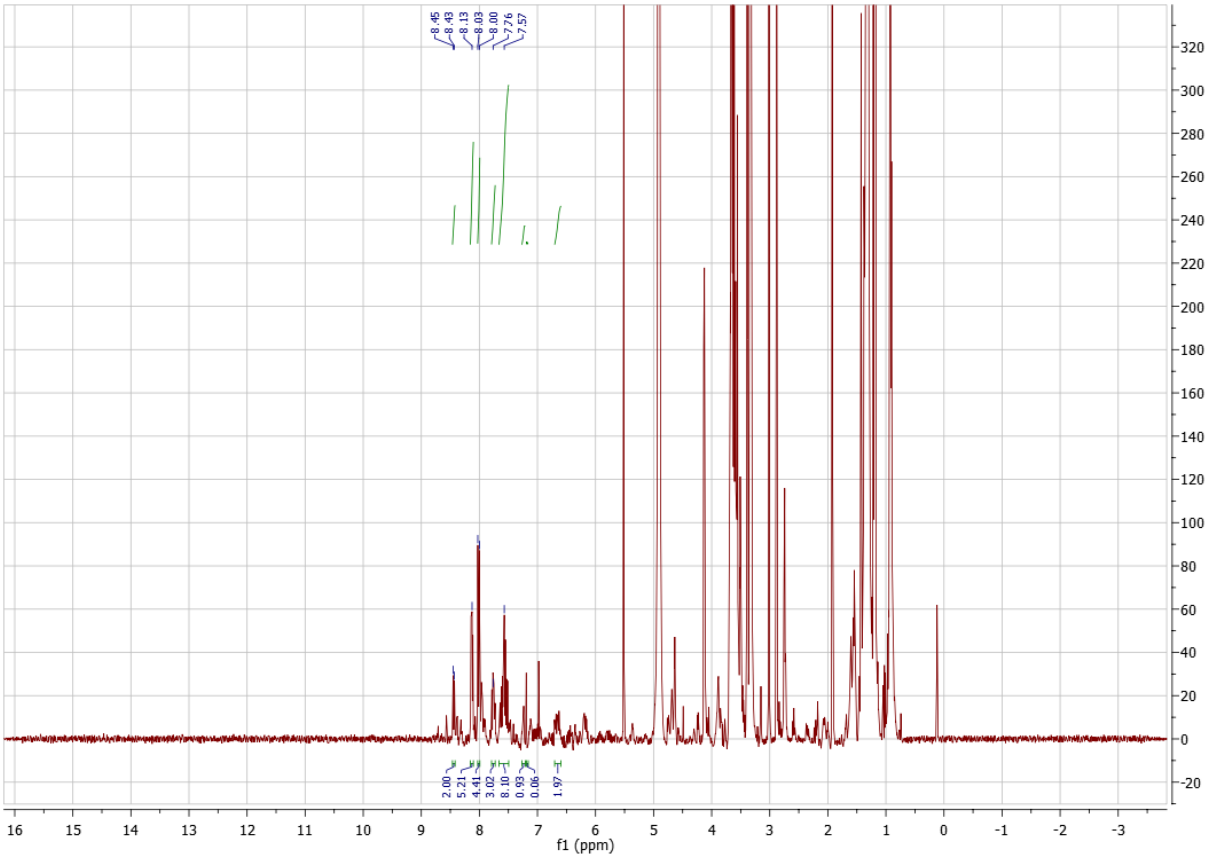

Figure 59- ^{1}H-NMR spectrum (400 MHz, 298K, acetone) of [Ir(pqc)$_2$(bbzH$_2$)]Cl, Complex 15

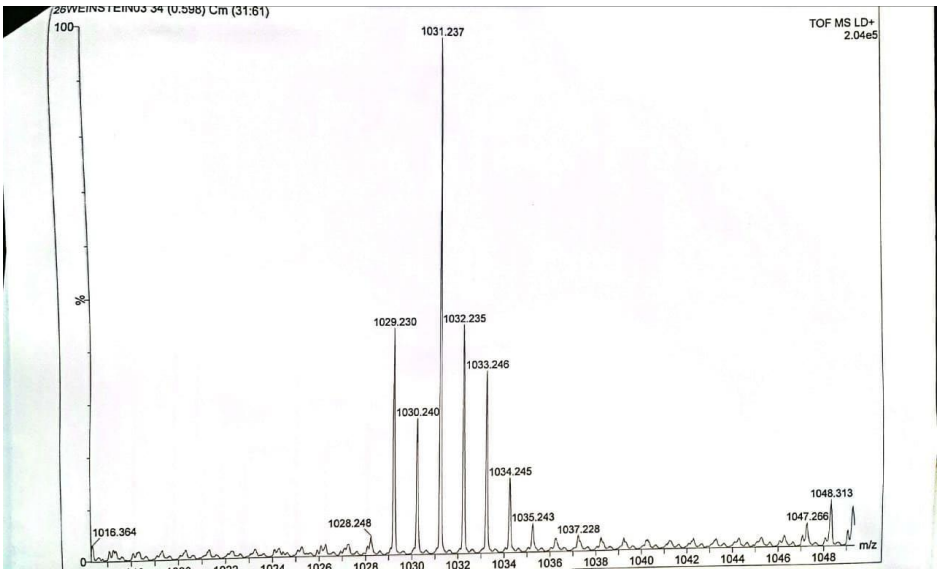

Figure 60- TOF MS of [Ir(mdz-pqc)$_2$(bbzH$_2$)]Cl

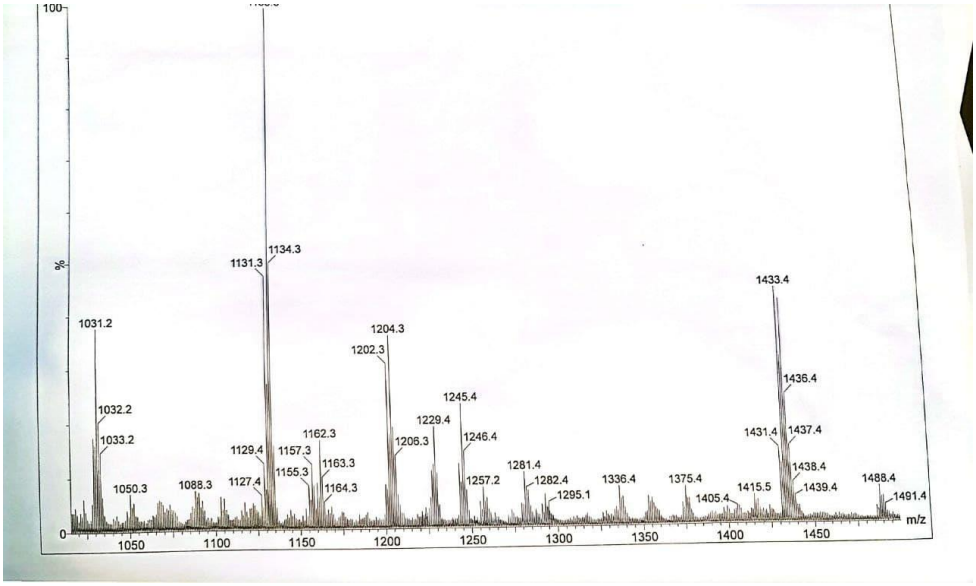

Figure 61- ESI MS of [Ir(mdz-pqc)$_2$(bbzH$_2$)]Cl, Complex 14

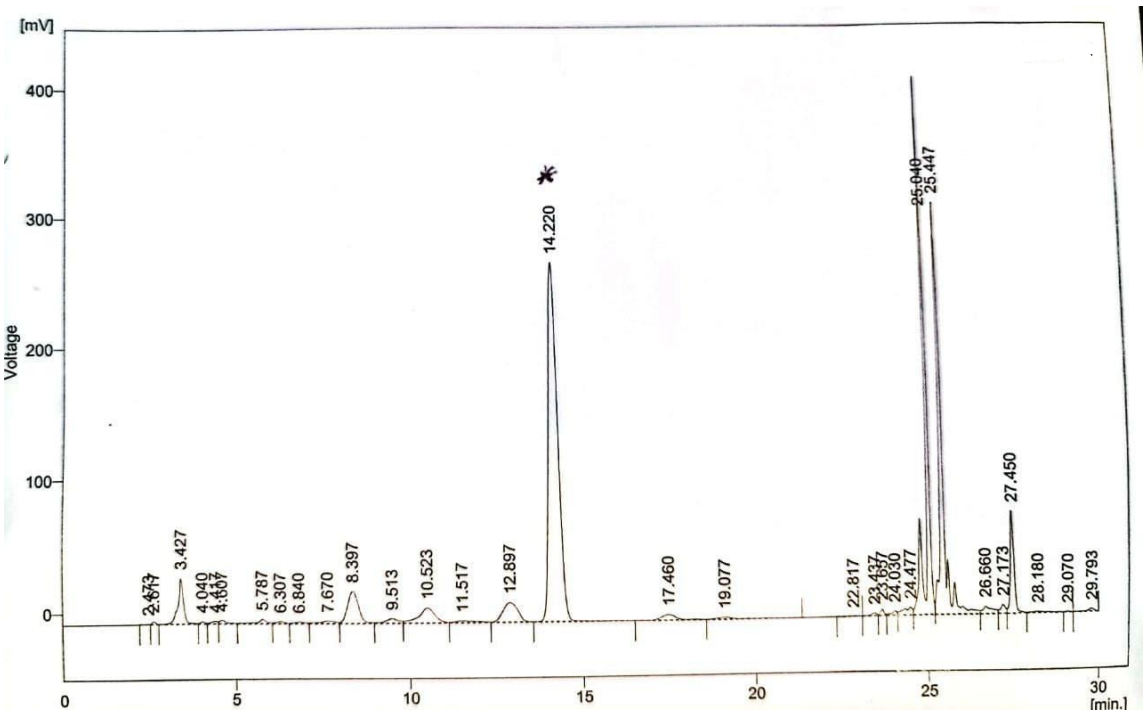

Figure 62- HPLC chromatogram of impure [Ir(mdz-pqc)$_2$(bbzH$_2$)]Cl, Complex 14

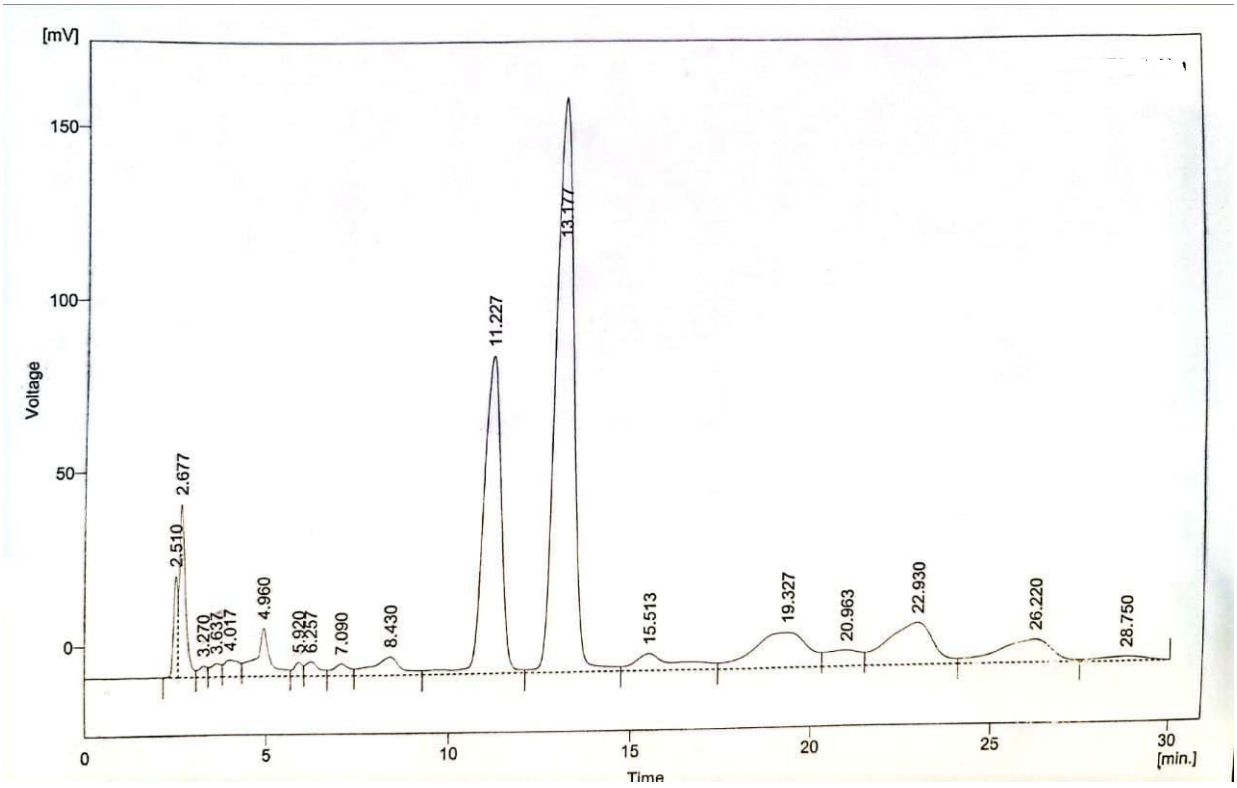

Figure 63- HPLC of [Ir(mdz-pqc)$_2$(bbzH$_2$)]Cl, Complex 14 after purification

References

1 F. Cieplik, D. Deng, W. Crielaard, W. Buchalla, E. Hellwig, A. Al-Ahmad and T. Maisch, Antimicrobial photodynamic therapy – what we know and what we don't, *Critical Reviews in Microbiology*, 2018, **44**, 571–589.

2 R. I. Aminov, A brief history of the antibiotic era: lessons learned and challenges for the future, *Front. Microbiol.*, 2010, **1**, 134.

3 M. J. Renwick, V. Simpkin, E. Mossialos, World Health Organization, Regional Office for Europe, and European Observatory on Health Systems and Policies, *Targeting innovation in antibiotic drug discovery and development: the need for a one health - one Europe - one world framework*, 2016.

4 C. J. Murray, K. S. Ikuta, F. Sharara, L. Swetschinski, G. R. Aguilar, A. Gray, C. Han, C. Bisignano, P. Rao, E. Wool, S. C. Johnson, A. J. Browne, M. G. Chipeta, F. Fell, S. Hackett, G. Haines-Woodhouse, B. H. K. Hamadani, E. A. P. Kumaran, B. McManigal, R. Agarwal, S. Akech, S. Albertson, J. Amuasi, J. Andrews, A. Aravkin, E. Ashley, F. Bailey, S. Baker, B. Basnyat, A. Bekker, R. Bender, A. Bethou, J. Bielicki, S. Boonkasidecha, J. Bukosia, C. Carvalheiro, C. Castañeda-Orjuela, V. Chansamouth, S. Chaurasia, S. Chiurchiù, F. Chowdhury, A. J. Cook, B. Cooper, T. R. Cressey, E. Criollo-Mora, M. Cunningham, S. Darboe, N. P. J. Day, M. D. Luca, K. Dokova, A. Dramowski, S. J. Dunachie, T. Eckmanns, D. Eibach, A. Emami, N. Feasey, N. Fisher-Pearson, K. Forrest, D. Garrett, P. Gastmeier, A. Z. Giref, R. C. Greer, V. Gupta, S. Haller, A. Haselbeck, S. I. Hay, M. Holm, S. Hopkins, K. C. Iregbu, J. Jacobs, D. Jarovsky, F. Javanmardi, M. Khorana, N. Kissoon, E. Kobeissi, T. Kostyanev, F. Krapp, R. Krumkamp, A. Kumar, H. H. Kyu, C. Lim, D. Limmathurotsakul, M. J. Loftus, M. Lunn, J. Ma, N. Mturi, T. Munera-Huertas, P. Musicha, M. M. Mussi-Pinhata, T. Nakamura, R. Nanavati, S. Nangia, P. Newton, C. Ngoun, A. Novotney, D. Nwakanma, C. W. Obiero, A. Olivas-Martinez, P. Olliaro, E. Ooko, E. Ortiz-Brizuela, A. Y. Peleg, C. Perrone, N. Plakkal, A. Ponce-de-Leon, M. Raad, T. Ramdin, A. Riddell, T. Roberts, J. V. Robotham,

A. Roca, K. E. Rudd, N. Russell, J. Schnall, J. A. G. Scott, M. Shivamallappa, J. Sifuentes-Osornio, N. Steenkeste, A. J. Stewardson, T. Stoeva, N. Tasak, A. Thaiprakong, G. Thwaites, C. Turner, P. Turner, H. R. van Doorn, S. Velaphi, A. Vongpradith, H. Vu, T. Walsh, S. Waner, T. Wangrangsimakul, T. Wozniak, P. Zheng, B. Sartorius, A. D. Lopez, A. Stergachis, C. Moore, C. Dolecek and M. Naghavi, Global burden of bacterial antimicrobial resistance in 2019: a systematic analysis, *The Lancet*, 2022, **399**, 629–655.

5 C. Schweitzer and R. Schmidt, Physical Mechanisms of Generation and Deactivation of Singlet Oxygen, *Chemical Reviews*, 2003, **103**, 1685–1758.

6 E. L. Clennan and A. Pace, Advances in singlet oxygen chemistry, *Tetrahedron*, 2005, **61**, 6665–6691.

7 J.-M. Aubry, C. Pierlot, J. Rigaudy and R. Schmidt, Reversible Binding of Oxygen to Aromatic Compounds, *Accounts of Chemical Research*, 2003, **36**, 668–675.

8 N. J. Turro and M. F. Chow, Mechanism of thermolysis of endoperoxides of aromatic compounds. Activation parameters, magnetic field, and magnetic isotope effects, *Journal of the American Chemical Society*, 1981, **103**, 7218–7224.

9 N. J. Turro, Fun with Photons, Reactive Intermediates, and Friends. Skating on the Edge of the Paradigms of Physical Organic Chemistry, Organic Supramolecular Photochemistry, and Spin Chemistry, *The Journal of Organic Chemistry*, 2011, **76**, 9863–9890.

10 C. S. Foote, Mechanisms of Photosensitized Oxidation, *Science*, 1968, **162**, 963–970.

11 M. DeRosa, Photosensitized singlet oxygen and its applications, *Coordination Chemistry Reviews*, 2002, **233–234**, 351–371.

12 P. R. Ogilby, Singlet oxygen: there is indeed something new under the sun, *Chemical Society Reviews*, 2010, **39**, 3181.

13 R. W. Redmond and I. E. Kochevar, Spatially Resolved Cellular Responses to Singlet Oxygen, *Photochemistry and Photobiology*, 2006, **82**, 1178.

14 I. Fridovich, Oxygen toxicity: A radical explanation, *J. Exp. Biol.*, 1998, **201**, 1203–1209.

15 B. Chen, T. Roskams and P. a. M. de Witte, Antivascular tumor eradication by hypericin-mediated photodynamic therapy, *Photochem. Photobiol.*, 2002, **76**, 509–513.

16 R. Weissleder, A clearer vision for in vivo imaging, *Nature Biotechnology*, 2001, **19**, 316–317.

17 R. Lipson, E. Baldes and A. Olsen, Use of a Derivative of Hematoporphyrin in Tumor Detection, *J. Natl. Cancer Inst.*, 1961, **26**, 1-.

18 T. Dougherty, Activated Dyes as Antitumor Agents, *JNCI-J. Natl. Cancer Inst.*, 1974, **52**, 1333–1336.

19 D. Kessel, Sites of Photosensitization by Derivatives of Hematoporphyrin, *Photochem. Photobiol.*, 1986, **44**, 489–493.

20 P. Agostinis, K. Berg, K. A. Cengel, T. H. Foster, A. W. Girotti, S. O. Gollnick, S. M. Hahn, M. R. Hamblin, A. Juzeniene, D. Kessel, M. Korbelik, J. Moan, P. Mroz, D. Nowis, J. Piette, B. C. Wilson and J. Golab, Photodynamic Therapy of Cancer: An Update, *CA-Cancer J. Clin.*, 2011, **61**, 250–281.

21 D. Vecchio, T. Dai, L. Huang, L. Fantetti, G. Roncucci and M. R. Hamblin, Antimicrobial photodynamic therapy with RLP068 kills methicillin-resistant Staphylococcus aureus and improves wound healing in a mouse model of infected skin abrasion, *J. Biophotonics*, 2013, **6**, 733–742.

22 E. Mannucci, S. Genovese, M. Monami, G. Navalesi, F. Dotta, R. Anichini, F. Romagnoli and G. Gensini, Photodynamic topical antimicrobial therapy for infected foot ulcers in patients with diabetes: a randomized, double-blind, placebo-controlled study-the DANTE (Diabetic ulcer Antimicrobial New Topical treatment Evaluation) study, *Acta Diabetol.*, 2014, **51**, 435–440.

23 X.-F. Zhang, X. Li, L. Niu, L. Sun and L. Liu, Charge Transfer Photophysics of Tetra(α-amino) Zinc Phthalocyanine, *J Fluoresc*, 2009, **19**, 947–954.

24 A. Wagner, U. W. Denzer, D. Neureiter, T. Kiesslich, A. Puespoeck, E. A. J. Rauws, K. Emmanuel, N. Degenhardt, U. Frick, U. Beuers, A. W. Lohse, F. Berr and G. W. Wolkersdoerfer,

Temoporfin improves efficacy of photodynamic therapy in advanced biliary tract carcinoma: A multicenter prospective phase II study, *Hepatology*, 2015, **62**, 1456–1465.

25 E. Palao, R. Sola-Llano, A. Tabero, H. Manzano, A. R. Agarrabeitia, A. Villanueva, I. Lopez-Arbeloa, V. Martinez-Martinez and M. J. Ortiz, Acetylacetonate BODIPY-Biscyclometalated Iridium(III) Complexes: Effective Strategy towards Smarter Fluorescent Photosensitizer Agents, *Chem.-Eur. J.*, 2017, **23**, 10139–10147.

26 V. S. Müller Campanile, C. Giannopoulou, G. Campanile, J. A. Cancela and A. Mombelli, Single or repeated antimicrobial photodynamic therapy as adjunct to ultrasonic debridement in residual periodontal pockets: clinical, microbiological, and local biological effects, *Lasers Med Sci*, 2015, **30**, 27–34.

27 M. Segarra-Vidal, S. Guerra-Ojeda, L. S. Vallés, A. López-Roldán, M. D. Mauricio, M. Aldasoro, F. Alpiste-Illueca and J. M. Vila, Effects of photodynamic therapy in periodontal treatment: A randomized, controlled clinical trial, *J Clin Periodontol*, 2017, **44**, 915–925.

28 A. Skurska, E. Dolinska, M. Pietruska, J. K. Pietruski, V. Dymicka, H. Kemona, N. B. Arweiler, R. Milewski and A. Sculean, Effect of nonsurgical periodontal treatment in conjunction with either systemic administration of amoxicillin and metronidazole or additional photodynamic therapy on the concentration of matrix metalloproteinases 8 and 9 in gingival crevicular fluid in patients with aggressive periodontitis, *BMC Oral Health*, 2015, **15**, 63.

29 H. A. Alwaeli, S. N. Al-Khateeb and A. Al-Sadi, Long-term clinical effect of adjunctive antimicrobial photodynamic therapy in periodontal treatment: a randomized clinical trial, *Lasers Med Sci*, 2015, **30**, 801–807.

30 G. Hill, C. Dehn, A. V. Hinze, M. Frentzen and J. Meister, Indocyanine green-based adjunctive antimicrobial photodynamic therapy for treating chronic periodontitis: A randomized clinical trial, *Photodiagnosis and Photodynamic Therapy*, 2019, **26**, 29–35.

31 O. Raab, Effect of fluorescent substances on Infusoria, *Z. Biol.*, 1900, **39**, 524–546.

32 Z. Malik, H. Ladan and Y. Nitzan, Photodynamic Inactivation of Gram-Negative Bacteria - Problems and Possible Solutions, *J. Photochem. Photobiol. B-Biol.*, 1992, **14**, 262–266.

33 D. M. Adolfo Vera, M. H. Haynes, A. R. Ball, T. Dai, C. Astrakas, M. J. Kelso, M. R. Hamblin and G. P. Tegos, Strategies to Potentiate Antimicrobial Photoinactivation by Overcoming Resistant Phenotypes, *Photochem. Photobiol.*, 2012, **88**, 499–511.

34 T. Maisch, Resistance in antimicrobial photodynamic inactivation of bacteria, *Photochem. Photobiol. Sci.*, 2015, **14**, 1518–1526.

35 V. Zijnge, M. B. M. van Leeuwen, J. E. Degener, F. Abbas, T. Thurnheer, R. Gmuer and H. J. M. Harmsen, Oral Biofilm Architecture on Natural Teeth, *PLoS One*, 2010, **5**, e9321.

36 X. Y. Liu, A. Sroka, J. Potempa and C. A. Genco, Coordinate expression of the Porphyromonas gingivalis lysine-specific gingipain proteinase, Kgp, arginine-specific gingipain proteinase, RgpA, and the heme/hemoglobin receptor, HmuR, *Biol. Chem.*, 2004, **385**, 1049–1057.

37 O. Yimaz, The chronicles of Porphyromonas gingivalis: the microblum, the human oral epithelium and their interplay, *Microbiology-(UK)*, 2008, **154**, 2897–2903.

38 O. Yilmaz, K. Watanabe and R. J. Lamont, Involvement of integrins in fimbriae-mediated binding and invasion by Porphyromonas gingivalis, *Cell Microbiol.*, 2002, **4**, 305–314.

39 O. Yilmaz, L. Yao, K. Maeda, T. M. Rose, E. L. Lewis, M. Duman, R. J. Lamont and D. M. Ojcius, ATP scavenging by the intracellular pathogen Porphyromonas gingivalis inhibits P2X(7)-mediated host-cell apoptosis, *Cell Microbiol.*, 2008, **10**, 863–875.

40 O. Yilmaz, P. Verbeke, R. J. Lamont and D. A. Ojcius, Intercellular spreading of Porphyromonas gingivalis infection in primary gingival epithelial cells, *Infect. Immun.*, 2006, **74**, 703–710.

41 J. Potempa, R. Pike and J. Travis, Titration and mapping of the active site of cysteine proteinases from Porphyromonas gingivalis (Gingipains) using peptidyl chloromethanes, *Biol. Chem.*, 1997, **378**, 223–230.

42 Y. Guo, K.-A. Nguyen and J. Potempa, Dichotomy of gingipains action as virulence factors: from cleaving substrates with the precision of a surgeon's knife to a meat chopper-like brutal degradation of proteins, *Periodontol. 2000*, 2010, **54**, 15–44.

43 M. A. Curtis, J. Aduse-Opoku and M. Rangarajan, Cysteine proteases of Porphyromonas gingivalis, *Crit. Rev. Oral Biol. Med.*, 2001, **12**, 192–216.

44 C. Y. Chiang, G. Kyritsis, D. T. Graves and S. Amar, Interleukin-1 and tumor necrosis factor activities partially account for calvarial bone resorption induced by local injection of lipopolysaccharide, *Infect. Immun.*, 1999, **67**, 4231–4236.

45 N. A. Paramonov, J. Aduse-Opoku, A. Hashim, M. Rangarajan and M. A. Curtis, Structural Analysis of the Core Region of O-Lipopolysaccharide of Porphyromonas gingivalis from Mutants Defective in O-Antigen Ligase and O-Antigen Polymerase, *J. Bacteriol.*, 2009, **191**, 5272–5282.

46 G. Hajishengallis, M. Wang and S. Liang, Induction of Distinct TLR2-Mediated Proinflammatory and Proadhesive Signaling Pathways in Response to Porphyromonas gingivalis Fimbriae, *J. Immunol.*, 2009, **182**, 6690–6696.

47 N. Paramonov, M. Rangarajan, A. Hashim, A. Gallagher, J. Aduse-Opoku, J. M. Slaney, E. Hounsell and M. A. Curtis, Structural analysis of a novel anionic polysaccharide from Porphyromonas gingivalis strain W50 related to Arg-gingipain glycans, *Mol. Microbiol.*, 2005, **58**, 847–863.

48 M. L. Laine and A. J. van Winkelhoff, Virulence of six capsular serotypes of Porphyromonas gingivalis in a mouse model, *Oral Microbiol. Immunol.*, 1998, **13**, 322–325.

49 T. J. Sims, R. E. Schifferle, R. W. Ali, N. Skaug and R. C. Page, Immunoglobulin G response of periodontitis patients to Porphyromonas gingivalis capsular carbohydrate and lipopolysaccharide antigens, *Oral Microbiol. Immunol.*, 2001, **16**, 193–201.

50 G. Sundqvist, D. Figdor, L. Hanstrom, S. Sorlin and G. Sandstrom, Phagocytosis and Virulence of Different Strains of Porphyromonas-Gingivalis, *Scandinavian Journal of Dental Research*, 1991, **99**, 117–129.

51 J. Brunner, N. Scheres, N. B. El Idrissi, D. M. Deng, M. L. Laine, A. J. van Winkelhoff and W. Crielaard, The capsule of Porphyromonas gingivalis reduces the immune response of human gingival fibroblasts, *BMC Microbiol.*, 2010, **10**, 5.

52 R. J. Lamont and H. F. Jenkinson, Life below the gum line: Pathogenic mechanisms of Porphyromonas gingivalis, *Microbiol. Mol. Biol. Rev.*, 1998, **62**, 1244-+.

53 H. Inaba, K. Nakano, T. Kato, R. Nomura, S. Kawai, M. Kuboniwa, K. Ishihara, T. Ooshima and A. Amano, Heterogenic virulence and related factors among clinical isolates of Porphyromonas gingivalis with type II fimbriae, *Oral Microbiol. Immunol.*, 2008, **23**, 29–35.

54 M. Listgarten, C. Lai and V. Young, Microbial Composition and Pattern of Antibiotic-Resistance in Subgingival Microbial Samples from Patients with Refractory Periodontitis, *J. Periodont.*, 1993, **64**, 155–161.

55 M. Feres, A. D. Haffajee, K. Allard, S. Som, J. M. Goodson and S. S. Socransky, Antibiotic resistance of subgingival species during and after antibiotic therapy, *J. Clin. Periodontol.*, 2002, **29**, 724–735.

56 M. Merchat, G. Bertolini, P. Giacomini, A. Villanueva and G. Jori, Meso-substituted cationic porphyrins as efficient photosensitizers of gram-positive and gram-negative bacteria, *J. Photochem. Photobiol. B-Biol.*, 1996, **32**, 153–157.

57 M. Wilson, T. Burns, J. Pratten and G. Pearson, Bacteria in Supragingival Plaque Samples Can Be Killed by Low-Power Laser-Light in the Presence of a Photosensitizer, *J. Appl. Bacteriol.*, 1995, **78**, 569–574.

58 N. S. Soukos, S. E. Mulholland, S. S. Socransky and A. G. Doukas, Photodestruction of human dental plaque bacteria: Enhancement of the photodynamic effect by photomechanical waves in an oral biofilm model, *Lasers Surg. Med.*, 2003, **33**, 161–168.

59 P. S. Stewart, L. Grab and J. A. Diemer, Analysis of biocide transport limitation in an artificial biofilm system, *J. Appl. Microbiol.*, 1998, **85**, 495–500.

60 I. Foley and P. Gilbert, Antibiotic resistance of biofilms, *Biofouling*, 1996, **10**, 331–346.

61 E. Baggaley, J. A. Weinstein and J. A. G. Williams, Lighting the way to see inside the live cell with luminescent transition metal complexes, *Coord. Chem. Rev.*, 2012, **256**, 1762–1785.

62 J. Zhao, W. Wu, J. Sun and S. Guo, Triplet photosensitizers: from molecular design to applications, *Chem. Soc. Rev.*, 2013, **42**, 5323–5351.

63 J. A. G. Williams, in *Photochemistry and Photophysics of Coordination Compounds Ii*, eds. V. Balzani and S. Campagna, Springer-Verlag Berlin, Berlin, 2007, vol. 281, pp. 205–268.

64 D. A. K. Vezzu, D. Ravindranathan, A. W. Gamer, L. Bartolotti, M. E. Smith, P. D. Boyle and S. Huo, Highly Luminescent Tridentate (NC)-C-boolean AND*N Platinum(II) Complexes Featured in Fused Five-Six-Membered Metallacycle and Diminishing Concentration Quenching, *Inorg. Chem.*, 2011, **50**, 8261–8273.

65 M. L. Muro, S. Diring, X. Wang, R. Ziessel and F. N. Castellano, Photophysics in Platinum(II) Bipyridylacetylides, *Inorg. Chem.*, 2009, **48**, 11533–11542.

66 Y. Sun, Z. M. Hudson, Y. Rao and S. Wang, Tuning and Switching MLCT Phosphorescence of [Ru(bpy)(3)](2+) Complexes with Triarylboranes and Anions, *Inorg. Chem.*, 2011, **50**, 3373–3378.

67 Y. You and W. Nam, Photofunctional triplet excited states of cyclometalated Ir(III) complexes: beyond electroluminescence, *Chem. Soc. Rev.*, 2012, **41**, 7061–7084.

68 E. Holder, B. M. W. Langeveld and U. S. Schubert, New trends in the use of transition metal-ligand complexes for applications in electroluminescent devices, *Adv. Mater.*, 2005, **17**, 1109–1121.

69 P. J. Hay, Theoretical studies of the ground and excited electronic states in cyclometalated phenylpyridine Ir(III) complexes using density functional theory, *J. Phys. Chem. A*, 2002, **106**, 1634–1641.

70 D. N. Chirdon, C. E. McCusker, F. N. Castellano and S. Bernhard, Tracking of Tuning Effects in Bis-Cyclometalated Iridium Complexes: A Combined Time Resolved Infrared Spectroscopy, Electrochemical, and Computational Study, *Inorg. Chem.*, 2013, **52**, 8795–8804.

71 Y. M. You and S. Y. Park, Inter-ligand energy transfer and related emission change in the cyclometalated heteroleptic iridium complex: Facile and efficient color tuning over the whole visible range by the ancillary ligand structure, *J. Am. Chem. Soc.*, 2005, **127**, 12438–12439.

72 A. F. Rausch, M. E. Thompson and H. Yersin, Blue Light Emitting Ir(III) Compounds for OLEDs - New Insights into Ancillary Ligand Effects on the Emitting Triplet State, *J. Phys. Chem. A*, 2009, **113**, 5927–5932.

73 J. Li, P. I. Djurovich, B. D. Alleyne, M. Yousufuddin, N. N. Ho, J. C. Thomas, J. C. Peters, R. Bau and M. E. Thompson, Synthetic control of excited-state properties in cyclometalated Ir(III) complexes using ancillary ligands, *Inorg. Chem.*, 2005, **44**, 1713–1727.

74 S. Lamansky, P. Djurovich, D. Murphy, F. Abdel-Razzaq, H. E. Lee, C. Adachi, P. E. Burrows, S. R. Forrest and M. E. Thompson, Highly phosphorescent bis-cyclometalated iridium complexes: Synthesis, photophysical characterization, and use in organic light emitting diodes, *J. Am. Chem. Soc.*, 2001, **123**, 4304–4312.

75 S. Liu, P. Mueller, M. K. Takase and T. M. Swager, 'Click' Synthesis of Heteroleptic Tris-Cyclometalated Iridium(III) Complexes: Cu(I) Triazolide Intermediates as Transmetalating Reagents, *Inorg. Chem.*, 2011, **50**, 7598–7609.

76 R. M. Gao, D. G. Ho, B. Hernandez, M. Selke, D. Murphy, P. I. Djurovich and M. E. Thompson, Bis-cyclometalated Ir(III) complexes as efficient singlet oxygen sensitizers, *J. Am. Chem. Soc.*, 2002, **124**, 14828–14829.

77 P. I. Djurovich, D. Murphy, M. E. Thompson, B. Hernandez, R. Gao, P. L. Hunt and M. Selke, Cyclometalated iridium and platinum complexes as singlet oxygen photosensitizers: quantum yields, quenching rates and correlation with electronic structures, *Dalton Trans.*, 2007, 3763–3770.

78 J. Wang, Y. Lu, N. McGoldrick, C. Zhang, W. Yang, J. Zhao and S. M. Draper, Dual phosphorescent dinuclear transition metal complexes, and their application as triplet photosensitizers for TTA upconversion and photodynamic therapy, *J. Mater. Chem. C*, 2016, **4**, 6131–6139.

79 P. Majumdar, X. Yuan, S. Li, B. Le Guennic, J. Ma, C. Zhang, D. Jacquemin and J. Zhao, Cyclometalated Ir(III) complexes with styryl-BODIPY ligands showing near, *J. Mat. Chem. B*, 2014, **2**, 2838–2854.

80 L. Wang, H. Yin, P. Cui, M. Hetu, C. Wang, S. Monro, R. D. Schaller, C. G. Cameron, B. Liu, S. Kilina, S. A. McFarland and W. Sun, Near-infrared-emitting heteroleptic cationic iridium complexes derived from 2,3-diphenylbenzo[g]quinoxaline as in vitro theranostic photodynamic therapy agents, *Dalton Trans.*, 2017, **46**, 8091–8103.

81 L. K. McKenzie, I. V. Sazanovich, E. Baggaley, M. Bonneau, V. Guerchais, J. A. G. Williams, J. A. Weinstein and H. E. Bryant, Metal Complexes for Two-Photon Photodynamic Therapy: A Cyclometallated Iridium Complex Induces Two-Photon Photosensitization of Cancer Cells under Near-IR Light, *Chem.-Eur. J.*, 2017, **23**, 234–238.

82 L. R. Jennings, H. E. Colley, J. Ong, F. Panagakos, J. G. Masters, H. M. Trivedi, C. Murdoch and S. Whawell, Development and Characterization of In Vitro Human Oral Mucosal Equivalents Derived from Immortalized Oral Keratinocytes, *Tissue Eng Part C Methods*, 2016, **22**, 1108–1117.

83 M. J. Rubino, Experiences with HEK293: A Human Cell Line, *PDA J Pharm Sci Technol*, 2010, **64**, 392–395.

84 D. P. Aden, A. Fogel, S. Plotkin, I. Damjanov and B. B. Knowles, Controlled synthesis of HBsAg in a differentiated human liver carcinoma-derived cell line, *Nature*, 1979, **282**, 615–616.

85 R. Dulbecco and G. Freeman, Plaque production by the polyoma virus, *Virology*, 1959, **8**, 396–397.

86 M. J. Duncan, S. Nakao, Z. Skobe and H. Xie, Interactions of Porphyromonas gingivalis with epithelial cells., *Infection and Immunity*, 1993, **61**, 2260–2265.

87 J. R. Shewring, PhD thesis, The University of Sheffield, 2017.

88 J. A. Mindell, Lysosomal acidification mechanisms, *Annu. Rev. Physiol.*, 2012, **74**, 69–86.

89 G. Meral, F. Tasar, S. Kocagöz and C. Sener, Factors affecting the antibacterial effects of Nd:YAG laser in vivo, *Lasers Surg Med*, 2003, **32**, 197–202.

90 D. M. Harris, S. L. Jacques and R. Darveau, The Black Bug Myth: Selective photodestruction of pigmented pathogens: THE BLACK BUG MYTH, *Lasers in Surgery and Medicine*, 2016, **48**, 706–714.

91 J. R. Shewring, A. J. Cankut, L. K. McKenzie, B. J. Crowston, S. W. Botchway, J. A. Weinstein, E. Edwards and M. D. Ward, Multimodal Probes: Superresolution and Transmission Electron Microscopy Imaging of Mitochondria, and Oxygen Mapping of Cells, Using Small-Molecule Ir(III) Luminescent Complexes, *Inorg. Chem.*, 2017, **56**, 15259–15270.

92 M. Mauro, A. Aliprandi, D. Septiadi, N. S. Kehr and L. De Cola, When self-assembly meets biology: luminescent platinum complexes for imaging applications, *Chem. Soc. Rev.*, 2014, **43**, 4144–4166.

93 S. Lofmark, C. Edlund and C. E. Nord, Metronidazole Is Still the Drug of Choice for Treatment of Anaerobic Infections, *Clin. Infect. Dis.*, 2010, **50**, S16–S23.

94 M. Muller, Reductive Activation of Nitroimidazoles in Anaerobic Microorganisms, *Biochem. Pharmacol.*, 1986, **35**, 37–41.

95 C. W. Ang, A. M. Jarrad, M. A. Cooper and M. A. T. Blaskovich, Nitroimidazoles: Molecular Fireworks That Combat a Broad Spectrum of Infectious Diseases, *Journal of Medicinal Chemistry*, 2017, **60**, 7636–7657.

96 R. A. Smith, E. C. Stokes, E. E. Langdon-Jones, J. A. Platts, B. M. Kariuki, A. J. Hallett and S. J. A. Pope, Cyclometalated cinchophen ligands on iridium(iii): towards water-soluble complexes with visible luminescence, *Dalton Transactions*, 2013, **42**, 10347.

97 L.-Y. Zhang, Y.-J. Hou, M. Pan, L. Chen, Y.-X. Zhu, S.-Y. Yin, G. Shao and C.-Y. Su, Near-infrared (NIR) emitting Nd/Yb(III) complexes sensitized by MLCT states of Ru(II)/Ir(III) metalloligands in the visible light region, *Dalton Transactions*, 2015, **44**, 15212–15219.

98 J. Catalan and J. Elguero, in *Advances in Heterocyclic Chemistry*, Elsevier, 1987, vol. 41, pp. 187–274.

99 V. I. Minkin, A. D. Garnovskii, J. Elguero, A. R. Katritzky and O. V. Denisko, in *Advances in Heterocyclic Chemistry*, Elsevier, 2000, vol. 76, pp. 157–323.

100 A. Alshaar, D. Gilmour, D. Lythgoe, I. Mcclenaghan and C. Ramsden, Preparation, Structure and Addition-Reactions of 4-Aminoimidazoles and 5-Aminoimidazoles, *J. Chem. Soc.-Perkin Trans. 1*, 1992, 2779–2788.

101 A. Secrieru, P. M. O'Neill and M. L. S. Cristiano, Revisiting the Structure and Chemistry of 3(5)-Substituted Pyrazoles, *Molecules*, 2019, **25**, 42.

102 M. Kubicki, Two tautomers in one crystal: 4(5)-nitro-5(4)-methoxyimidazole, *Acta Crystallogr B Struct Sci*, 2004, **60**, 191–196.

103 J. Elguero, A. Fruchier and V. Pellegrin, Annular tautomerism in the solid state: a high resolution n.m.r. study, *J. Chem. Soc., Chem. Commun.*, 1981, 1207.

104 R. Boppella and M. Pandiri, Advances in synthesis of nanostructured metal oxides for chemical sensors, *chemical sensors*, 2014, **4**, 19.

105 P. LidstroÈm, J. Tierney, B. Wathey and J. Westman, Microwave assisted organic synthesisÐa review, 2001, 59.

106 L. Khanna, S. Panda and P. Khanna, Synthetic Routes to Symmetric Bisbenzimidazoles: A Review, *Mini-Reviews in Organic Chemistry*, 2012, **9**, 381–396.

107 M. Astasov-Frauenhoffer, O. Braissant, I. Hauser-Gerspach, R. Weiger, C. Walter, N. U. Zitzmann and T. Waltimo, Microcalorimetric Determination of the Effects of Amoxicillin, Metronidazole, and Their Combination on In Vitro Biofilm, *Journal of Periodontology*, 2014, **85**, 349–357.

108 R. G. Masterton, A. Galloway, G. French, M. Street, J. Armstrong, E. Brown, J. Cleverley, P. Dilworth, C. Fry, A. D. Gascoigne, A. Knox, D. Nathwani, R. Spencer and M. Wilcox, Guidelines for the management of hospital-acquired pneumonia in the UK: Report of the Working Party on hospital-acquired pneumonia of the British Society for Antimicrobial Chemotherapy, *J. Antimicrob. Chemother.*, 2008, **62**, 5–34.

109 Health Protection Report, *Northern Ireland*, 2017, **12**, 20.

110 WHO publishes list of bacteria for which new antibiotics are urgently needed, https://www.who.int/news/item/27-02-2017-who-publishes-list-of-bacteria-for-which-new-antibiotics-are-urgently-needed, (accessed 8 February 2022).

111 P. Nordmann and M. Guibert, Extended-spectrum beta-lactamases in Pseudomonas aeruginosa, *J. Antimicrob. Chemother.*, 1998, **42**, 128–131.

112 D. Livermore, Interplay of Impermeability and Chromosomal Beta-Lactamase Activity in Imipenem-Resistant Pseudomonas-Aeruginosa, *Antimicrob. Agents Chemother.*, 1992, **36**, 2046–2048.

113 R. A. Bonomo and D. Szabo, Mechanisms of multidrug resistance in Acinetobacter species and Pseudomonas aeruginosa, *Clin. Infect. Dis.*, 2006, **43**, S49–S56.

114 M. Alhede, K. N. Kragh, K. Qvortrup, M. Allesen-Holm, M. van Gennip, L. D. Christensen, P. Ø. Jensen, A. K. Nielsen, M. Parsek, D. Wozniak, S. Molin, T. Tolker-Nielsen, N. Høiby, M. Givskov and T. Bjarnsholt, Phenotypes of non-attached Pseudomonas aeruginosa aggregates resemble surface attached biofilm, *PLoS One*, 2011, **6**, e27943.

115 O. Ciofu and T. Tolker-Nielsen, Tolerance and Resistance of Pseudomonas aeruginosa Biofilms to Antimicrobial Agents—How P. aeruginosa Can Escape Antibiotics, *Frontiers in Microbiology*.

116 P. M. Bales, E. M. Renke, S. L. May, Y. Shen and D. C. Nelson, Purification and Characterization of Biofilm-Associated EPS Exopolysaccharides from ESKAPE Organisms and Other Pathogens, *PLoS One*, 2013, **8**, e67950.

117 M. S. Dueholm, M. T. Søndergaard, M. Nilsson, G. Christiansen, A. Stensballe, M. T. Overgaard, M. Givskov, T. Tolker-Nielsen, D. E. Otzen and P. H. Nielsen, Expression of Fap amyloids in Pseudomonas aeruginosa, P. fluorescens, and P. putida results in aggregation and increased biofilm formation, *Microbiologyopen*, 2013, **2**, 365–382.

118 C. B. Whitchurch, T. Tolker-Nielsen, P. C. Ragas and J. S. Mattick, Extracellular DNA required for bacterial biofilm formation, *Science*, 2002, **295**, 1487.

119 Y. H. Bae, T. Okano and S. W. Kim, 'On-off' thermocontrol of solute transport. I. Temperature dependence of swelling of N-isopropylacrylamide networks modified with hydrophobic components in water, *Pharm Res*, 1991, **8**, 531–537.

120 M. Allesen-Holm, K. B. Barken, L. Yang, M. Klausen, J. S. Webb, S. Kjelleberg, S. Molin, M. Givskov and T. Tolker-Nielsen, A characterization of DNA release in Pseudomonas aeruginosa cultures and biofilms, *Mol Microbiol*, 2006, **59**, 1114–1128.

121 P. S. Stewart, Theoretical aspects of antibiotic diffusion into microbial biofilms., *Antimicrob Agents Chemother*, 1996, **40**, 2517–2522.

122 M. A. Kohanski, D. J. Dwyer, B. Hayete, C. A. Lawrence and J. J. Collins, A common mechanism of cellular death induced by bactericidal antibiotics, *Cell*, 2007, **130**, 797–810.

123 H. Ma and J. D. Bryers, Non-invasive determination of conjugative transfer of plasmids bearing antibiotic-resistance genes in biofilm-bound bacteria: effects of substrate loading and antibiotic selection, *Appl Microbiol Biotechnol*, 2013, **97**, 317–328.

124 M. Kostakioti, M. Hadjifrangiskou and S. J. Hultgren, Bacterial biofilms: development, dispersal, and therapeutic strategies in the dawn of the postantibiotic era, *Cold Spring Harb Perspect Med*, 2013, **3**, a010306.

125 W. S. da Cruz Nizer, V. Inkovskiy, Z. Versey, N. Strempel, E. Cassol and J. Overhage, Oxidative Stress Response in Pseudomonas aeruginosa, *Pathogens*, 2021, **10**, 1187.

126 A. Romsang, J. Duang-Nkern, P. Leesukon, K. Saninjuk, P. Vattanaviboon and S. Mongkolsuk, The Iron-Sulphur Cluster Biosynthesis Regulator IscR Contributes to Iron Homeostasis and Resistance to Oxidants in Pseudomonas aeruginosa, *PLOS ONE*, 2014, **9**, e86763.

127 L. Cavinato, E. Genise, F. R. Luly, E. G. Di Domenico, P. Del Porto and F. Ascenzioni, Escaping the Phagocytic Oxidative Burst: The Role of SODB in the Survival of Pseudomonas aeruginosa Within Macrophages, *Frontiers in Microbiology*.

128 V. T. Orlandi, F. Bolognese, L. Chiodaroli, T. Tolker-Nielsen and P. 2015 Barbieri, Pigments influence the tolerance of Pseudomonas aeruginosa PAO1 to photodynamically induced oxidative stress, *Microbiology*, **161**, 2298–2309.

129 J. Mestas and C. C. W. Hughes, Of mice and not men: differences between mouse and human immunology, *J Immunol*, 2004, **172**, 2731–2738.

130 J. Shepherd, I. Douglas, S. Rimmer, L. Swanson and S. MacNeil, Development of Three-Dimensional Tissue-Engineered Models of Bacterial Infected Human Skin Wounds, *Tissue Eng. Part C-Methods*, 2009, **15**, 475–484.

131 H. Sueke, S. Kaye, T. Neal, C. Murphy, A. Hall, D. Whittaker, S. Tuft and C. Parry, Minimum Inhibitory Concentrations of Standard and Novel Antimicrobials for Isolates from Bacterial Keratitis, *Invest. Ophthalmol. Vis. Sci.*, 2010, **51**, 2519.